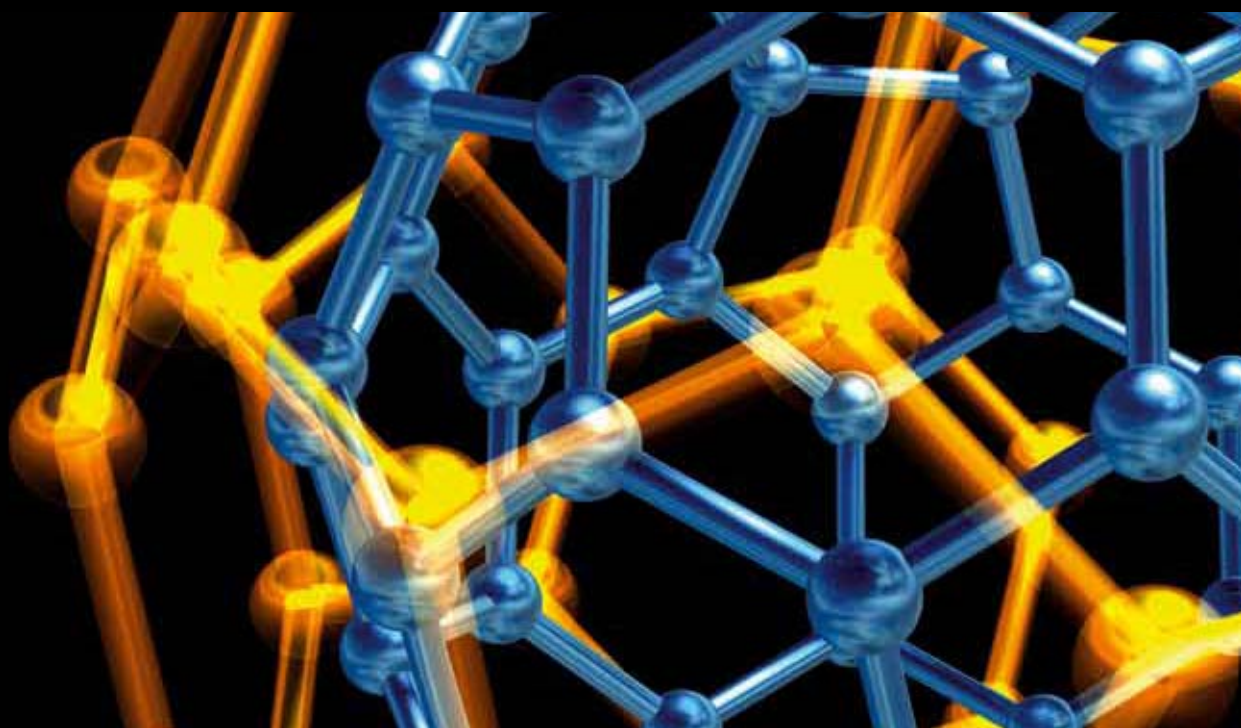


MATERIALS AND DEVICES FOR ORGANIC ELECTRONICS

GUEST EDITORS: MARISOL REYES-REYES, DAVID L. CARROLL, WERNER BLAU,
AND ROMÁN LÓPEZ-SANDOVAL





Materials and Devices for Organic Electronics

Journal of Nanotechnology

Materials and Devices for Organic Electronics

Guest Editors: Marisol Reyes-Reyes, David L. Carroll,
Werner Blau, and Román López-Sandoval



Copyright © 2011 Hindawi Publishing Corporation. All rights reserved.

This is a special issue published in volume 2011 of "Journal of Nanotechnology." All articles are open access articles distributed under the Creative Commons Attribution License, which permits unrestricted use, distribution, and reproduction in any medium, provided the original work is properly cited.

Editorial Board

Simon Joseph Antony, UK
Y. Bando, Japan
B. Bhushan, USA
Felix A. Buot, USA
Carlos R. Cabrera, Puerto Rico
John A. Capobianco, Canada
Franco Cerrina, USA
Gan Moog Chow, Singapore
Jeffery L. Coffey, USA
Dmitriy A. Dikin, USA
Dimitris Drikakis, UK
H. D. Espinosa, USA
John S. Foord, UK
E. Goldys, Australia
Lambertus Hesselink, USA
Joseph Irudayaraj, USA

Niraj K. Jha, USA
Miguel Jose-Yacamán, USA
Valery Khabashesku, USA
Yoke Khin Yap, USA
Sakhrat Khizroev, USA
Andrei Kolmakov, USA
Charles M. Lieber, USA
Charles M. Lukehart, USA
Abdel S. H. Makhlof, Germany
Constantinos Mavroidis, USA
Vincent Meunier, USA
Paolo Milani, Italy
Oded Millo, Israel
M. Grant Norton, USA
R. Lee Penn, USA
S. N. Piramanayagam, Singapore

A. M. Rao, USA
Paresh Chandra Ray, USA
Benjaram M. Reddy, India
Federico Rosei, Canada
Mehmet Sarikaya, USA
Jorge M. Seminario, USA
V. Shalaev, USA
Mahi R. Singh, Canada
Bobby G. Sumpter, USA
Xiao Wei Sun, Singapore
Weihong Tan, USA
O. K. Tan, Singapore
Thomas Thundat, USA
Boris I. Yakobson, USA
Nan Yao, USA
Chuan Jian Zhong, USA

Contents

Materials and Devices for Organic Electronics, Marisol Reyes-Reyes, David L. Carroll, Werner Blau, and Román López-Sandoval
Volume 2011, Article ID 589241, 2 pages

Variation of the Side Chain Branch Position Leads to Vastly Improved Molecular Weight and OPV Performance in 4,8-dialkoxybenzo[1,2-b:4,5-b']dithiophene/2,1,3-benzothiadiazole Copolymers, Robert C. Coffin, Christopher M. MacNeill, Eric D. Peterson, Jeremy W. Ward, Jack W. Owen, Claire A. McLellan, Gregory M. Smith, Ronald E. Nofle, Oana D. Jurchescu, and David L. Carroll
Volume 2011, Article ID 572329, 10 pages

Formation of a Molecular Wire Using the Chemically Adsorbed Monomolecular Layer Having Pyrrolyl Groups, Kazufumi Ogawa, Norihisa Mino, Shin-ichi Yamamoto, and Tadashi Ohtake
Volume 2011, Article ID 560830, 8 pages

Growth and Switching of Ferroelectric Nanocrystals from Ultrathin Film of Copolymer of Vinylidene Fluoride and Trifluoroethylene, R. Gaynutdinov, V. Fridkin, and H. Kliem
Volume 2011, Article ID 180104, 5 pages

Effect of the Thickness of Insulator Polymeric Films on the Memory Behavior: The Case of the Polymethylmethacrylate and the Polystyrene, J. A. Avila-Niño, A. O. Sustaita, M. Reyes-Reyes, and R. López-Sandoval
Volume 2011, Article ID 702464, 9 pages

Effect of Processing Parameters on Performance of Spray-Deposited Organic Thin-Film Transistors, Jack W. Owen, Natalia A. Azarova, Marsha A. Loth, Markos Paradinas, Marion Coll, Carmen Ocal, John E. Anthony, and Oana D. Jurchescu
Volume 2011, Article ID 914510, 6 pages

Inkjet-Printed Organic Field-Effect Transistor by Using Composite Semiconductor Material of Carbon Nanoparticles and Poly(3-Hexylthiophene), Chih-Ting Lin, Chun-Hao Hsu, Chang-Hung Lee, and Wen-Jung Wu
Volume 2011, Article ID 142890, 7 pages

Molecular Engineering of Nonplanar Porphyrin and Carbon Nanotube Assemblies: A Linear and Nonlinear Spectroscopic and Modeling Study, Éimhín M. Ní Mhuircheartaigh, Silvia Giordani, Donal MacKernan, Sharon M. King, David Rickard, Lisa M. Val Verde, Mathias O. Senge, and Werner J. Blau
Volume 2011, Article ID 745202, 12 pages

Editorial

Materials and Devices for Organic Electronics

Marisol Reyes-Reyes,¹ David L. Carroll,² Werner Blau,³ and Román López-Sandoval⁴

¹*Instituto de Investigación en Comunicación Óptica, Universidad Autónoma de San Luis Potosí, Alvaro Obregon 64, 78000 San Luis Potosí, SLP, Mexico*

²*Department of Physics, The Center for Nanotechnology and Molecular Materials, Wake Forest University, Winston-Salem, NC 27109, USA*

³*School of Physics, Trinity College Dublin, Dublin 2, Ireland*

⁴*Division de Materiales Avanzados, IPICYT, Camino a la Presa San José 2055, Col. Lomas 4a. sección, 78216 San Luis Potosí, SLP, Mexico*

Correspondence should be addressed to Marisol Reyes-Reyes, reyesm@iico.uaslp.mx

Received 28 August 2011; Accepted 28 August 2011

Copyright © 2011 Marisol Reyes-Reyes et al. This is an open access article distributed under the Creative Commons Attribution License, which permits unrestricted use, distribution, and reproduction in any medium, provided the original work is properly cited.

Organic electronics have attracted much attention in recent years due to their multiple advantages such as high flexibility, easy processing, low fabrication cost, and large area fabrication. These unique advantages make them highly promising for organic solar cells, organic memory devices, organic thin film transistors, organic light emitting diodes, organic photodetectors, organic sensor, and so forth. The performance of organic electronic devices is strongly dependent on the fabrication procedure as well as the processing parameters. Among various fabrication methods to implement these organic electronics devices, spray coating is emphasized because of its compatibility to large area fabrications and industrial mass productions. However, other methods, such as inkjet printing, offer, for example, to reduce the ink material consumption by drop-on-demand design. The recent advances in fabricating organic electronic devices have been carried out with the development of novel materials. Certainly, blending of organic materials to form composites has been developed to improve the properties of the devices, or to lead studies to determine some properties due to their interaction. Complementary modeling studies can be carried out to support the evidence experimentally. In this special issue, the papers address these issues.

The first paper of this special issue is on the syntheses and characterization of new low bandgap copolymers, the results indicate that one of them has the potential for obtaining highly efficient solar cells. The second paper describes the

formation and characterization of an organic molecular wire containing polypyrrolyl conjugate bonds. In addition, it is suggested that the conduction mechanism of this molecular wire might be different from semiconductors and metals. The third paper proposes, from the obtained results, that copolymer ferroelectric nanocrystals are good candidates for devices with high-density nonvolatile storage. The two subsequent papers address the influence of the processing parameters on the performance of organic memories and organic thin-film transistors. Particularly, the fourth paper presents the effect of the thickness variation of the PMMA and PSS film on the memory behavior; the different types of behavior are attributed to the metal electrodes and film thickness, whereas the organic film has minor influence. The fifth paper is on the effect of processing on film morphology and the mobility of carriers in spray-deposited organic thin film transistors. The morphology of the spray-deposited devices showing the best performance is similar with that of spin-coated devices and, for this reason, comparable performance is achieved. The sixth paper addresses the blending of materials for organic thin film transistors by using inkjet printing. Particularly, poly(3-hexylthiophene) blended with carbon nanoparticles is used as the organic semiconductor material for improving the performance of fabricated transistor. The final paper of this special issue describes the linear and nonlinear optical characterization of a composite of porphyrin with nanotube moieties.

The results show evidence that much of the optical evidence attributed to strong noncovalent binding in these systems by other authors is likely to be an artifact. Complementary molecular dynamic studies were in striking agreement with the experimental observations.

Marisol Reyes-Reyes
David L. Carroll
Werner Blau
Román López-Sandoval

Research Article

Variation of the Side Chain Branch Position Leads to Vastly Improved Molecular Weight and OPV Performance in 4,8-dialkoxybenzo[1,2-*b*:4,5-*b'*]dithiophene/2,1,3-benzothiadiazole Copolymers

Robert C. Coffin,¹ Christopher M. MacNeill,² Eric D. Peterson,¹
Jeremy W. Ward,¹ Jack W. Owen,¹ Claire A. McLellan,¹ Gregory M. Smith,¹
Ronald E. Noffle,² Oana D. Jurchescu,¹ and David L. Carroll¹

¹The Department of Physics and the Center for Nanotechnology and Molecular Materials, Wake Forest University, Winston-Salem, NC 27109, USA

²The Department of Chemistry, Wake Forest University, Winston-Salem, NC 27109, USA

Correspondence should be addressed to Robert C. Coffin, coffinrc@wfu.edu

Received 2 February 2011; Accepted 13 April 2011

Academic Editor: Román López-Sandoval

Copyright © 2011 Robert C. Coffin et al. This is an open access article distributed under the Creative Commons Attribution License, which permits unrestricted use, distribution, and reproduction in any medium, provided the original work is properly cited.

Through manipulation of the solubilizing side chains, we were able to dramatically improve the molecular weight (M_w) of 4,8-dialkoxybenzo[1,2-*b*:4,5-*b'*]dithiophene (BDT)/2,1,3-benzothiadiazole (BT) copolymers. When dodecyl side chains (**P1**) are employed at the 4- and 8-positions of the BDT unit, we obtain a chloroform-soluble copolymer fraction with M_w of 6.3 kg/mol. Surprisingly, by moving to the commonly employed 2-ethylhexyl branch (**P2**), M_w decreases to 3.4 kg/mol. This is despite numerous reports that this side chain increases solubility and M_w . By moving the ethyl branch in one position relative to the polymer backbone (1-ethylhexyl, **P3**), M_w is dramatically increased to 68.8 kg/mol. As a result of this M_w increase, the shape of the absorption profile is dramatically altered, with $\lambda_{max} = 637$ nm compared with 598 nm for **P1** and 579 nm for **P2**. The hole mobility as determined by thin film transistor (TFT) measurements is improved from $\sim 1 \times 10^{-6}$ cm²/Vs for **P1** and **P2** to 7×10^{-4} cm²/Vs for **P3**, while solar cell power conversion efficiency is increased to 2.91% for **P3** relative to 0.31% and 0.19% for **P1** and **P2**, respectively.

1. Introduction

Over the past few years considerable attention has been drawn to the field of organic photovoltaics (OPVs) [1–3]. These devices are lightweight and can be made on flexible substrates via low cost roll-to-roll processing offering a more affordable alternative to traditional PVs based on inorganic semiconductors [4–6]. However, a major stumbling block has been that OPVs are typically far less efficient than their inorganic counterparts. OPV power conversion efficiencies (PCEs) need to be dramatically improved in order to compete with inorganics and improved further still to achieve grid parity. Recently, researchers have made great

strides in improving OPV PCEs from <4% in 2001 to the current record of 8.3% [7].

These devices employ a bulk heterojunction (BHJ) architecture consisting of an active (absorbing) layer, comprised of a phase-separated network of a polymer donor (p-type) phase and a fullerene acceptor (n-type) phase sandwiched between an anode and cathode. Ideally, the domain sizes within the active layer are less than 10 nm, ensuring that excitons generated within the bulk of a phase are able to diffuse to the donor-acceptor interface, where charge separation occurs. It is also necessary that the network is bicontinuous to ensure that the separated charges have unobstructed paths to their respective electrodes. Improving

the active layer, both its components (donor and acceptor) and its morphology are the subject of the majority of OPV research and accounts for the recent upsurge in PCEs. Contributing to these improvements are (1) new processing methods that allow for more ideal phase separation and ordering within the absorbing layer [8–14], (2) new fullerene acceptor materials with elevated lowest unoccupied molecular orbitals (LUMOs) that allow for improved open circuit voltages (V_{oc}) and in-turn PCEs [15, 16] and (3) new polymer materials with highest occupied molecular orbital (HOMO) and LUMO energy levels designed specifically for OPV applications [17].

Hundreds of low bandgap polymers have now been reported for BHJ solar cells [17]. However, despite many new materials having attractive HOMO and LUMO levels for OPV applications, only a small fraction has been fabricated into efficient (PCE > 5%) organic solar cells. Frequently, this is a result of low molecular weight and poor solubility. It has been shown that higher molecular weights are generally required for good charge transport and OPV performance, while good solubility is required for the fabrication of uniform thin films and general ease of film deposition. Molecular weight and solubility often go hand-in-hand, since molecular weight growth can be terminated by precipitation of a poorly soluble polymer chain. Fortunately, M_n and solubility can often be simultaneously improved by altering the side chains on the polymer.

With this in mind, we were interested in improving the molecular weight of a copolymer (**H7**) of 4,8-didodecoxybenzo[1,2-b:4,5-b']dithiophene (C_{12} -BDT) and 2,1,3-benzothiadiazole (BT) reported by Hou et al. [18]. When employed in a bulk heterojunction solar cell, this polymer exhibited a PCE of 0.9%, which seemed particularly low considering that both BDT and BT have been employed in copolymers that have been used to fabricate highly efficient OPVs [11, 19–26]. In more recent reports of BDT copolymers, it has been suggested that linear alkoxy chains at the 4 and 8 positions of BDT result in poorly processable low molecular weight (M_w) materials [20, 26]. We anticipated that by altering the side chains from linear (dodecoxy) to branched, we could enhance M_w and solubility, and in turn improve upon the PCE of **H7**.

In this paper, we detail the syntheses, characterization, and photovoltaic properties of copolymers comprised of 4,8-dialkoxybenzo[1,2-b:4,5-b']dithiophene (BDT) and 2,1,3-benzothiadiazole, where dodecoxy (**P1**, **H7**), 2-ethylhexyl (**P2**) and 1-ethylhexyl (**P3**) side chains are employed at the 4- and 8-positions (see Scheme 1). This contribution focuses on how simple alteration of the solubilizing side chains can lead to significant increases in polymer molecular weight, charge transport, and photovoltaic performance.

2. Experimental Section

2.1. Materials. 3-Thiophenecarboxylic acid (**1**) was purchased from Matrix Scientific Co. Diethylamine, thionyl chloride, n-butyllithium (1.6 M in hexanes), trimeth-

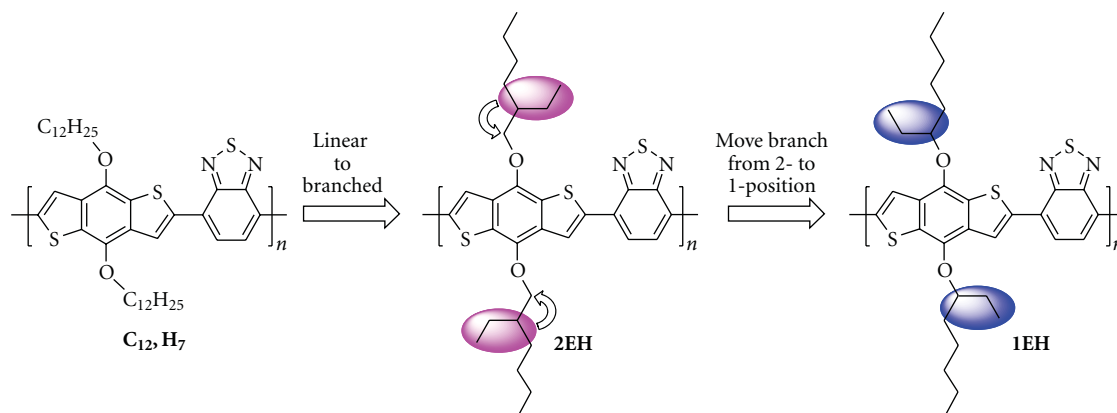
yltin chloride, *CAUTION: trimethyltin chloride is a neurotoxin, and proper precaution should be taken when handling it*, 2-ethylhexyl bromide, methanesulfonyl chloride and 3-octanol were purchased from Aldrich Chemical Co. Bromine was purchased from Fisher Chemical Co. Palladium tetrakis(triphenyl)phosphine was purchased from Acros Chemical Co. 1-bromododecane and tetrabutylammonium bromide were purchased from Eastman Chemical Co. All other reagents were purchased from common commercial sources and used without further purification unless otherwise noted. THF was dried over Na/benzophenone ketal. 4,7-Dibromo-2,1,3-benzothiadiazole (**11**) was synthesized according to literature procedure [27]. The nonstannylated 4,8-didodecoxybenzo[1,2-b:4,5-b']dithiophene (**5**) and 4,8-bis(2-ethylhexyloxy)benzo[1,2-b:4,5-b']dithiophene (**6**) were synthesized according to the published procedures [18, 21].

2.2. Instrumentation. Flash chromatography was performed on a Biotage Isolera Flash Purification System using Biotage SNAP Flash Purification Cartridges as the stationary phase. Microwave-assisted polymerizations were carried out using a CEM Discover Microwave reactor. ^1H and ^{13}C NMR spectra were recorded on a Bruker Avance DPX-300 NMR spectrometer. ^{119}Sn NMR spectra were recorded on a Bruker Avance DRX-500 instrument. UV-vis absorption spectra were recorded on an Agilent 8453 diode-array spectrophotometer operating over a range of 190–1100 nm. GC-MS were recorded on an Agilent 6850 Series GC system coupled to an Agilent 5973 mass selective detector run in electron impact mode. Infrared spectra were recorded over the 450–4000 cm^{-1} region using on a Perkin Elmer Spectrum 100 spectrophotometer with an ATR sampling accessory equipped with a diamond anvil. Gel permeation chromatography (135°C in 1,2,4-trichlorobenzene) was performed by American Polymer Standards (Ohio).

2.3. Synthesis

2.3.1. 3-Thiophenecarbonyl Chloride (2). 3-Thiophenecarboxylic acid (20.0 g, 0.156 mol) (**1**) was added to a round bottom flask equipped with a reflux condenser and stopper. Thionyl chloride (100 mL) was then added, and the mixture was allowed to reflux for 4 hours under a blanket of argon. The excess thionyl chloride was distilled over and the solution was dried on a vacuum line to yield colorless crystals (22.7 g, 99%). Characterization was consistent with published data.

2.3.2. N,N-Diethylthiophene-3-carboxamide (3). 3-Thiophenecarbonyl chloride (13.2 g, 0.09 mol) was dissolved in methylene chloride (45 mL) and added dropwise at 0°C to a solution of diethylamine (25 mL) in methylene chloride (25 mL). The solution was stirred at 0°C for 2 hours and then at RT overnight. Diethylamine (10 mL) was added and the mixture was stirred for another 2 hours. The diethylamine



SCHEME 1: Side chain variation in 4,8-dialkoxybenzo[1,2-*b*:4,5-*b'*]dithiophene (BDT) 2,1,3-benzothiadiazole copolymers.

hydrochloride precipitate was filtered off and the organic phase was extracted with water. The solution was dried over magnesium sulfate and evaporated to give a brown oil (14.1 g, 85%). Characterization of the product was consistent with the published data. *One pot procedure.* 3-Thiophenecarboxylic acid (7.0 g, 0.055 mol) and thionyl chloride (5.0 mL, 0.068 mol) were added to a round bottom flask containing methylene chloride (200 mL) and cooled to 0°C. Triethylamine (15 mL) was then added dropwise over 15 minutes resulting in the formation of a white precipitate. The mixture was allowed to warm to room temperature. After 30 minutes, diethylamine (8 mL) was added dropwise over 10 minutes. The mixture was stirred for an additional 30 minutes at room temperature. The methylene chloride was evaporated, then ether was added, and the triethylamine hydrochloride precipitate was filtered and washed with a small amount of ether. The ether was then evaporated to leave a brown oil (8.6 g, 86%).

2.3.3. 4,8-Dihydrobenzo[1,2-*b*:4,5-*b'*]dithiophene-4,8-dione (4). Compound **2** (14.1 g, 0.077 mol) was added to a 2-neck round bottom flask that was charged with dry THF (50 mL). *n*-Butyllithium (51 mL, 0.082 mmol, 1.6 M in hexanes) was added dropwise over 30 minutes at 0°C. The mixture was allowed to stir at 0°C for 30 minutes and then at RT for 2 hours. The mixture was poured over ice and allowed to sit for 4 hours. The precipitate was filtered, washed with water and methanol, and the olive green product was allowed to dry in air overnight. Typical yields range from 75%–92%. Characterization was consistent with the published data.

2.3.4. 4,8-Bis(1-ethylhexyloxy)benzo[1,2-*b*:4,5-*b'*]dithiophene (7). Compound **3** (4.0 g, 18.1 mmol) was added to a flask containing Zn dust (2.6 g, 39.8 mmol) and NaOH (85.0 mL, 25%) solution. The green mixture was allowed to reflux for 1 hour. The color changed to orange and 3-octylmethanesulfonate (7.3 g, 35 mmol), and tetrabutylammonium bromide (600 mg, ~10 mol%) were added. After 2 hours, additional portions of 3-octylmesylate (1.34 g, 6.4 mmol) and Zn dust (1.2 g, 18.3 mmol) were added, and the mixture was refluxed overnight. After cooling, the

mixture was quenched with H₂O and separated with ether. The organic phase was dried over MgSO₄ and evaporated to yield an orange oil (4.40 g, 54%). ¹H-NMR (CDCl₃), δ (ppm): 7.47 (d, 2H); 7.33 (d, 2H); 4.52 (m, 2H); 1.73 (m, 8H); 1.51 (m, 4H); 1.30 (m, 8H) 1.03 (m, 6H); 0.89 (m, 6H). ¹³C-NMR (CDCl₃), δ (ppm): 143.1, 132.4, 130.5, 125.5, 120.7, 83.7, 33.7, 32.1, 26.9, 25.1, 22.6, 14.0, 9.6. MS (EI): calc'd 446.23, found (M+1)⁺, 447.3.

2.3.5. General Procedure for Stannylation of Compounds (5), (6), and (7). Compounds **5**–**7** in dry THF (20 equiv. by wt.) were cooled to –78°C in an acetone/dry ice bath. *n*-Butyllithium (2.2 equiv, 1.6 M) in hexanes was added dropwise. The solution was stirred at –78°C for 30 minutes and at RT for 2 hours. The solution was then cooled to –78°C and freshly prepared trimethyltin chloride solution (2.4 equiv, 20% by wt. in THF) was added dropwise, and the solution was allowed to stir at RT overnight. The solution was poured into cold water and extracted with ether. The solution was washed with water, and the organic phase was dried over anhydrous MgSO₄ and evaporated to give a waxy yellow solid (>95% yield). White powders could be obtained by triturating with EtOH. No difference in purity was observed via NMR spectroscopy, nor were there differences observed in subsequent polymerization reactions. **2,6-Bis(trimethyltin)-4,8-didodecyloxybenzo[1,2-*b*:4,5-*b'*]dithiophene (8).** ¹H-NMR (CDCl₃), δ (ppm): 7.52 (s, 2H); 4.30 (t, 4H); 1.89 (m, 4H); 1.59 (m, 4H); 1.23–1.43 (m, 32H); 0.89 (t, 6H); 0.46 (s, 18H). ¹³C-NMR (CDCl₃), δ (ppm): 143.2, 140.5, 134.5, 133.0, 128.0, 73.6, 32.0, 30.6, 29.8, 29.7, 29.5, 29.4, 26.2, 22.7, 14.2, –8.3. ¹¹⁹Sn-NMR (CDCl₃), δ (ppm) relative to SnMe₃Cl (164), –33.99. **2,6-Bis(trimethyltin)-4,8-bis(2-ethylhexyloxy)benzo[1,2-*b*:4,5-*b'*]dithiophene (9).** ¹H-NMR (CDCl₃), δ (ppm): 7.53 (s, 2H); 4.20 (d, 4H); 1.54–1.64 (m, 4H); 1.33–1.88 (m, 18H); 1.04 (t, 6H) 0.96 (t, 6H) 0.46 (s, 18H). ¹³C-NMR (CDCl₃), δ (ppm): 143.3, 140.4, 133.9, 132.9, 128.0, 75.7, 40.7, 30.6, 29.3, 24.0, 23.2, 14.2, 11.4, –8.3. ¹¹⁹Sn-NMR (CDCl₃), δ (ppm) relative to SnMe₃Cl (164), –33.91. **2,6-Bis(trimethyltin)-4,8-bis(1-ethylhexyloxy)benzo[1,2-*b*:4,5-*b'*]dithiophene (10).** ¹H-NMR

(CDCl₃), δ (ppm): 7.53 (s, 2H); 4.58 (m, 2H); 1.74 (m, 8H); 1.56 (m, 6H); 1.33 (m, 8H); 1.05 (m, 6H) 0.90 (m, 6H) 0.44 (s, 18H). ¹³C-NMR (CDCl₃), δ (ppm): 141.8, 139.8, 134.4, 133.8, 128.7, 83.2, 33.7, 32.2, 27.0, 25.1, 22.7, 14.1, 9.7, -8.3. ¹¹⁹Sn-NMR (CDCl₃), δ (ppm) relative to SnMe₃Cl (164), -34.18.

2.3.6. General Procedure for Polymer Synthesis of P1–P3. Under ambient atmosphere in a 5 mL microwave tube equipped with a stir bar was added the bis(trimethyltin) monomer (0.5 mmol) along with the dibromo monomer (0.485 mmol) and 2 mL of chlorobenzene. The mixture was stirred for 5 minutes and tetrakis(triphenylphosphine)palladium(0) (2.5–5 mol%) was added to the tube and the tube was capped and set in the microwave at 200°C for 10 minutes. The viscous gel was precipitated in methanol and filtered. The solid was then added to a Soxhlet thimble and subjected to extractions with hexanes (6 hrs), THF (24 hrs), and finally chloroform (24 hrs). The chloroform extract was evaporated almost to completion, and methanol was added to precipitate the polymer, which was filtered and dried under vacuum for 24 hours.

2.3.7. Poly[(4,8-Bis(1-dodecyloxy)benzo[1,2-b:4,5-b']dithiophene-2,6-diyl-alt-2,1,3-benzothiadiazole-4,7-diyl) (P1). (Yield from CHCl₃ extract, 5–30%). FT-IR: 2917 (s), 2849 (s), 1577 (m), 1524 (m), 1489 (m), 1450 (s), 1400 (m), 1354 (s), 1273(m), 1177 (s), 1038 (br), 908 (m), 854 (m), 816 (s), 750 (w), 718 (m), 689 (m). GPC (TCB, 135°C): $M_n = 4,760$ g/mol, $M_w = 6,310$ g/mol, $PDI = 1.33$. $\lambda_{max} = 598$ nm (1,2-dichlorobenzene).

2.3.8. Poly[(4,8-bis(2-ethylhexyl)benzo[1,2-b:4,5-b']dithiophene-2,6-diyl-alt-2,1,3-benzothiadiazole-4,7-diyl) (P2). (Yield from CHCl₃ extract, 5–20%). FT-IR: 2951 (m), 2916 (s), 2850 (s), 1573 (m), 1523 (m), 1487 (m), 1447 (s), 1397 (m), 1351 (s), 1257 (w), 1175 (s), 1030 (br), 906 (m), 852 (w), 817 (s), 715 (w), 688 (w). GPC (TCB, 135°C): $M_n = 2,880$ g/mol, $M_w = 3,430$ g/mol, $PDI = 1.19$. $\lambda_{max} = 579$ nm (1,2-dichlorobenzene).

2.3.9. Poly[(4,8-bis(1-ethylhexyl)benzo[1,2-b:4,5-b']dithiophene-2,6-diyl-alt-2,1,3-benzothiadiazole-4,7-diyl) (P3). (Yield from CHCl₃ extract, 40–56%.) FT-IR: 2951 (m), 2916 (s), 2852 (s), 1575 (m), 1523 (m), 1486 (m), 1448 (s), 1396 (m), 1337 (s), 1257 (w), 1178 (s), 1019 (br), 906 (m), 853 (w), 818 (s), 715 (w), 688 (w). GPC (TCB, 135°C): $M_n = 27,100$ g/mol, $M_w = 68,800$ g/mol, $PDI = 2.54$. $\lambda_{max} = 637$ nm (1,2-dichlorobenzene).

2.4. Electrochemistry. Cyclic voltammetry (CV) was carried out using a computer-controlled Pine Model AFCBP 1 Bi-Potentiostat with PineChem software in a standard single-compartment, three electrode cell. The working electrode was glassy carbon, while the counter electrode was a platinum wire. The pseudoreference electrode was a silver wire and was calibrated against (Fc/Fc⁺). The polymer was drop-cast onto glassy carbon from a 2.5 mg/mL solution

in chlorobenzene. All measurements were carried out in degassed solutions of acetonitrile with tetrabutylammonium hexafluorophosphate (0.1 M, electrochemical grade) as the supporting electrolyte. The scan rate used was 100 mVs⁻¹. The electrochemical onsets were determined as the position at which the current differed by 2 μ A from the baseline. The highest occupied molecular orbital (HOMO) and lowest unoccupied molecular orbital (LUMO) energy levels were calculated from the oxidation (E_{onset}^{ox}) and reduction (E_{onset}^{red}) onsets, respectively, according to

$$E_{HOMO} = -(E_{onset}^{ox} + 4.8) \text{ (eV)} \quad (1)$$

$$E_{LUMO} = -(E_{onset}^{red} + 4.8) \text{ (eV)} \quad (2)$$

2.5. Powder X-Ray Diffraction. X-Ray powder diffraction data were collected at room temperature using a BRUKER P4 general-purpose four-circle X-ray diffractometer modified with a GADDS/Hi-Star detector at 40 kv and 30 mA for Cu K α radiation ($\lambda = 1.5406$ Å). The GADDS software suite was used to control the goniometer [28]. The samples were mounted on a loop and two frames were measured at $2\theta = 20^\circ$ and 50° with exposure time of 180 seconds/frame. For the inset powder diffraction spectrum, one frame was measured at $2\theta = 25^\circ$ with an exposure time of 180 seconds/frame for 10 frames. Area integration techniques were used to reproduce the single powder diffraction pattern for each frame. The powder patterns were each merged and analyzed using the EVA program to produce a single powder diffraction pattern [29].

2.6. Charge Transport Measurements. Bottom-contact thin-film transistors (TFTs) were fabricated by spin-coating (1000 rpm) polymer solutions (0.75 wt% in 1,2-dichlorobenzene) over the 1.2 cm \times 1.2 cm substrate with prefabricated device structures containing a Si gate electrode, 300 nm SiO₂ gate dielectric and 5 nm Ti/45 nm Au source-drain contacts with channel length $L = 5$ μ m and channel width $W = 1000$ μ m. Prior to spin coating, the substrates were cleaned by soaking in hot acetone, followed by isopropyl alcohol. The substrates were then cleaned in UV ozone for five minutes and rinsed with DI water. The surfaces were chemically treated by submerging the substrates for 30 min in a 17 mmol n-octyltrichlorosilane (OTS) solution in hexadecane at room temperature. The substrates were then removed and sonicated in isopropyl alcohol for 10 minutes, sonicated in chloroform for 10 minutes, and rinsed with isopropyl alcohol followed by DI water. The polymer solutions were stirred overnight prior to spin coating to ensure complete dissolution. After spin-coating, the substrates were placed in a vacuum oven overnight prior to measuring the current-voltage characteristics.

The transistors were characterized by measuring the drain current (I_D) against a sweeping gate voltage (V_{GS}) from -20 V to 60 V in the saturation regime, drain source voltage $V_{DS} = -60$ V. The measurements were made in ambient conditions using a commercially available probe station and an Agilent 4155C Semiconductor Parameter Analyzer. Five devices were measured for each material. The field-effect

mobility (μ) was calculated from the slope of the $(I_D)^{1/2}$ versus V_{GS} graph, using the relationship in

$$I_D = \frac{1}{2} \frac{W}{L} C_i \cdot \mu \cdot (V_{GS} - V_T)^2, \quad (3)$$

where C_i is the capacitance per unit area for the SiO_2 gate dielectric, W is the channel width, L is the channel length, and V_T is the threshold voltage. A value for $\partial I_D^{1/2} / \partial V_{GS}$ was determined from the slope of the linear portion of the $(I_D)^{1/2}$ versus V_{GS} plot.

2.7. Photovoltaic Characteristics. ITO-coated glass slides (Delta Technologies) were cleaned by sonication in acetone and isopropanol for 20 minutes each, followed by ozone cleaning for 30 minutes. A solution of PEDOT:PSS (Clevios P—H.C. Starck) at 1:1 PEDOT:PSS solution to deionized water was spin-coated onto the slides at 4000 RPM (resulting in a 40 nm layer). The films were then baked in a vacuum oven at 100°C for 30 minutes. Polymer solutions were then spin-coated onto the PEDOT:PSS-coated substrates. Solutions were prepared by mixing polymer and 1,2-dichlorobenzene (8 mg/mL for **P2** and **P3**, 10 mg/mL for **P1**), then they were heated (80°C for **P3**, 100°C for **P1** and **P2**) and stirred for 24 hours. The solution for **P3** was then filtered while hot (0.45 μm PVDF (Millipore)). **P1** and **P2** were spin-coated from unfiltered, hot solutions, since filtration removed much of the polymer and resulted in poorer device performance and a high frequency of devices shorting. Unfiltered solutions of **P3** resulted in devices with ~10% poorer power conversion efficiency. Optimal spin coating conditions were found to be 600 RPM for 30 s for **P1** and **P2**, and 1500 RPM for 40 s for **P3**.

The films were set to dry for 30 minutes and then placed under vacuum for thermal deposition of electrodes (2 nm LiF/100 nm aluminum). The active area of the device was 38 mm². All film thicknesses were determined via a JEOL JSPM-5200 operating in AFM tapping mode.

The current-voltage (J - V) characteristics were measured with a Keithley 236 digital source meter under simulated air mass (AM) 1.5 solar irradiation of 100 mW/cm² (Oriel 150 W Xenon Light Source). The light intensity was calibrated with a NREL calibrated reference cell (Newport). The external quantum efficiency (EQE) curve was measured using a 300 W Oriel Xenon light source passed through an Oriel Cornerstone 260 monochromator, a Merlin lock-in amplifier, a calibrated Si UV detector, and an SR 570 low noise preamplifier.

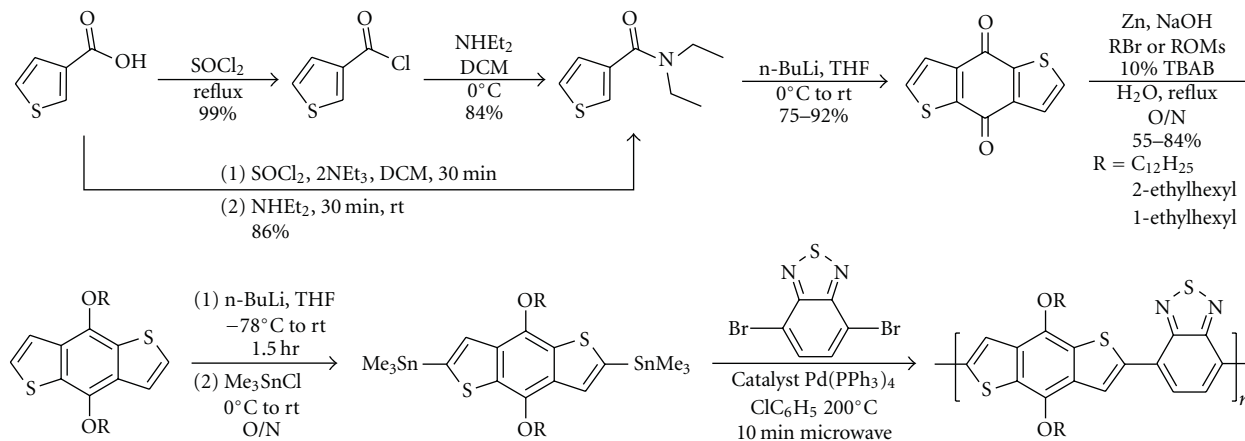
3. Results and Discussion

3.1. Synthesis and Characterization. The synthetic routes to the monomers and polymers are shown in Scheme 2. Starting from 3-thiophenecarboxylic acid (**1**), we developed a new one-pot procedure for accessing the synthetic intermediate *N,N*-diethylthiophene-3-carboxamide (**3**). This involves the *in situ* preparation of thiophene-3-carbonyl chloride (**2**) via the reaction of **1** with thionyl chloride and excess triethylamine in dichloromethane. The triethylamine functions

as a catalyst by generating the more reactive carboxylate and also reacts with the hydrochloric acid (HCl) byproduct generated by the chlorination reaction. After 30 minutes of stirring, a single equivalent of diethylamine was added to the reaction mixture containing **2** to form the desired product. The HCl generated by this reaction was reacted with the remaining triethylamine. The dione **4**, the 4,8-dialkoxy-BDTs (**5–7**) and the *bis*-stannane monomers (**8–10**) are prepared by procedures similar to those in the literature [18, 21]. The purity of monomers **8–10** was confirmed by ¹¹⁹Sn-NMR spectroscopy (See Supplementary Materials available at doi:10.1155/2011/572329) a very useful technique for determining whether there are any trace monostannane impurities in the monomers. These impurities are detrimental to molecular weight growth.

The polymers **P1–P3** were prepared by microwave-assisted Stille cross-coupling polymerization of the *bis*-stannane monomers **8–10** with 4,7-dibromo-2,1,3-benzothiadiazole (BT) in chlorobenzene using *tetrakis*(triphenylphosphine)palladium(0) ((Ph₃P)₄Pd) as the catalyst (see Scheme 1). Microwave heating was used because it is more efficient than conventional heating methods, and it has also been reported to give higher molecular weights [19, 22, 30–32]. After reaction the polymers were precipitated into methanol, collected by filtration, and transferred to a Soxhlet extractor where the material was washed with hexanes and extracted with chloroform. The chloroform-soluble fraction was isolated to ensure the material was sufficiently soluble for the preparation OPV devices. In all cases, material remained in the extraction thimble after chloroform extraction; however, the amount of this material was highly variable. For **P1** and **P2**, yields from the chloroform soluble fractions were often less than 10%, while for **P3**, yields as high as 55% were obtained. Assuming no crosslinking has occurred, the fact that material remained in the extraction thimble after chloroform extraction means that the chloroform fraction contained material with the highest molecular weight that is soluble in chloroform. The molecular weights of these fractions were determined by gel permeation chromatography (GPC) at 135°C using 1,2,4-trichlorobenzene as the solvent, and the results are summarized in Table 1. **P1**, **P2**, and **P3** were found to have weight average molecular weights (M_w) of 6.3, 3.4, and 68.8 kg/mol, respectively. Our result for **P1** differs dramatically from that of Hou et al. and may be due to differences in GPC protocols. Hou et al. ran elutions at RT using THF and found a M_w of 31.4 kg/mol, while our GPC protocol was 135°C using 1,2,4-trichlorobenzene as eluent and found our M_w to be 6.3 kg/mol. For **P2**, we find that despite several reports of the beneficial effect of the 2-ethylhexyl side chain on solubility and molecular weight, **P2** has a lower M_w than **P1**. Lastly we find that moving the ethyl branch in by one position (**P2** compared with **P3**) results in an unexpectedly large increase in M_w .

Thermogravimetric analysis (TGA) was performed on polymers **P1–P3** under argon at 5°C/min as shown in Figure 1. The results indicate that the polymers have similar thermal stabilities with the onsets of degradation ranging from 268°C and 278°C. This degradation has been attributed to the loss of the side chains [18], which is supported by the



SCHEME 2: Synthesis of 4,8-dialkoxybenzo[1,2-b:4,5-b']dithiophene (BDT) 2,1,3-benzothiadiazole copolymers.

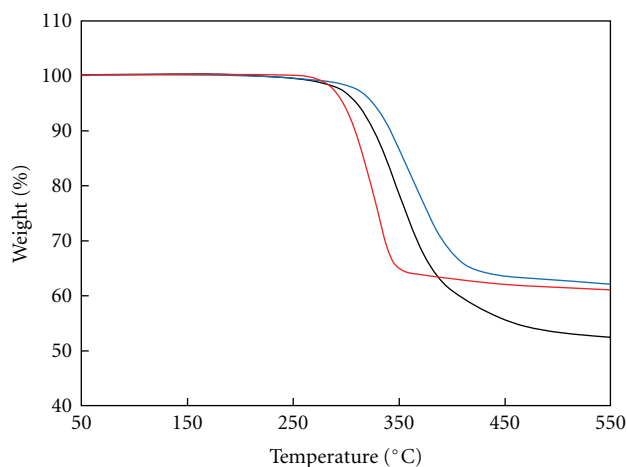


FIGURE 1: TGA curves of **P1** (black), **P2** (blue), and **P3** (red) under argon at a heating rate of 5°C/min.

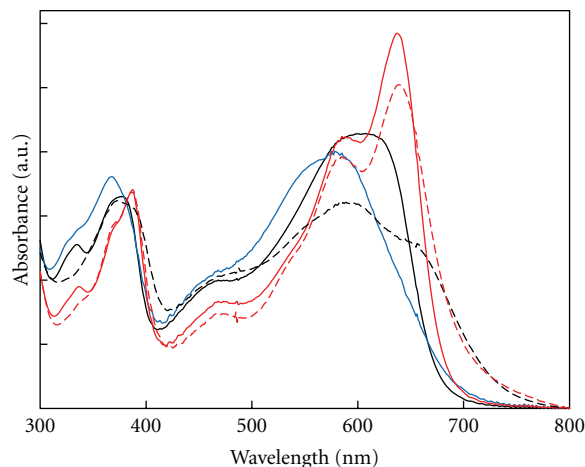


FIGURE 2: UV-Vis spectra of **P1** (black), **P2** (blue), and **P3** (red) in chloroform solution (solid) and film (dashed). Spectra are normalized by area.

fact that the **P1** which has 12 carbon side chain loses a larger weight percentage compared with **P2** and **P3**, which have 8 carbon side chains.

3.2. Optical and Electrochemical Properties. UV-visible absorption spectra (normalized by area) for polymers **P1**–**P3** in chloroform solution are shown in Figure 2. **P2** is considerably blue-shifted of **P1**, with a λ_{\max} of 579 nm compared to 598 nm for **P1**. The spectrum for **P1** is similar in shape and slightly red-shifted of Hou et al.'s **H7** (λ_{\max} = 591 nm in THF) indicating comparable molecular weight. The shape of the absorption profile for **P3** is very different from those of **P1** and **P2** with a very sharp low-energy feature dominating the spectrum—resulting in a λ_{\max} of 637 nm for **P3**. This sharp low-energy feature has been seen in other low bandgap copolymers and is indicative of high molecular weight and often high solar cell performance [11, 19, 33, 34]. UV-Vis spectra of **P1** and **P3** films (dropcast from chloroform) are shown in the dashed spectra in Figure 2. A spectrum for **P2** is not shown as dewetting of the chloroform

TABLE 1: Molecular weight of the polymers.

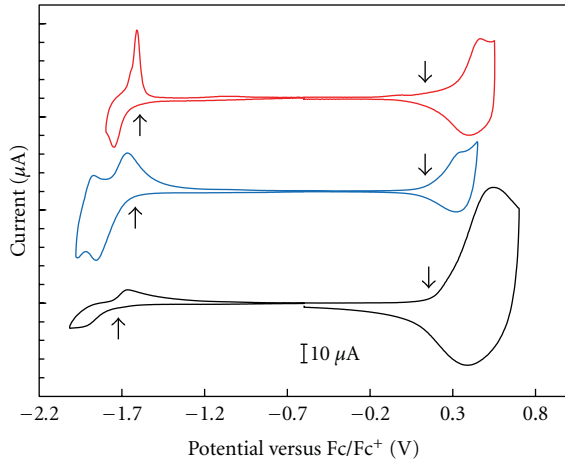
	M_n (kg/mol)	M_w (kg/mol)	<i>PDI</i>
P1	4.8	6.3	1.33
P2	2.9	3.4	1.19
P3	27.1	68.8	2.54

solution prevented preparation of uniform film. The onset of absorption for **P1** red shifts 45 nm transitioning from 685 nm in solution to 730 nm in the film. The shift in absorption onset for **P3** is not as large, shifting 35 nm from 695 nm in solution to 730 nm in the film. The film spectrum for **P1** shows the presence of low-energy shoulder that was not observed in solution, while the spectrum for **P3** is broadened but similar in shape to the solution spectrum. The optical bandgaps for both **P1** and **P3** as determined by absorption onset is 1.69 eV.

Cyclic voltammetry measurements were made on polymer films of **P1**–**P3** prepared by dropcasting chloroform

TABLE 2: Summary of optical and electrochemical properties.

	λ_{\max} (nm)	E_g^{opt} (eV)	$E_{\text{onset}}^{\text{ox}}$ (V)	HOMO (eV)	$E_{\text{onset}}^{\text{red}}$ (V)	LUMO (eV)	E_g^{elect} (eV)
P1	598	1.69	0.15	-4.95	-1.72	-3.08	1.87
P2	579	—	0.13	-4.93	-1.62	-3.18	1.75
P3	637	1.69	0.12	-4.92	-1.59	-3.21	1.71

FIGURE 3: Cyclic voltammograms of **P1** (black), **P2** (blue), and **P3** (red). Arrows indicate onsets.

solutions of the polymers onto a glassy carbon electrode (see Figure 3). The onsets of the oxidation and reduction potentials for the three polymers were comparable—not surprising given that they share a common backbone. These results are summarized in Table 2. The oxidation onsets, determined as the point where the current differed from the baseline by $2 \mu\text{A}$, were found to be 0.15, 0.13, and 0.12 V for **P1**, **P2**, and **P3** giving rise to HOMO levels of -4.95 ([18] -5.10 eV), -4.93 , and -4.92 eV, respectively. Similarly, the reduction onsets were found to be -1.72 , -1.62 and -1.59 V for **P1**, **P2**, and **P3** giving rise to LUMO levels of -3.08 ([18] -3.19 eV), -3.18 , and -3.21 eV, respectively. These results give electrochemical bandgaps of 1.87 ([18] 1.91 eV), 1.75, and 1.71 eV for **P1**, **P2**, and **P3**.

3.3. Solid State Ordering and Charge Transport. To give insight into the internal packing structure of the polymers, powder X-ray diffraction (PXRD) was used. Samples were mounted on a loop and two frames were measured at $2\theta = 20$ and 50° with exposure time of 180 seconds/frame. The integrated diffraction patterns are shown in Figure 4(a). For the inset powder diffraction pattern, 10 frames were measured at $2\theta = 25^\circ$ with an exposure time of 180 seconds/frame, then they were added together. The intensities of the diffraction patterns decrease and diffraction peaks broaden from **P1** to **P2** to **P3**, indicating that structural order within the solid polymers decreases in the order **P1** > **P2** > **P3**. This order correlates with the increasing bulk of the side chain relative to the conjugated backbone. For **P3**, which has a much higher M_w , this lack of order is further exacerbated, since order has been shown to decrease as M_w increases [35].

The peaks at low angle ($2\theta = 4.15^\circ$ for **P1**, 5.7° for **P2** and 5.5° for **P3**) are assigned to the intermolecular distance between the polymer main chains separated by an alkoxy side chain (d_1 -spacing; see Figure 4(b)). The dodecyloxy chain (**P1**) gives the longest d_1 -spacing at 21.3 \AA , while the shorter 2-ethylhexyloxy (**P2**) and 1-ethylhexyloxy (**P3**) side chains give small d_1 -spacings (15.5 and 16.1 \AA , resp.). A plot of the low angle d-spacing versus no. of carbon atoms for the three polymers gave a slope of $0.98 \text{ \AA}/\text{carbon atom}$, which is indicative of an interdigitation packing mode (see Figure 4(b)), not an end-to-end packing mode like that seen in polythiophenes [36–38]. The peaks at $2\theta = 24.9^\circ$ for **P1**, 24.5° for **P2** and 23.8° for **P3** correspond to the π - π stacking distances (d_2 -spacings) 3.58 , 3.63 , and 3.74 \AA for **P1**, **P2**, and **P3**, respectively. Despite the increase in the π - π stacking distance due to the 1-ethylhexyl chain, it is worth noting that **P3** still has a smaller π - π stacking distance than poly(3-hexylthiophene).

Thin-film transistors were fabricated from the three polymers to assess charge transport. Figure 5 shows the current-voltage characteristics of a representative device for each polymer with channel length $L = 5 \mu\text{m}$ and channel width $W = 1000 \mu\text{m}$. Here, we plot the $\log(I_D)$ versus V_{GS} in solid symbols (right axis) and the $(I_D)^{1/2}$ versus V_{GS} in open symbols (left axis) in the saturation regime ($V_{DS} = -60 \text{ V}$). The field-effect hole mobility (μ_h) of the devices shown here are $\mu_h = 1.36 \times 10^{-6}$, $9.69 \times 10^{-7} \text{ cm}^2/\text{Vs}$ and $8.17 \times 10^{-4} \text{ cm}^2/\text{Vs}$ for **P1**, **P2**, and **P3**, respectively. These values represent an underestimation of the mobility of these materials, as optical inspection of the devices demonstrated that the film partially dewets the substrates, and the material covers only a fraction of the width of the device. Thus the real width in (3) is lower than the width defined by photolithography. The on/off current ratios for the three devices presented here are 10^2 , 10^2 , and 10^4 , for **P1**, **P2**, and **P3**, respectively.

3.4. Photovoltaic Properties. The photovoltaic characteristics of the polymers were determined using a standard bulk heterojunction device architecture—ITO/PEDOT:PSS/**P1**–**P3**:PC₆₁BM/LiF/Al. The devices (0.38 cm^2) were fabricated under an inert atmosphere and tested in air. The active layers were deposited from 1,2-dichlorobenzene solutions (8 mg/mL for **P2** and **P3**, 10 mg/mL for **P1**) and the optimal weight ratios of polymer:PC₆₁BM was determined to be 1:2.5 for **P1** and **P3** and 1:2.2 for **P2**. The active layer thickness for the optimal devices as determined by atomic force microscopy (AFM) were 130 , 50 , and 100 nm for **P1**, **P2**, and **P3**, respectively. Due to the poor solubility of **P2** and its low M_w , thicker films could not be achieved even at the lowest spin speeds. The current-voltage curves for the

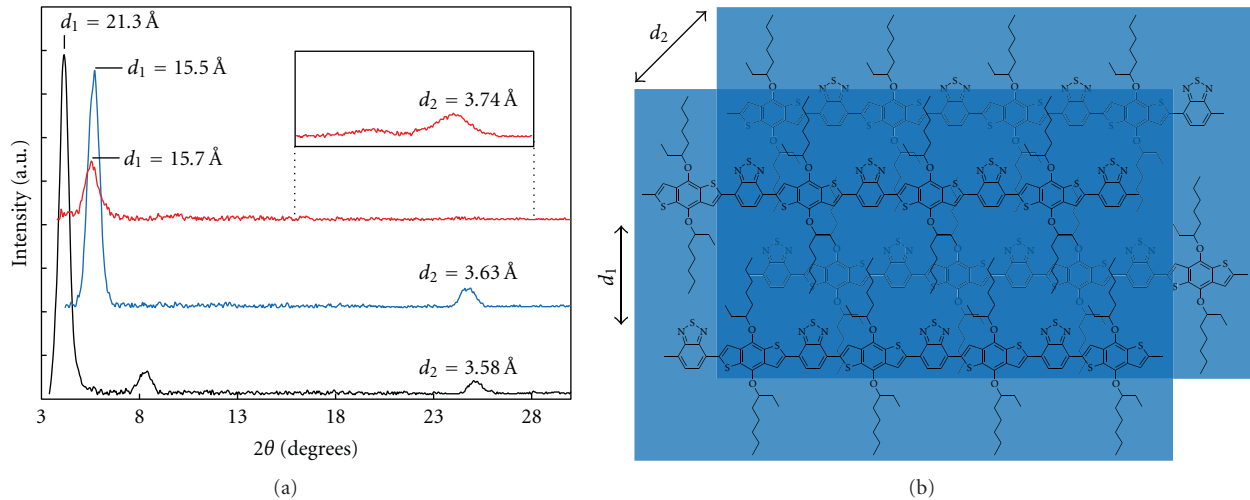


FIGURE 4: (a) Integrated powder diffraction patterns for **P1** (black), **P2** (blue), and **P3** (red). Inset: 10 frames added together for **P3**. (b) Model of packing for **P3**.

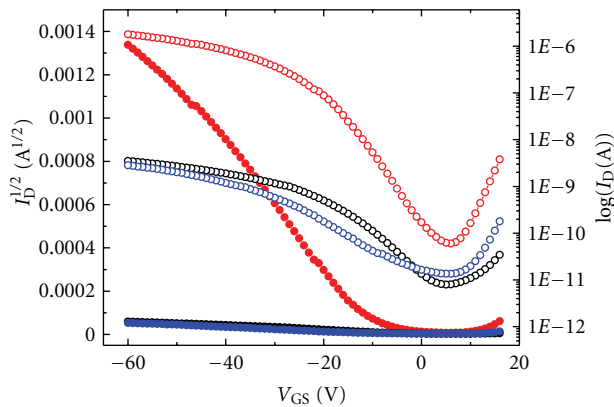


FIGURE 5: Electrical characteristics of **P1** (black), **P2** (blue), and **P3** (red). Each device has dimensions $L = 5 \mu\text{m}$ and $W = 1000 \mu\text{m}$. A plot of the $\log(I_D)$ versus V_{GS} in open symbols (right axis) and the $I_D^{1/2}$ versus V_{GS} in solid symbols (left axis) in the saturation regime ($V_{DS} = -60 \text{ V}$) are shown.

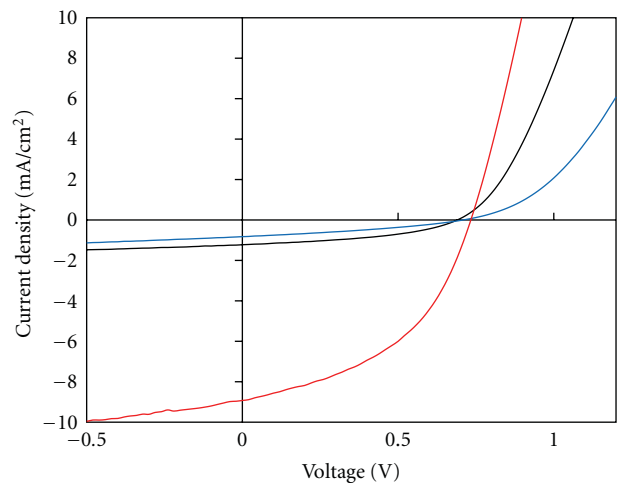


FIGURE 6: Current-voltage characteristics of bulk heterojunction solar cells based on **P1** (black), **P2** (blue), and **P3** (red) and PC_{61}BM .

best devices for each polymer are shown in Figure 6, and the results are summarized in Table 3.

Consistent with the HOMO levels determined by cyclic voltammetry, the open circuit voltages (V_{oc}) are similar for the three polymers, near 0.7 V. The short circuit currents (J_{sc}) for **P1** and **P2** are similarly low (near 1 mA/cm^2), while it is much higher for **P3** at 8.93 mA/cm^2 . The fill factors (FFs) increase with increasing M_w peaking at 0.46 for **P3**. Consequently, **P3** has a much higher power conversion efficiency (PCE) peaking at 2.91% compared with 0.31% for **P1** and 0.19% for **P2**.

The EQE spectra for the **P1** and **P2** devices (seen in Figure 7) show poor current generation across the spectrum with peak EQE less than 12%. **P3**, on the other hand, shows EQE above 30% from 330–670 nm, with a peak at 51% at 370 nm. Between 400 and 600 nm, the EQE dips, indicating that current production could be enhanced by using PC_{71}BM

TABLE 3: Photovoltaic characteristics of best devices prepared from **P1–P3** and PC_{61}BM at a polymer.

	V_{oc} (V)	J_{sc} (mA/cm^2)	FF	PCE (%)
P1	0.69	1.22	0.42	0.33
P2	0.71	0.81	0.33	0.19
P3	0.73	8.93	0.46	2.99

instead of PC_{61}BM as PC_{71}BM absorbs in this range [26]. A comparison between these devices fabricated from **P1** with Hou et al.'s **H7** [18] reveals similar V_{oc} 's (0.69 V for **P1** versus 0.68 V for **H7**) and FFs (0.42 versus 0.44) though they obtain a higher J_{sc} of 2.97 mA/cm^2 resulting in a higher PCE of 0.90%. The discrepancy in results could be explained by the fact that Hou et al. used a Ca/Al cathode and tested the devices under nitrogen, whereas we used a LiF/Al cathode and tested in air. **P3** outperforms **H7** across the board, with

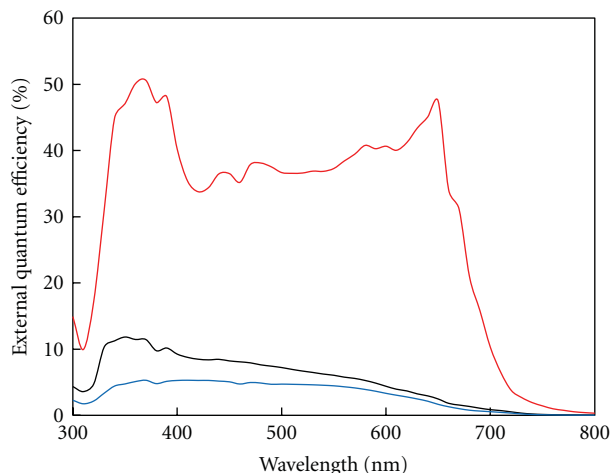


FIGURE 7: External quantum efficiency spectra of bulk heterojunction solar cells based on **P1** (black), **P2** (blue), and **P3** (red) and PC₆₁BM.

higher V_{oc} , J_{sc} , FF, and PCE, highlighting the significance of our side chain variation. It is worth noting that the **P3** solar cells were prepared from pristine DCB solution without the use of optimization techniques such as annealing or additive processing that could greatly enhance the PCE.

4. Conclusions

We prepared and characterized two new low bandgap copolymers based on BDT and BT that employ branched side chains at the 4 and 8 positions, poly[(4,8-bis(2-ethylhexyloxy)benzo[1,2-b:4,5-b'])dithiophene-2,6-diyl-alt-2,1,3-benzothiadiazole-4,7-diyl] (**P2**) and poly[(4,8-bis(1-ethylhexyloxy)benzo[1,2-b:4,5-b'])dithiophene-2,6-diyl-alt-2,1,3-benzothiadiazole-4,7-diyl] (**P3**) as well as the previously reported linear side chain analog poly[(4,8-didodecyloxy)benzo[1,2-b:4,5-b']dithiophene-2,6-diyl-alt-2,1,3-benzothiadiazole-4,7-diyl] (**P1**). Surprisingly, transitioning from the linear dodecyl side chain (**P1**) to the branched 2-ethylhexyl side chain (**P2**) results in a decrease in M_w ; however, by moving the ethyl branch in by one position relative to the polymer backbone (**P3**), we observe a dramatic increase in M_w to 68.8 kg/mol compared with 6.3 kg/mol for **P1** and 3.4 kg/mol for **P2**. This results in vastly different optical properties, with the appearance of a sharp low-energy feature in the UV-visible absorption spectrum of **P3** that is not present in the spectra of **P1** and **P2**. Despite the increase in the π - π stacking distance due to the 1-ethylhexyl branch in **P3** relative to **P1** and **P2**, the increased M_w results in a factor of 100 increase in hole mobility, and a factor of 10 increase in the PCE of bulk heterojunction solar cells. We observe a peak PCE of 2.91% for devices based on **P3** and PC₆₁BM with minimal optimization indicating that this material has the potential to make highly efficient solar cells. The use of the 1-ethylhexyl side chain, and indeed, the general technique of moving side chain branches closer to the polymer backbone is a widely applicable means of

increasing M_w in conjugated polymers, many of which have not reached their full potential because of insufficient M_w .

Acknowledgments

This work was supported by grants from FiberCell Inc. and the Department of Energy (DOE DE-FG02-07ER46428).

References

- [1] W. Cai, X. Gong, and Y. Cao, "Polymer solar cells: recent development and possible routes for improvement in the performance," *Solar Energy Materials and Solar Cells*, vol. 94, no. 2, pp. 114–127, 2010.
- [2] S. Günes, H. Neugebauer, and N. S. Sariciftci, "Conjugated polymer-based organic solar cells," *Chemical Reviews*, vol. 107, no. 4, pp. 1324–1338, 2007.
- [3] B. C. Thompson and J. M. J. Fréchet, "Polymer-fullerene composite solar cells," *Angewandte Chemie*, vol. 47, no. 1, pp. 58–77, 2008.
- [4] L. Li, G. Lu, X. Yang, and E. Zhou, "Progress in polymer solar cell," *Chinese Science Bulletin*, vol. 52, no. 2, pp. 145–158, 2007.
- [5] K. M. Coakley and M. D. McGehee, "Conjugated polymer photovoltaic cells," *Chemistry of Materials*, vol. 16, no. 23, pp. 4533–4542, 2004.
- [6] J. Y. Kim, K. Lee, N. E. Coates et al., "Efficient tandem polymer solar cells fabricated by all-solution processing," *Science*, vol. 317, no. 5835, pp. 222–225, 2007.
- [7] Press Release, 2010, <http://www.konarka.com/>.
- [8] J. K. Lee, W. L. Ma, C. J. Brabec et al., "Processing additives for improved efficiency from bulk heterojunction solar cells," *Journal of the American Chemical Society*, vol. 130, no. 11, pp. 3619–3623, 2008.
- [9] J. Peet, C. Soci, R. C. Coffin et al., "Method for increasing the photoconductive response in conjugated polymer/fullerene composites," *Applied Physics Letters*, vol. 89, no. 25, Article ID 252105, 2006.
- [10] Y. Kim, S. A. Choulis, J. Nelson, D. D. C. Bradley, S. Cook, and J. R. Durrant, "Device annealing effect in organic solar cells with blends of regioregular poly(3-hexylthiophene) and soluble fullerene," *Applied Physics Letters*, vol. 86, no. 6, Article ID 063502, pp. 1–3, 2005.
- [11] J. Peet, J. Y. Kim, N. E. Coates et al., "Efficiency enhancement in low-bandgap polymer solar cells by processing with alkane dithiols," *Nature Materials*, vol. 6, no. 7, pp. 497–500, 2007.
- [12] F. Padinger, R. S. Rittberger, and N. S. Sariciftci, "Effects of postproduction treatment on plastic solar cells," *Advanced Functional Materials*, vol. 13, no. 1, pp. 85–88, 2003.
- [13] M. Campoy-Quiles, T. Ferenczi, T. Agostinelli et al., "Morphology evolution via self-organization and lateral and vertical diffusion in polymer:fullerene solar cell blends," *Nature Materials*, vol. 7, no. 2, pp. 158–164, 2008.
- [14] J. S. Moon, C. J. Takacs, S. Cho et al., "Effect of processing additive on the nanomorphology of a bulk heterojunction material," *Nano Letters*, vol. 10, no. 10, pp. 4005–4008, 2010.
- [15] M. Lenne, G. J. A. H. Wetzelaer, F. B. Kooistra, S. C. Veenstra, J. C. Hummelen, and P. W. M. Blom, "Fullerene bisadducts for enhanced open-circuit voltages and efficiencies in polymer solar cells," *Advanced Materials*, vol. 20, no. 11, pp. 2116–2119, 2008.
- [16] Y. He, H. Y. Chen, J. Hou, and Y. Li, "Indene-C bisadduct: a new acceptor for high-performance polymer solar cells," *Journal of the American Chemical Society*, vol. 132, no. 4, pp. 1377–1382, 2010.

- [17] Y. J. Cheng, S. H. Yang, and C. S. Hsu, "Synthesis of conjugated polymers for organic solar cell applications," *Chemical Reviews*, vol. 109, no. 11, pp. 5868–5923, 2009.
- [18] J. Hou, M. H. Park, S. Zhang et al., "Bandgap and molecular energy level control of conjugated polymer photovoltaic materials based on benzo[1,2-*b*:4,5-*b'*]dithiophene," *Macromolecules*, vol. 41, no. 16, pp. 6012–6018, 2008.
- [19] R. C. Coffin, J. Peet, J. Rogers, and G. C. Bazan, "Streamlined microwave-assisted preparation of narrow-bandgap conjugated polymers for high-performance bulk heterojunction solar cells," *Nature Chemistry*, vol. 1, no. 8, pp. 657–661, 2009.
- [20] Y. Liang, D. Feng, Y. Wu et al., "Highly efficient solar cell polymers developed via fine-tuning of structural and electronic properties," *Journal of the American Chemical Society*, vol. 131, no. 22, pp. 7792–7799, 2009.
- [21] J. Hou, H. Y. Chen, S. Zhang et al., "Synthesis of a low band gap polymer and its application in highly efficient polymer solar cells," *Journal of the American Chemical Society*, vol. 131, no. 43, pp. 15586–15587, 2009.
- [22] H. Zhou, L. Yang, S. C. Price, K. J. Knight, and W. You, "Enhanced photovoltaic performance of low-bandgap polymers with deep LUMO levels," *Angewandte Chemie*, vol. 49, no. 43, pp. 7992–7995, 2010.
- [23] C. Piliago, T. W. Holcombe, J. D. Douglas, C. H. Woo, P. M. Beaujuge, and J. M. J. Fréchet, "Synthetic control of structural order in N-alkylthieno[3,4-*c*]pyrrole-4,6-dione-based polymers for efficient solar cells," *Journal of the American Chemical Society*, vol. 132, no. 22, pp. 7595–7597, 2010.
- [24] Y. Liang, Z. Xu, J. Xia et al., "For the bright future-bulk heterojunction polymer solar cells with power conversion efficiency of 7.4%," *Advanced Materials*, vol. 22, no. 20, pp. E135–E138, 2010.
- [25] H.-Y. Chen, J. Hou, S. Zhang et al., "Polymer solar cells with enhanced open-circuit voltage and efficiency," *Nature Photonics*, vol. 3, no. 11, pp. 649–653, 2009.
- [26] Y. Zou, A. Najari, P. Berrouard et al., "A thieno[3,4-*c*]pyrrole-4,6-dione-based copolymer for efficient solar cells," *Journal of the American Chemical Society*, vol. 132, no. 15, pp. 5330–5331, 2010.
- [27] K. Pilgram, M. Zupan, and R. Skiles, "Bromination of 2,1,3-benzothiadiazoles," *Journal of Heterocyclic Chemistry*, vol. 7, p. 629, 1970.
- [28] GADDS V4.1.14, *General Area Detector Diffraction System Program for Instrument Control and Data Collection*, BRUKER AXS Inc., Madison, Wis, USA.
- [29] EVA V8.0, *Graphics Program for 2-Dimensional Data Evaluation and Presentation*, BRUKER AXS Inc., Madison, Wis, USA.
- [30] F. Galbrecht, T. W. Bünnagel, U. Scherf, and T. Farrell, "Microwave-assisted preparation of semiconducting polymers," *Macromolecular Rapid Communications*, vol. 28, no. 4, pp. 387–394, 2007.
- [31] B. S. Nehls, U. Asawapirom, S. Földner, E. Preis, T. Farrell, and U. Scherf, "Semiconducting polymers via microwave-assisted Suzuki and Stille cross-coupling reactions," *Advanced Functional Materials*, vol. 14, no. 4, pp. 352–356, 2004.
- [32] K. R. Carter, "Nickel(0)-mediated coupling polymerizations via microwave-assisted chemistry," *Macromolecules*, vol. 35, no. 18, pp. 6757–6759, 2002.
- [33] J. Peet, N. S. Cho, S. K. Lee, and G. C. Bazan, "Transition from solution to the solid state in polymer solar cells cast from mixed solvents," *Macromolecules*, vol. 41, no. 22, pp. 8655–8659, 2008.
- [34] R. F. Cossigli, L. Akcelrud, and D. Z. Atvars, "Solvent and Molecular Weight Effects on Fluorescence Emission of MEH-PPV," *Journal of Brazilian Chemical Society*, vol. 16, p. 74, 2005.
- [35] R. J. Kline, M. D. McGehee, E. N. Kadnikova, J. Liu, J. M. J. Fréchet, and M. F. Toney, "Dependence of regioregular poly(3-hexylthiophene) film morphology and field-effect mobility on molecular weight," *Macromolecules*, vol. 38, no. 8, pp. 3312–3319, 2005.
- [36] T. Yamamoto, Q. Fang, and T. Morikita, "New soluble poly(aryleneethynylene)s consisting of electron-accepting benzothiadiazole units and electron-donating dialkoxybenzene units. Synthesis, molecular assembly, orientation on substrates, and electrochemical and optical properties," *Macromolecules*, vol. 36, no. 12, pp. 4262–4267, 2003.
- [37] T. Yamamoto, D. Komarudin, M. Arai et al., "Extensive studies on π -stacking of poly(3-alkylthiophene-2,5-diyl)s and poly(4-alkylthiazole-2,5-diyl)s by optical spectroscopy, NMR analysis, light scattering analysis, and X-ray crystallography," *Journal of the American Chemical Society*, vol. 120, no. 9, pp. 2047–2058, 1998.
- [38] J. Watanabe, B. R. Harkness, M. Sone, and H. Ichimura, "Rigid-rod polyesters with flexible side chains. 4. Thermotropic behavior and phase structures in polyesters based on 1,4-dialkyl esters of pyromellitic acid and 4,4'-biphenol," *Macromolecules*, vol. 27, no. 2, pp. 507–512, 1994.

Research Article

Formation of a Molecular Wire Using the Chemically Adsorbed Monomolecular Layer Having Pyrrolyl Groups

Kazufumi Ogawa,¹ Norihisa Mino,² Shin-ichi Yamamoto,³ and Tadashi Ohtake¹

¹Department of Advanced Materials Science, Faculty of Engineering, Kagawa University, 2217-20, Hayashi-cho, Takamatsu, Kagawa 761-0396, Japan

²Advanced Technology Research Laboratories, Panasonic Corporation, 3-4 Hikaridai, Seika-cho, Souraku-gun, Kyoto 619-0237, Japan

³Department of Electronics and Informatics, Faculty of Science and Technology, Ryukoku University, 1-5 Yokotani, Oe-cho, Seta, Ohtsu city, Siga 520-2194, Japan

Correspondence should be addressed to Kazufumi Ogawa, kaogawa@eng.kagawa-u.ac.jp

Received 28 February 2011; Accepted 6 April 2011

Academic Editor: Román Lopez-Sandoval

Copyright © 2011 Kazufumi Ogawa et al. This is an open access article distributed under the Creative Commons Attribution License, which permits unrestricted use, distribution, and reproduction in any medium, provided the original work is properly cited.

A molecular wire containing polypyrrolyl conjugate bonds has been prepared by a chemical adsorption technique using 1,1,1-trichloro-12-pyrrolyl-1-siladodecane (PNN) and an electrooxidative polymerization technique, and the conductivity of the molecular wire without any dopant has been measured by using AFM/STM at room temperature. When sample dimension measured was about 0.3 nm (thickness of the conductive portion in the PNN monomolecular layer) \times 100 μ m (the average width of an electric path) \times 2 mm (the distance between Pt positive electrode and the AFM tip covered with Au), the conductivity of the polymerized PNN molecular wire at room temperature was larger than 1.6×10^5 S/cm both in an atmosphere and in a vacuum chamber of 10^{-5} Torr. The activation energy obtained by Arrhenius' plots was almost zero in the temperature range between 320 and 450 K.

1. Introduction

Although there have been numerous investigations into the preparation of conductive polymers and those electric-properties, the conductivity of the conjugate bonds itself has not been measured at present.

W. A. Little reported about forty years ago from a realistic estimation of the matrix elements and density of states in certain organic polymers having a long unsaturated polyene chain that superconductivity should occur even at temperatures well above the room temperature [1]. Nevertheless, the superconductivity has not been confirmed yet at room temperatures on the organic polymer.

Chiang et al. reported that the highest room-temperature results were obtained by doping cis-(CH)_x with AsF₆ to yield cis-[CH(AsF₅)_{0.14}]_x with $\sigma(300\text{ K}) = 560\ \Omega^{-1}\text{cm}^{-1}$. The value was comparable to that obtained with single crystals of the organic metal tetrathiafulvalene-tetracyanoquinodimethane (TTF-TCNQ) [2]. But the measurement of the conductivity was carried out on the bulk polymer, and the

conductivity might contain hopping conduction between polyacetylene fibrils. Thus the conductivity of the polyacetylenic conjugated bonds itself might not be measured directly.

Moreover Intelmann et al. recently reported the preparation technique of ultrathin polypyrrolyl films using a chemically adsorbed pyrrolyl monolayer as an adhesion promoter [3].

Thereupon, we have tried to prepare superlong polypyrrolyl conjugate bonds as a molecular wire by a chemical adsorption technique with 1,1,1-trichloro-12-pyrrolyl-1-siladodecane (PNN) and an electrooxidative polymerization technique and measured the conductivity of the superlong polypyrrolyl conjugate bonds in the PNN monomolecular layer directly.

2. Experimental

2.1. Materials. A long chain molecule (PNN) having a pyrrolyl group at the molecular end, a trichlorosilyl group

at the other end, and a hydrocarbon group at the middle portion was synthesized. The pyrrolyl group, trichlorosilyl group, and hydrocarbon group were introduced for preparing conjugate bonds by electrooxidative polymerization, chemical adsorbing to a substrate surface having an active hydrogen such as hydroxyl group ($-\text{OH}$), and increasing flexibility and electric resistance of the molecule at electrooxidative polymerization, respectively. The synthesis technique will be reported elsewhere. Although there were some reports of self-assembled monolayer of pyrrole-containing alkanethiol, those were not tried this time, because the self-assembled monolayer of alkanethiol is not so durable for electro-oxidation and it cannot be prepared on an insulator such as a glass plate [4, 5].

2.2. Procedure. Samples were prepared using following steps, and measured: chemically adsorbed monomolecular layers were prepared with PNN on a Tempax (Schott Glas) glass plate ($26 \times 75 \times 1.1 \text{ mm}^3$) having two parallel Pt electrodes (deposition thickness was about 50 nm, and gap was about 2 mm) at room temperature, wherein PNN molecules anchored to the substrate surface were aligned at about 45 degrees to the length direction of the electrodes by pulling up from a washing solvent. The monomolecular layer prepared could be confirmed by multiple external reflection (MER) FTIR spectroscopy [6], and it was supported by our studies [7, 8] that monomolecular layers can be prepared on the substrates having active hydrogen such as the hydroxyl group by using chemical adsorption (CA) technique. The CA technique and alignment technique were also reported in some studies [9, 10].

And then electrooxidative polymerization was carried out in pure water by applying 40 VDC between the two Pt electrodes with a 2 mm gap at room temperature for about 7 hours. The immersion length in pure water was also 50 mm.

Although Satoh et al. tried electrochemical polymerization in an aqueous medium utilizing various electrolytes, in our experiment, the electrochemical polymerization was carried out in distilled water in order to avoid the electrolytes doping into the monolayer [11], wherein the main current at the electro-oxidation was used for electrolysis of water and a little current was used for polymerization, because many bubbles were generated at two electrode edges during the electrolysis.

For confirming the electric path, polypyrrole decoration was also carried out by applying DC voltages between the third (negative) electrode and the two (positive) Pt electrodes shorted in a pure water-containing pyrrole.

The I-V curves were measured by applying different DC voltages between the two parallel Pt electrodes at room temperature in an atmosphere and in a vacuum chamber of 10^{-5} Torr. Thus the measurements of the I-V curves were carried out using two-probe method. Measurements of activation energies were also carried out at different temperatures in the temperature range between 320 and 450 K by two-probe method in a vacuum chamber of 10^{-5} Torr.

Moreover, for searching electric paths in the monomolecular layer between the two parallel Pt electrodes and

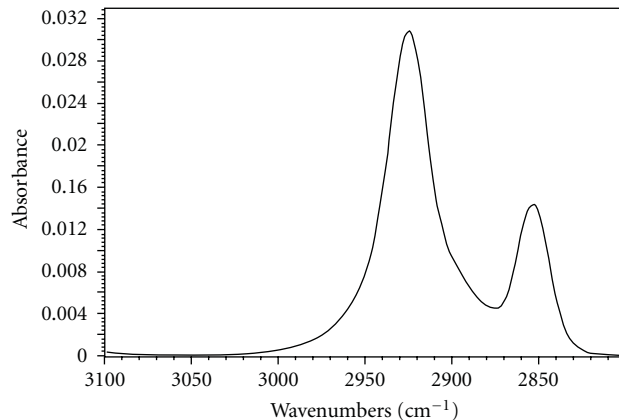


FIGURE 1: MER FTIR spectrum of the TNN monomolecular layer on a glass plate.

measuring the conductivity of these directly, an atomic force microscope (AFM, Type: SPI3800, Seiko Instruments Inc.) combined with a scanning tunneling microscope (STM) for simultaneous operation (AFM/STM) [12] was used. Thus the measurements of the conductivities at the electric path were also carried out using two probes method at room temperature in an atmosphere.

Of course, we know that four probes method should be used to measure correct conductivity of the electric path, but it was hard to attach four electrodes of micron scale to the electric path directly, because the electric path was invisible and too small.

3. Results and Discussion

3.1. Confirmation of the PNN Monomolecular Layer. The MER FTIR spectrum of the PNN monomolecular layer deposited on the $\text{SiO}_2/\text{Al}/\text{Glass}$ substrate is shown in Figure 1. Although the absorption peak due to pyrrolyl group was very weak, the split and strong absorption bands due to asymmetric CH_2 stretching (ν_{as}) and symmetric CH_2 stretching (ν_{s}) vibrations were observed clearly at 2930 cm^{-1} (ν_{as}) and 2860 cm^{-1} (ν_{s}), respectively, indicating that a densely packed PNN monomolecular layer is formed and the PNN molecules in the layer are aligned along a fixed direction [6–8].

3.2. Electrooxidation Polymerization. Electrooxidation current change is shown in Figure 2. The electric resistivity of the pure water used at the electro-oxidation was about $10^7 \Omega\text{cm}$. The electric current was almost 0 mA at the starting point of electro-oxidation. The electro-oxidation current increased gradually from 0 (starting point) to about 5 mA (3.5 hours later) with increasing the electrooxidative polymerization time. The current increased markedly at about 3.7 hours and changed up and down from about 15 mA to 30 mA in a range from several seconds' to a few minutes' cycle in the pure water after the time, as shown in Figure 2.

In this case, although the polypyrrolyl conjugate bonds contributing to electric conduction are formed self-assembly

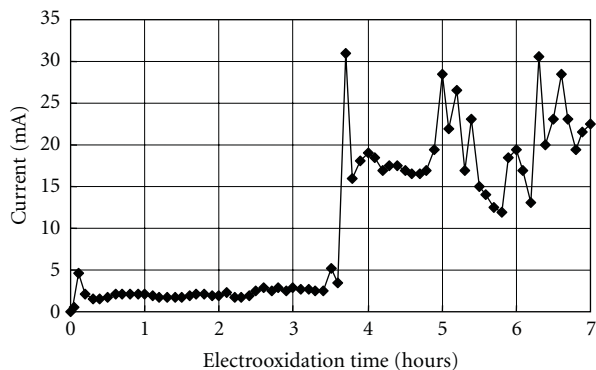


FIGURE 2: Current changes as a function of electrooxidation times.

on the substrate perpendicular to the two electrodes by the applied electric field, it is unlikely that all the molecules between two electrodes are polymerized.

3.3. Search of Electric Paths. We searched electric paths on the same sample used above by a decoration technique using electrochemical polymerization in an aqueous solution containing pyrrole. After the decoration, several black polypyrrole wires (not molecular wire, and should be only on the electric paths of the polymerized PNN monomolecular layer) connecting two electrodes of 50 mm width (immersed width in water at the electrooxidative polymerization) and 2 mm gap were observed between the two electrodes, as shown in Figures 3(a) and 3(b). All the wires were connected to Pt^+ electrode, and the widths of wires near the Pt^+ electrode were wider than those near Pt^- electrode, as shown in Figure 3(b), indicating that the polymerization of the PNN monomolecular layer occurred from the Pt^+ positive electrode.

When the polymerization is not complete in connecting between two electrodes, pure water acts as a conductor connecting between the conjugate bonds, which was formed by the polymerization of monomolecular layer from the Pt^+ electrode and connected to the Pt^+ electrode but not connected to the Pt^- electrode, and the Pt^- electrode. When the polymerization of the PNN monomolecular layer becomes completed in connecting between two electrodes, most of the electric current of about 30 mA runs through the several electric paths at the electro-oxidation time of about 3.7 hours. Then the electric current decreases or increases depending on the connection of the electric paths between two electrodes. That is, when some of the electric paths are destroyed by overconcentration of the electric current, the electric current decreases, and when the electric paths are recompleted by the electro-oxidation, the electric current increases again. This may indicate that some PNN molecular wires connected between two Pt electrodes at the current of 30 mA.

3.4. Measurement of the I-V Curves. On another sample after the polymerization, I-V curves were measured. The I-V curves measured in an atmosphere and in a vacuum chamber of 10^{-5} Torr were similar to each other, as shown in Figure 4.

Currents increased linearly with applied voltages, indicating that the sample and circuits for measuring are ohmic and the effects of adsorbed water may be neglected in an atmosphere. Thus it is easy to calculate the electric resistance of the sample, regardless of the contact resistance. However, it was difficult to calculate the electric conductivity of the electric paths (portions of the polymerized PNN monomolecular layer), because the electric paths were invisible and too small, and the number of paths and widths was unknown.

3.5. Estimation of the Activation Energy. Electric currents at temperatures in the range between 320 and 450 K were measured in a vacuum chamber of 10^{-5} Torr and plotted as a function of $1/T$ to estimate the activation energies of conductivity using Arrhenius's plots under three applied voltages of 0.01, 0.1, and 0.5 V DC, as shown in Figure 5. Slopes of three plots at applied voltages of 0.01, 0.1, and 0.5 V were almost zero, indicating that all the activation energies were almost zero between 320 and 450 K.

Accordingly, this material may be neither metallic nor semiconductor like, because if the material was metallic, the activation energy should be negative and if the material was semiconductor like, the activation energy should be positive.

3.6. Direct Measuring of Conductivity of the Polymerized PNN Monomolecular Layer. For searching the electric paths in the monomolecular layer directly and measuring the conductivity of these directly, an atomic force microscope (AFM) combined with scanning tunneling microscope (STM) for simultaneous operation (AFM/STM) [12] was used.

A topographical and a current were simultaneously obtained on the other sample without the decoration by AFM and using an AFM tip covered with Au, respectively, as shown in Figures 6(a) and 6(b). The sample used here was also one after 7 hours of electrolysis. The topographical image (Figure 6(a)) and the current image (Figure 6(b)) were obtained at the same position corresponding to the positions indicated by B (near Pt^+ electrode) in Figure 3(b).

On the topographical image (Figure 6(a)) obtained by AFM, there was no boundary between pp and p portions, because there was a PNN monomolecular layer on these portions and there was no difference of thickness. On the other hand, a boundary of the Pt^+ electrode and the PNN monomolecular layer (pp and p) could be distinguished clearly, because there was a large difference of thickness.

On the current image (Figure 6(b)) obtained using an AFM tip covered with Au, a boundary of the PNN monomolecular layer pp' and the PNN monomolecular layer p' could be distinguished clearly, because there were large differences in currents. But a boundary of the $\text{Pt}^{+'}$ electrode and the PNN monomolecular layer pp' could not be distinguished, because these currents were similar to each other, wherein the difference between the portion pp' and the portion p' was caused by the current differences of the monomolecular layer. I-V curves pp'i and p'i measured at black and white cross-points in Figure 6(b) are shown in Figure 6(c), respectively.

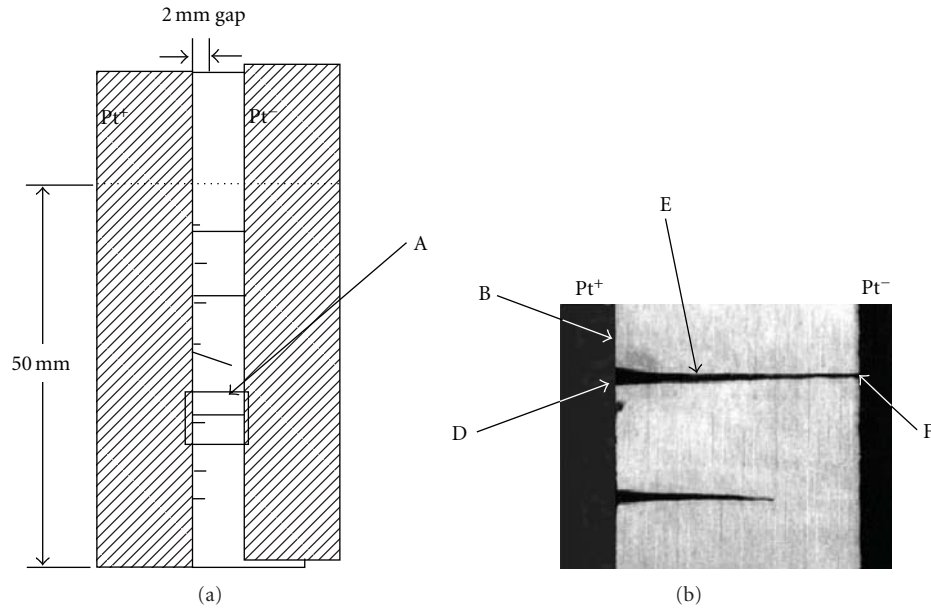


FIGURE 3: A schematic view (a) of a sample after electrooxidative polymerization. A micrograph taken after the polypyrrole decoration (b) at the position A indicated in (a). It is observed that the electric path composed of polypyrrolyl conjugate bonds grew from the Pt^+ electrode by electrooxidative polymerization.

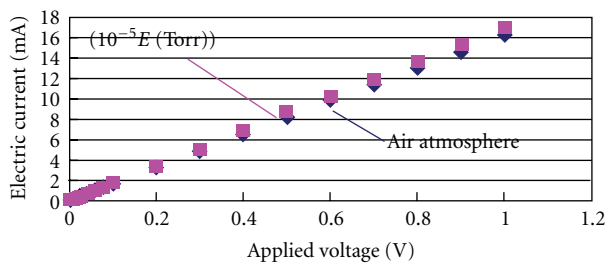


FIGURE 4: The I-V curves of a sample measured at room temperature in an atmosphere and in a vacuum chamber of 10^{-5} Torr.

On the other hand, no conduction region corresponding to pp' was observed near the Pt^- electrode.

These results may indicate that the PNN monomolecular layer at pp and pp' was polymerized and became conductive, but the PNN monomolecular layer at p and p' was not polymerized and was kept nonconductive, and conductivity at the portion of pp' is larger than that of Pt , because the thickness of Pt^+ electrode is much thicker than that of the PNN monomolecular layer and currents of these were similar to each other. The polymerization of the PNN monomolecular layer grew from the positive electrode, and the polypyrrolyl conjugate bonds contributing to electric conduction are formed on the substrate from the positive electrode to negative electrode self-assembly perpendicular to the two electrodes by the applied electric field, but the polymerization did not occur from the negative electrode.

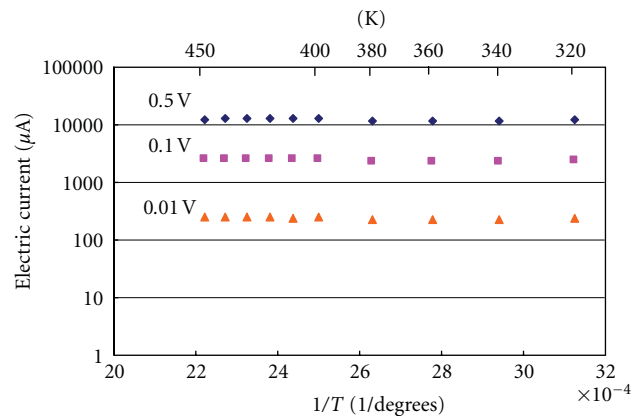


FIGURE 5: The arrhenius's plots of electric currents of a sample measured in a vacuum chamber of 10^{-5} Torr under three applied voltages of 0.01, 0.1, and 0.5 V.

Moreover, we found the electric path (molecular wire) in the monomolecular layer and measured the conductivity of the polymerized PNN monomolecular layer directly.

Figures 7(a), 7(b), and 7(c), respectively, show topographical images, current images and the I-V curves. They were obtained simultaneously on the electric path of the same sample which was used for obtaining Figure 6 by the same technique. The topographical images D1, E1, and F1, and the currents images, D2, E2, and F2, and the I-V curves D3, E3, and F3 were simultaneously obtained at the same positions corresponding to the positions indicated by D, E, and F in Figure 3(b), respectively.

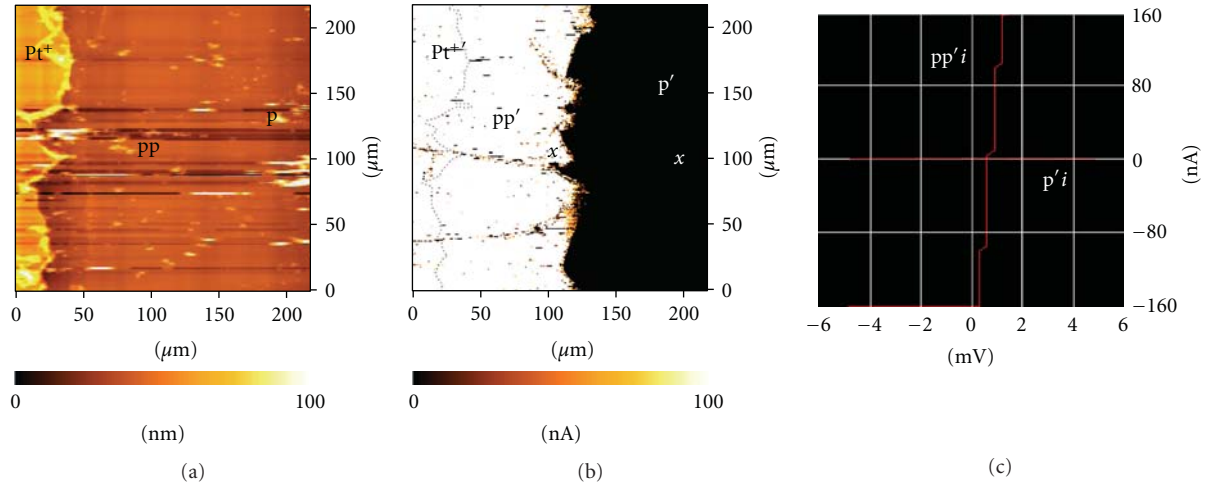


FIGURE 6: A topographical image (a), a current image (b), and I-V curves (c) simultaneously obtained at the same position corresponding to the positions B in Figure 2(b). Wherein portions pp and pp' are polymerized layer and portions p and p' are unpolymerized layer of the PNN monomolecular layer, and regions Pt⁺ and Pt⁻ are Pt electrodes. The I-V curves ppi and pi were obtained using the AFM tip covered with Au at the black and white cross-mark in (b), respectively.

On the topographical images D1 and F1 in Figure 7(a), boundaries of the polymerized portion of the PNN monomolecular layer (pp) and the Pt electrodes (Pt⁺ and Pt⁻) could be distinguished clearly, but no boundary was observed on the current images D2 and F2 in Figure 7(b).

On the other hand, on the topographical image E1 in Figure 7(a), the boundary of the polymerized portion of the PNN monomolecular layer (pp) and the unpolymerized portion (p) could not be distinguished, but, on the current image E2 in Figure 7(b), black and white portions were observed clearly. This indicates that the PNN monomolecular layer is polymerized at the bottom portion (pp') in the image E2, and the PNN monomolecular layer is unpolymerized at the top portion (p').

Accordingly, the electric path (molecular wire), which was composed of the polymerized PNN monomolecular layer containing polypyrrolyl conjugate bonds and similar to that confirmed by the above decoration technique, was observed directly by the current images. When the width of electric path without the decoration was measured directly using the AFM tip covered with Au, the average of the width was about 100 μm .

Moreover we tried to measure conductivity at the electric path (three points on the polymerized portion of the PNN monomolecular layer indicated by cross-marks on the images D2, E2, and F2 in Figure 7(b)) using the AFM tip covered with Au in an atmosphere at room temperature. The I-V curves D3, E3, and F3 obtained at the three cross marks in Figure 7(b) are shown in Figure 7(c). The slopes of the three I-V curves obtained were very similar to each other, as shown in Figure 7(c).

Although the I-V curves D3, E3, and F3 are a little different from each other, it is thought that the differences were caused by the timing shift. As the slopes of the three I-V curves were very similar to each other, the resistances

calculated with the slope of the three curves were almost the same.

When the applied voltage between Pt⁺ electrode and the AFM tip covered with Au was 0~2 mV, the slopes were about 250 nA/mV at the cross-mark on the image F2. That is, electric resistance at the F2 point was about 4 k Ω , and since the dimension of the electric path was about $0.3 \times 10^{-9} \text{ cm}^2$ (cross-sectional area of the electric path; average width of the electric path: about 100 μm and thickness of the conjugate bonds: 0.2 nm) \times 2 mm (length from the Pt electrode to the tip at the cross-mark in the image F2), the conductivity calculated was about $1.6 \times 10^5 \text{ S/cm}$. When the measurements were carried out in a vacuum chamber of 10^{-5} Torr, very similar result was also obtained. This conductivity is similar to that of Au.

On the other hand, when the measurement points of the resistance (indicated by the cross-marks) were moved from the cross-mark in F2 to the cross marks in E2 and D2 (the lengths measured from the Pt⁺ electrode to the tip on the cross marks in E2 and D2 were about 0.6 mm and 100 μm , resp.), two similar I-V curves E3 and D3 were obtained, as shown in Figure 7(c). This indicates that the electric resistance of the electric path is smaller than the contact resistance (between the polypyrrolyl conjugate bonds and the AFM tip covered with Au) and another contact resistance (between the polypyrrolyl conjugate bonds and the Pt⁺ electrode) and the circuit resistance of our setup.

Wherein if real resistance of the electric path without contact resistance was assumed to be 100 Ω at the cross-mark on the electric path in F2 (length: 2 mm), the resistances at the cross-mark E2 and D2 were calculated to be 30 Ω (length: 0.6 mm) and 5 Ω (length: 100 μm), respectively. Differences between the resistances at F2 and E2 and the resistances at F2 and D2 were 70 and 95 Ω , respectively. These values are larger than that of 1% of 4 k Ω , and as the resolution accuracy of our setup is higher than 1%, it should be easy

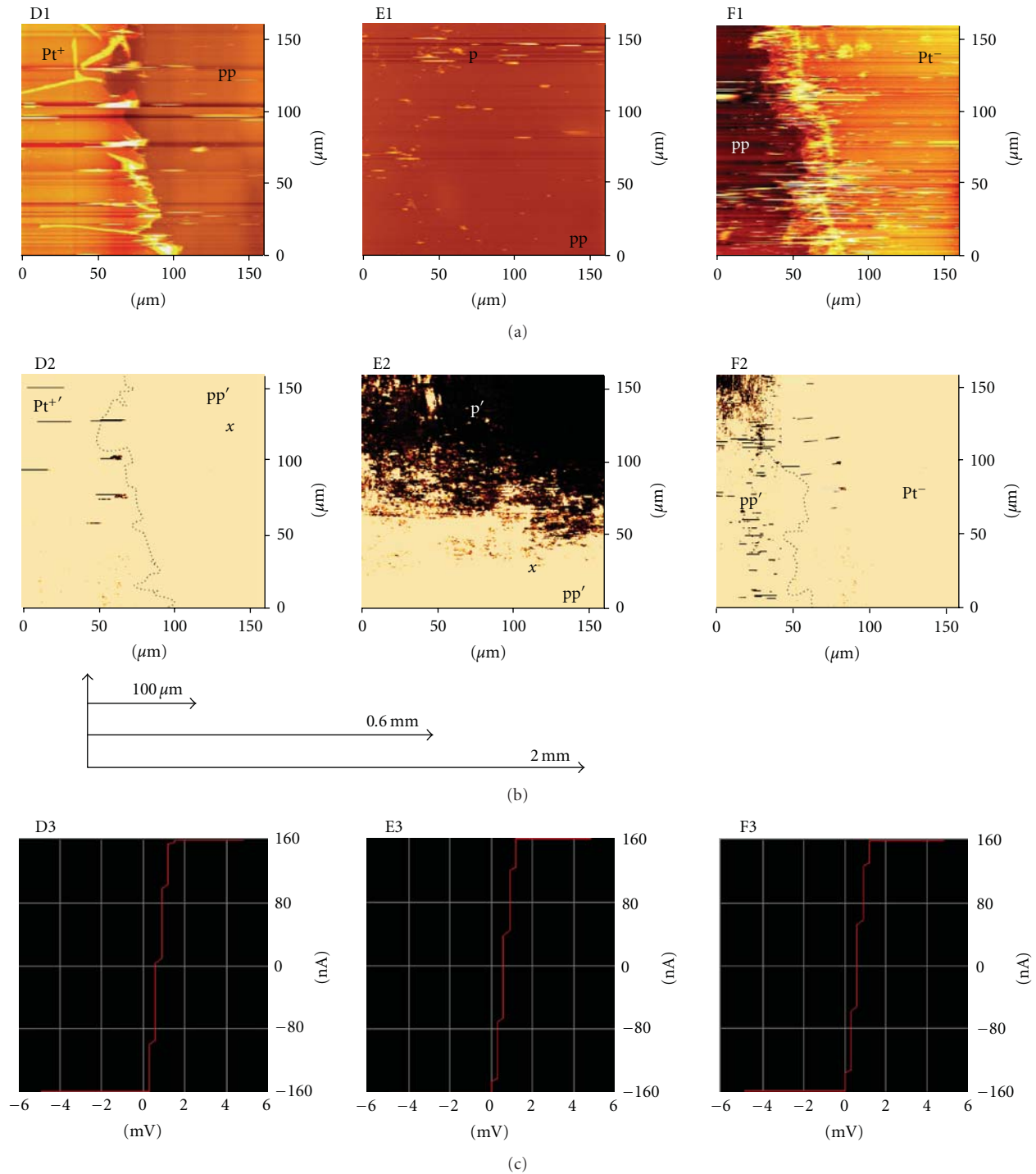


FIGURE 7: Topographical images (a), current images (b), and I-V curves (c) simultaneously obtained at the same position corresponding to the positions D, E, and F in Figure 3(b). Wherein portions pp and pp' are polymerized layer and portions p and p' are unpolymerized layer of the PNN monomolecular layer, and regions Pt⁺, Pt⁺, Pt, and Pt⁻ are Pt electrodes. The I-V curves D3, E3, and F3 were obtained using the AFM tip covered with Au at cross-marks on D2, E2, and F2 in (b), respectively.

to distinguish the difference on our setup. But any difference was not observed on the three I-V curves obtained at the cross-marks in D2, E2, and in F2. This indicates that if the contact resistance was removed, the real resistance of the electric path at 2 mm was below 100 Ω . If this assumption

is correct, the conductivity of the monomolecular layer containing polypyrrolyl conjugate bonds might be larger than 1×10^7 S/cm. This assumption may be also supported by Figure 6(b) and Figure 7(b), because the thickness of Pt⁺ and Pt⁻ electrodes (50 nm thickness), is about two hundred

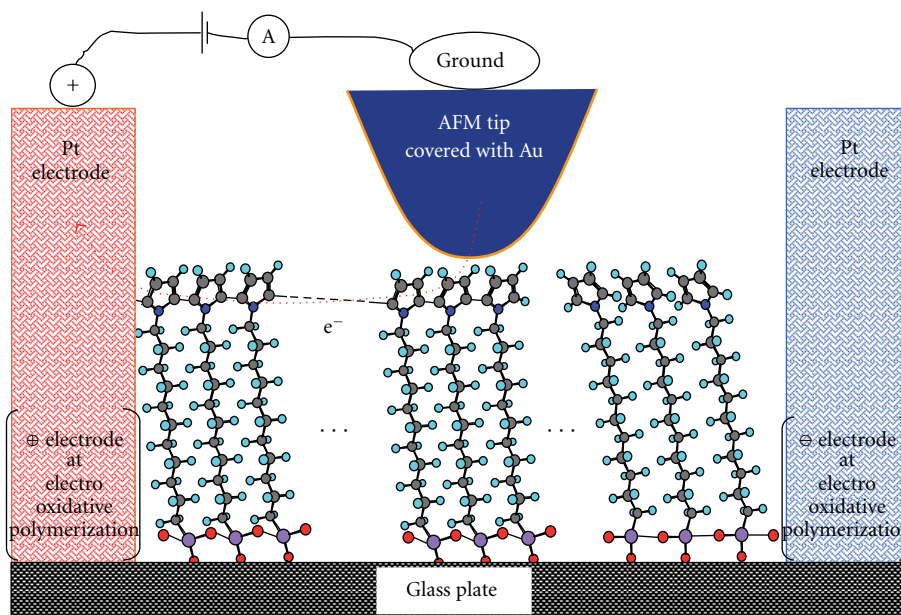


FIGURE 8: A possible electric conduction path at the current measurement shown schematically. Wherein the polypyrrolyl conjugated bonds contributing to the electric conduction in the PNN monomolecular layer are schematically shown at the molecular level. The direction of the electron running is shown by a broken line.

fifty times thicker than that of the conductive portion in the PNN monomolecular layer (0.2 nm thickness) and currents contrast obtained at Pt^+ , Pt^- , and pp' were similar to each other, as shown in Figure 6(b) and Figure 7(b).

3.7. Reasonable Electric Conduction Path. The conduction mechanism of this material may be different from semiconductors and metals. Electric conductance at the electric path is extraordinary high, as mentioned above. It is unlikely that all the PNN molecules at the electric path were polymerized to connect between the Pt^+ electrode and the tip covered with Au.

Accordingly, although it was difficult to confirm by our technique that the conjugated bond chains (molecular wires) connecting between Pt^+ electrode and the tip covered with Au were prepared in the PNN monomolecular layer, it may be reasonable to conclude that some of the molecular wires in the polymerized PNN monomolecular layer connect between Pt^+ electrode and the tip covered with Au, and these contribute mainly to the electric conductance. Thus reasonable electric conduction path at the current measurement may be schematically shown in Figure 8.

4. Conclusions

We have confirmed three times on three different samples made by the same technique using three different AFM/STM tips and obtained similar data. The conductivity of the molecular wire containing polypyrrolyl conjugate bonds should be larger than $1.6 \times 10^5 \text{ S/cm}$, and there may be a possibility of $1 \times 10^7 \text{ S/cm}$. The value is much larger than that of Au.

On the other hand, at the electric path (molecular wire), it is unlikely that all the PNN molecules were polymerized linearly to connect between Pt^+ electrode and the tip covered with Au. The polypyrrolyl conjugate bonds have no dopant.

Accordingly, it may be reasonable to conclude that only a few molecular wires made of continuous polypyrrolyl conjugate bonds were prepared in the electric path made of the polymerized PNN monomolecular layer to connect between Pt^+ electrode and the AFM tip covered with Au, and these contribute mainly to the electric conductance. The conduction mechanism of this molecular wire might be also different from semiconductors and metals.

Acknowledgment

The authors wish to thank Dr. M. Takenaga, Matsushita Electric Industrial Co., Ltd. for his helpful comments.

References

- [1] W. A. Little, "Possibility of synthesizing an organic superconductor," *Physical Review*, vol. 134, no. 6A, pp. A1416–A1424, 1964.
- [2] C. K. Chiang, C. R. Fincher Jr., Y. W. Park et al., "Electrical conductivity in doped polyacetylene," *Physical Review Letters*, vol. 39, no. 17, pp. 1098–1101, 1977.
- [3] C. M. Intelmann, U. Rammelt, W. Plieth, X. Cai, E. Jahne, and H.-P. Adler, "Preparation of ultrathin polypyrrole films using an adhesion promoter," *Journal of Solid State Electrochemistry*, vol. 11, no. 1, pp. 1–9, 2006.
- [4] C. N. Sayer and D. M. Collard, "Self-assembled monolayers of pyrrole-containing alkanethiols on gold," *Langmuir*, vol. 11, no. 1, pp. 302–306, 1995.

- [5] R. L. McCarley and R. J. Willicut, "Tethered monolayers of poly((N-pyrrolyl)alkanethiol) on Au," *Journal of the American Chemical Society*, vol. 120, no. 36, pp. 9296–9304, 1998.
- [6] N. Mino, H. Tamura, and K. Ogawa, "Analysis of color transitions and changes on langmuir-blodgett films of a polydiacetylene derivative," *Langmuir*, vol. 7, no. 10, pp. 2336–2341, 1991.
- [7] T. Ohtake, N. Mino, and K. Ogawa, "Effect of hydrocarbon chain length on arrangement of chemically adsorbed monolayers," *Langmuir*, vol. 8, no. 9, pp. 2081–2083, 1992.
- [8] K. Ogawa, N. Mino, K. Nakajima, Y. Azuma, and T. Ohmura, "Studies of molecular alignments of monolayers deposited by a chemical adsorption technique," *Langmuir*, vol. 7, no. 7, pp. 1473–1477, 1991.
- [9] J. Sagiv, "Organized monolayers by adsorption. 1. Formation and structure of oleophobic mixed monolayers on solid surfaces," *Journal of the American Chemical Society*, vol. 102, no. 1, pp. 92–98, 1980.
- [10] K. Ogawa, T. Ohtake, and T. Nomura, "Liquid crystal display having a rubbing-free photo-aligned monomolecular layer as an alignment film," *Japanese Journal of Applied Physics*, vol. 39, no. 10, pp. 5904–5911, 2000.
- [11] M. Satoh, K. Kaneto, and K. Yoshino, "Dependences of electrical and mechanical properties of conducting polypyrrole films on conditions of electrochemical polymerization in an aqueous medium," *Synthetic Metals*, vol. 14, no. 4, pp. 289–296, 1986.
- [12] K. Yano, R. Kuroda, Y. Shimada et al., "Information storage using conductance change of Langmuir-Blodgett film and atomic force microscope/scanning tunneling microscope," *Journal of Vacuum Science and Technology*, vol. 14, no. 2, pp. 1353–1355, 1996.

Research Article

Growth and Switching of Ferroelectric Nanocrystals from Ultrathin Film of Copolymer of Vinylidene Fluoride and Trifluoroethylene

R. Gaynutdinov,¹ V. Fridkin,¹ and H. Kliem²

¹Institute of Crystallography, Russian Academy of Sciences, Moscow, 119333, Russia

²Institute of Electrical Engineering Physics, Saarland University, 66041, Saarbrücken, Germany

Correspondence should be addressed to V. Fridkin, fridkin@ns.crys.ras.ru

Received 16 February 2011; Accepted 6 May 2011

Academic Editor: Marisol Reyes-Reyes

Copyright © 2011 R. Gaynutdinov et al. This is an open access article distributed under the Creative Commons Attribution License, which permits unrestricted use, distribution, and reproduction in any medium, provided the original work is properly cited.

The ferroelectric nanocrystals of the copolymer of vinylidene fluoride and trifluoroethylene P(VDF-TrFE) were grown from ultrathin Langmuir-Blodgett (LB) films on Si substrate. The annealing of ultrathin LB films with thickness of 3 monolayers (5 nm) in air in paraelectric phase at temperature 125°C was performed. The self-assembly leads to the growth of nanocrystals of ferroelectric copolymer 15–25 nm thick and 100–200 nm in diameter. The nanocrystals presumably belong to orthorhombic space group, where axis 2 is the direction of spontaneous polarization (and normal to substrate). By means of atomic force microscopy (AFM), the kinetics of ferroelectric nanocrystals growth and their switching were investigated. The obtained results confirm the conclusions that copolymer nanocrystals are candidates for high-density nonvolatile storage media devices.

1. Introduction

The first studies of independent nanocrystals of the copolymer of vinylidene fluoride and trifluoroethylene P(VDF-TrFE) were reported in [1, 2]. They were prepared from ultrathin LB films (1–5 monolayers) by annealing in air in the paraelectric phase at temperature 125°C with heating and cooling rates of 1°C per min. The ultrathin films were prepared by horizontal (Schaefer) LB method on Si substrate, investigated and described in detail in [3–5]. As shown in [1, 2], self-assembly leads to growth of nanocrystals of ferroelectric copolymer with thickness approximately 15–25 nm and diameter approximately 100–200 nm. These dimensions depend on the composition of copolymer, number of monolayers, and the annealing temperature.

Ferroelectricity in copolymer nanocrystals was confirmed by polarization reversal evident in the hysteresis of both capacitance and pyroelectric response of arrays of nanocrystals [1]. The switching time of nanocrystals arrays was measured by the pulsed current method indicating that they switch by nucleation and domain wall growth mechanisms [6]. In [7], by electron diffraction were obtained

the lattice parameters of what appeared to be single lamellar nanocrystals, corresponded to the orthorhombic space group $mm2$, which is also consistent with ferroelectricity (axis 2 is special polar direction).

The first investigation of the ferroelectric properties of individual copolymer nanocrystals have been reported in [8, 9], where polarization switching and hysteresis loops were observed with the method of piezoresponse force microscopy. As a result, the domain mechanism of switching and existence of nanodomains in the copolymer nanocrystals were proposed. The kinetic studies of copolymer nanocrystals switching were also consistent with nucleation-limited switching dynamics [6, 9].

The polarization switching kinetics was reported recently [9] for individual nanocrystals of ferroelectric of copolymer approximately 15–25 nm thick and 100–200 nm in diameter. The nanocrystal polarization could be repeatedly switched between two stable states and exhibit a well-saturated hysteresis loop. The dependence of switching time on switching voltage for an individual nanocrystal thickness $h = 25$ nm follow, the Merz exponential form $\exp(E_a/V)$ where the

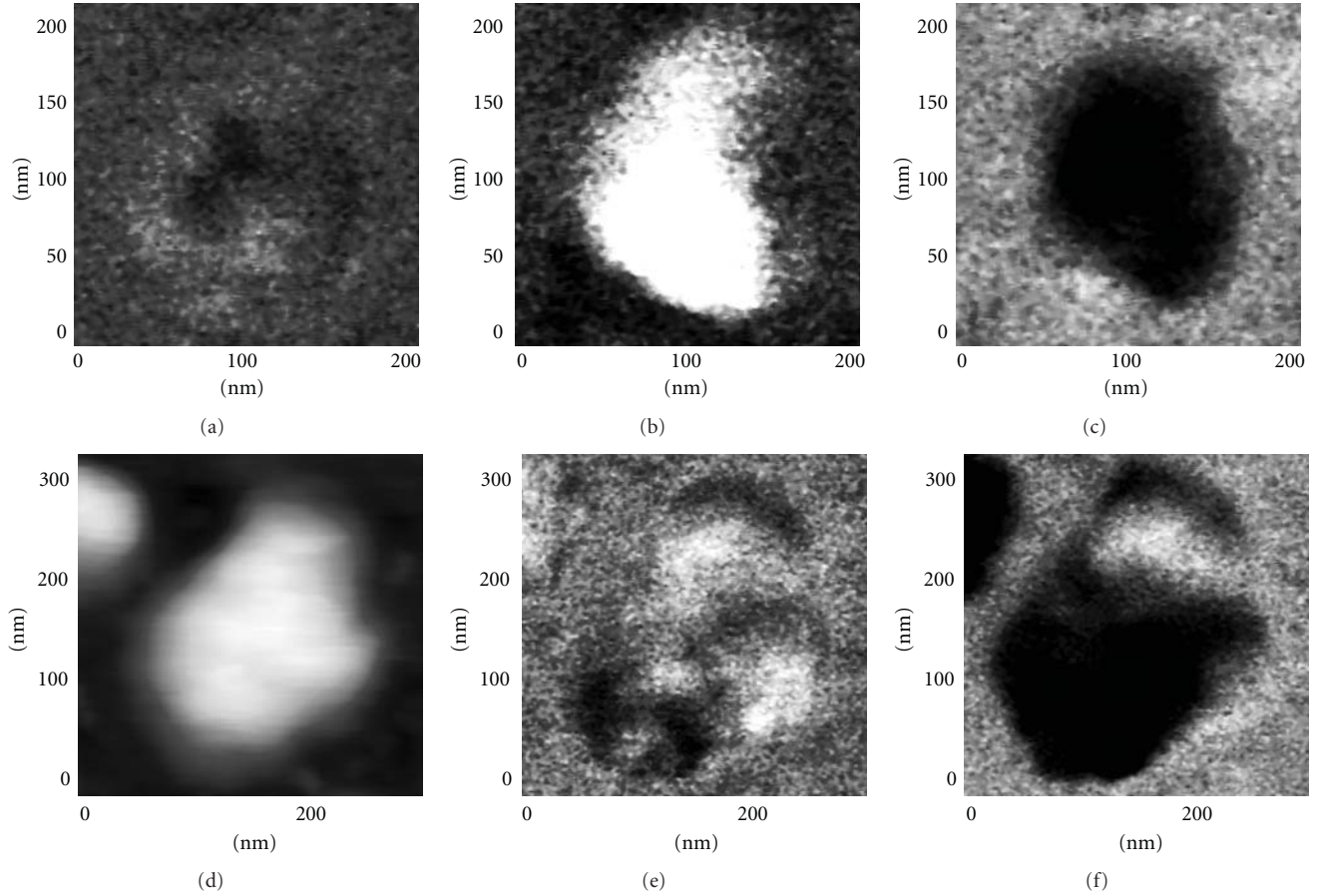


FIGURE 1: Piezoresponse images of the crystals at the following stages: nanocrystal no. 1 ($R \approx 50$ nm, $h \approx 15$ nm) (a) initial phase image, (b) after applying a bias voltage +10 V, and (c) after applying a bias voltage -10 V; nanocrystal no. 21 ($R \approx 100$ nm, $h \approx 25$ nm) (d) topography, (e) initial phase image, and (f) after applying a bias voltage -10 V.

activation field $E_a = 1, 4$ GV/m, a little larger than the value 1 GV/m obtained with thin-film capacitors of a similar 73 : 27 composition copolymer [10].

It was also found [8, 11] that the copolymer nanocrystals reveal multiple domains with opposing polarization states. What remains is to find out whether or not these crystals are homogeneous. The task of this paper is investigation of growth kinetics of the ferroelectric copolymer nanocrystals from the smallest size to the saturation, and observation of the nanocrystals switching in dependence of their size.

It is important to add, that in [9, 10] the kinetics of switching was performed for voltages $v > v_c$, where v_c is the coercive voltage.

2. The Fabrication and Observation of Nanocrystals

The nanocrystals were fabricated from a ferroelectric copolymer by Langmuir-Blodgett deposition of a copolymer consisting of 70% vinylidene fluoride and 30% trifluoroethylene. Deposition was accomplished by dispersing a 1.3% by weight solution of the copolymer in dimethyl sulfoxide on the surface of ultrapure water at room temperature and

compressed slowly to a pressure of 5 mN/m². One monolayer was transferred to a silicon substrate coated with a 50 nm thick aluminum film. To make the nanocrystals the film consisting from 3 monolayers was then heated to 125°C for different time and cooled to room temperature at a rate of 1°C per min. Measurements were carried out with a scanning probe microscope (model SOLVER P47, NT-MDT, Moscow). The growth kinetics was investigated in tapping mode by means of silicon cantilevers (model TL01, MicroMasch, Estonia) which had a lever force constant of approximately 2 N/m, a resonant frequency of 90 kHz, and tip radius of approximately 10 nm. The switching kinetics was studied with method of piezoresponse force microscopy (PFM). For the PFM measurements tips with Ti/Pt conductive coating (CSC38, MicroMash, Estonia) were used. Tip radius is about 10 nm, and lever force constant is approximately 0.05 N/m. The piezoresponse was obtained by applying an excitation voltage of amplitude 0.5 V and frequency 200 kHz to the tip and recording the amplitude and phase of the resulting tip deflection signal from the cantilever position detector with a lock-in amplifier. The piezoresponse signal is enhanced, because the bias voltage frequency was just above the piezoresponse resonance frequency, which was between 180 and 190 kHz. The PFM images consist of x - y

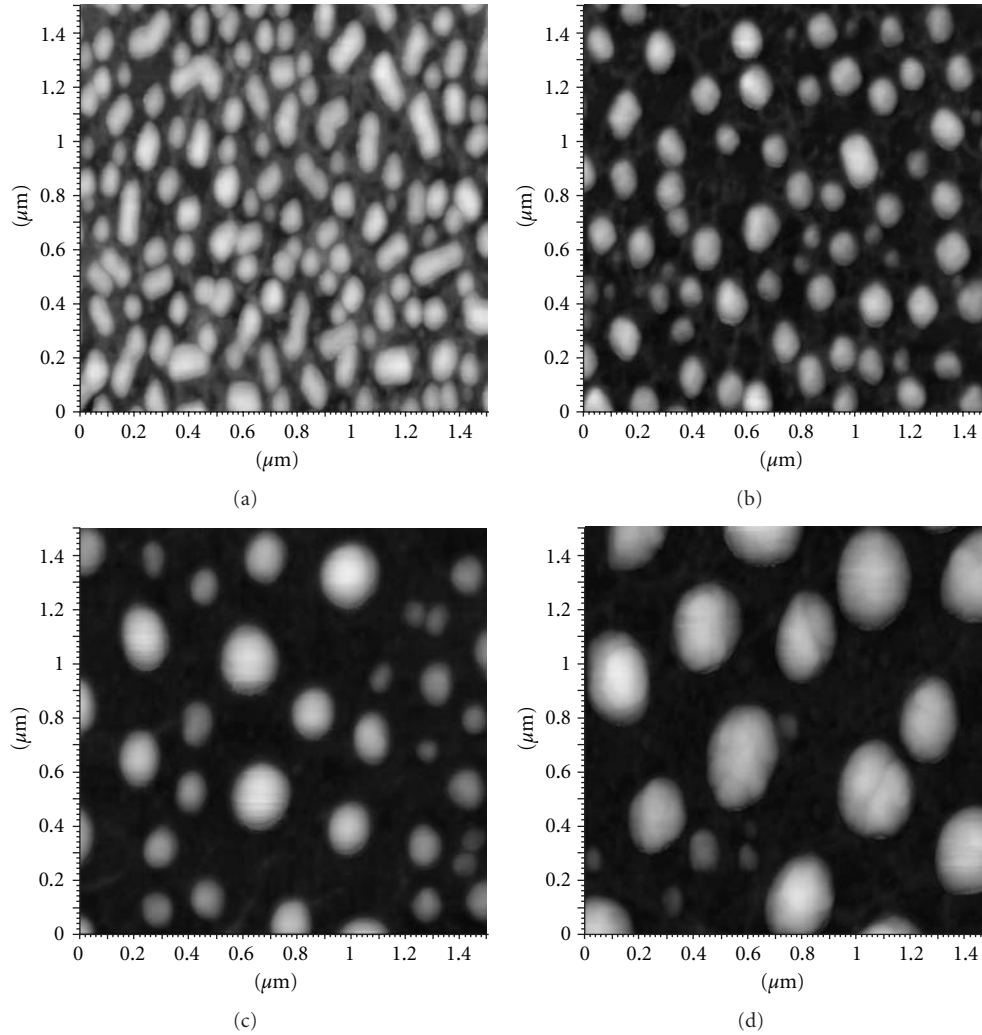


FIGURE 2: Kinetics of nanocrystals growth: (a) starting point, (b) 2 min, (c) 3 min, and (d) 4 min.

maps of the composite PFM signal, which is equal to the PFM amplitude times the cosine of the PFM phase. The measurements were carried at room temperature. The self-assembly led to the creation of nanocrystals of ferroelectric copolymer approximately 15–25 nm thick and 50–100 nm in radius with somewhat irregular shapes.

3. The Switching of Ferroelectric Copolymer Nanocrystals

As we mentioned in introduction, the switching of copolymer nanocrystals, its kinetics, and hysteresis loops were investigated in [6–9, 11]. In the present paper we revealed peculiarities in the crystal switching of different size.

Figure 1 shows the PFM image of small (Figures 1(a), 1(b), and 1(c)) and large (Figures 1(d), 1(e), and 1(f)) crystals, 1 and 2. The images of crystal 1 are obtained for following three states: (a) initial phase image (b) after applying a bias voltage of $V = +10$ V, and (c) after applying a bias voltage of $V = -10$ V. For crystal 2 the following images are presented: (d) topography image; (e) initial phase

image, and (f) after applying a bias voltage of $V = -10$ V. The comparison of the PFM images for crystals 1 and 2 shows the homogeneous switching of the small crystal 1 and inhomogeneous switching of large crystal 2. The right upper side of crystal 2 is not switched and it does not depend on the position of the tip. At the same time the all small crystals reveal homogeneous switching. Perhaps it shows that some large crystals are not monocrystals, consisting of parts with different orientation. The other explanation is the existence of so-called “stubborn” domains, which are known in ferroelectric crystals. The solution could be found by the investigation of electron diffraction patterns and transmission electron microscopy images of the copolymer nanocrystals [7].

4. Growth Kinetics

The polymer film perturbation and nanocrystal formation kinetics were analyzed in detail in [12]. Here we consider the nanocrystals growth just after film perturbation with a voltage pulse applied to the AFM tip.

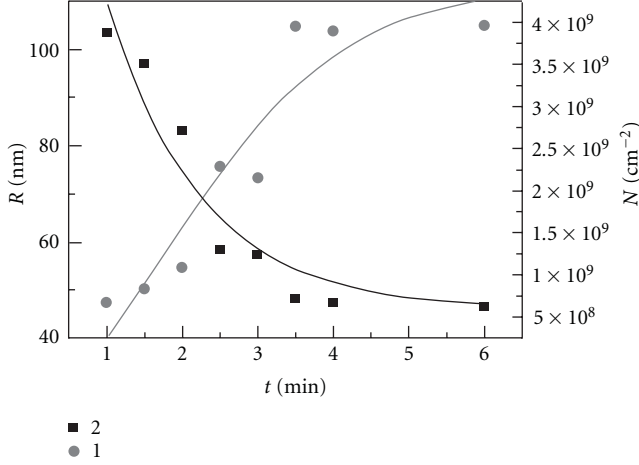


FIGURE 3: Time dependence of the middle radius R and concentration N (1: crystal concentration N , 2: middle radius of crystals R).

Just after polymer film perturbation and the first smallest crystals formation, we keep them at temperature $+125^\circ\text{C}$ for different periods of time ranging from 1 min to 6 min. This leads to the growth of crystals and a decrease of their concentration. Figure 2 illustrates 4 AFM images, corresponding to the initial stage (just after the film perturbation) and to three different period of annealing.

Figure 3 shows the time dependence of the middle radius R (curve 2, left side) and crystal concentration N (curve 1, right side). The values R and N reveal saturation at approximately same relaxation time τ . The experiment shows that the middle values of radius R and height h of the crystals grow from the initial values $R_0 \approx 50$ nm and $h_0 \approx 15$ nm to the saturation values $R_s \approx 100$ nm and $h_s \approx 25$ nm.

This kinetics based on the well-known growth kinetics from the melt [13] could be explained by the simplest model of drops merging. At $T = 125^\circ\text{C}$ we can consider material as a plate of round drops with radius R_0 , height h_0 , and concentration N_0 (on the substrate surface). As the temperature decreases the drops are crystallized in the ferroelectric phase. Let us consider one of the drops. The flow of the other drops to it is given by j_+

$$j_+ = \nu \exp\left(-\frac{u_1}{kT}\right)N. \quad (1)$$

The flow of the material in the opposite direction is given by j_-

$$j_- = \nu \exp\left(-\frac{u_2}{kT}\right)n, \quad (2)$$

where ν , u_1 , and u_2 are frequency and energy of drops merging and tearing accordingly, N and n are concentration of drops outside of drop 1 and on its surface accordingly. The condition of growth of the drops leads to $u_1 < u_2$. Then the time dependence of concentration N is given by

$$\frac{dN}{dt} = -j_+ + j_- = -a_1N + a_2n, \quad N + n = N_0, \quad (3)$$

where $a_1 = \nu \exp(-u_1/kT)$, $a_2 = \nu \exp(-u_2/kT)$, $a_2 < a_1$. The solution of (3) for $N(t=0) = N_0$ gives

$$N = N_0 \left\{ \frac{a_2}{a_1 + a_2} + \frac{a_1}{a_1 + a_2} \exp\left(-\frac{t}{\tau}\right) \right\}, \quad \tau = \frac{1}{a_1 + a_2}. \quad (4)$$

The velocity of drop growth is given by

$$\begin{aligned} \frac{dR}{dt} &= (j_+ - j_-)aS = \{a_1N - a_2(N_0 - n)\}aS \\ &\cong a_1NaR^2 \quad (a_2 \ll a_1). \end{aligned} \quad (5)$$

Here a is lattice constant and S is the length of the drop circle. The solution of (5) for $R(t=0) = R_0$ gives

$$R = \frac{1}{(1/R_0) - a_1aN_0\tau\{1 - \exp(-t/\tau)\}}, \quad (6)$$

where τ is given by (4).

This kinetics model for the average size of the drops, neglecting the size distribution, explained the saturation of the concentration and size with the same relaxation time τ . The relationship between saturated values of N_s and R_s is obtained from the conservation of copolymer mass:

$$\frac{N_s}{N_0} \left(\frac{R_s}{R_0}\right)^2 \frac{h_s}{h_0} \cong 1. \quad (7)$$

The substitution $N_s \approx 5 \cdot 10^8 \text{ cm}^{-2}$, $N_0 \approx 4 \cdot 10^9 \text{ cm}^{-2}$, $R_s \approx 100$ nm, $R_0 \approx 50$ nm, $h_s \approx 25$ nm, and $h_0 \approx 15$ nm meets (7).

5. Conclusions

The obtained results show the drastic difference in small and large nanocrystals switching. May be it is caused by heterogeneity of large copolymer nanocrystals. The size of copolymer nanocrystals at definite thickness of LB film is determined by the time and temperature of annealing.

The conditions of the ferroelectric nanocrystals growth and their switching are of critical importance to the performance of ferroelectric memory technology. Recently, the fabrication of high-density arrays of crystalline nanostructure of a ferroelectric copolymer P(VDF-TrFE) was realized by nanoembossing [14]. The results of [13, 14] show that copolymer ferroelectric crystals are candidates for high-density nonvolatile storage media devices.

Acknowledgments

The authors thank the late Professor Vitaly L. Ginzburg and Professor Stephen Ducharme for useful discussion. This paper was supported by Deutsche Forschung Gemeinschaft and by the Russian Research Foundation (RFFI-09-02-00096).

References

- [1] M. Bai and S. Ducharme, "Ferroelectric nanomesa formation from polymer Langmuir-Blodgett films," *Applied Physics Letters*, vol. 85, no. 16, pp. 3528–3530, 2004.

- [2] M. Bai, M. Poulsen, S. Ducharme, and M. Bai, "Effects of annealing conditions on ferroelectric nanomesa self-assembly," *Journal of Physics Condensed Matter*, vol. 18, no. 31, article 30, pp. 7383–7392, 2006.
- [3] S. P. Palto, L. N. Blinov, A. Bune et al., "Ferroelectric Langmuir-Blodgett films," *Ferroelectrics, Letters Section*, vol. 19, no. 3-4, pp. 65–68, 1995.
- [4] A. V. Bune, V. M. Fridkin, S. Ducharme et al., "Two-dimensional ferroelectric films," *Nature*, vol. 391, no. 6670, pp. 874–877, 1998.
- [5] S. Ducharme, S. P. Palto, V. M. Fridkin, and H. S. Nalwa, Eds., *Handbook of Thin Materials*, vol. 3, Academic Press, Moscow, Russia, 2002.
- [6] C. M. Othon, J. Kim, S. Ducharme, and V. M. Fridkin, "Switching kinetics of ferroelectric polymer nanomesas," *Journal of Applied Physics*, vol. 104, no. 5, Article ID 054109, 2008.
- [7] M. Bai, X. Z. Li, and S. Ducharme, "Electron diffraction study of the structure of vinylidene fluoride-trifluoroethylene copolymer nanocrystals," *Journal of Physics Condensed Matter*, vol. 19, no. 19, Article ID 196211, 2007.
- [8] C. J. KIM, *An intelligent decision making system for detecting high impedance faults*, Ph.D. thesis, University of Nebraska, 2008.
- [9] R. V. Gaynutdinov, O. A. Lysova, S. G. Yudin et al., "Polarization switching kinetics of ferroelectric nanomesas of vinylidene fluoride-trifluoroethylene copolymer," *Applied Physics Letters*, vol. 95, no. 2, Article ID 023303, 2009.
- [10] T. Nakajima, R. Abe, Y. Takahashi, and T. Furukawa, "Intrinsic switching characteristics of ferroelectric ultrathin vinylidene fluoride/trifluoroethylene copolymer films revealed using Au electrode," *Japanese Journal of Applied Physics, Part 2: Letters*, vol. 44, no. 42-45, pp. L1385–L1388, 2005.
- [11] C. Kittel, "Theory of the structure of ferromagnetic domains in films and small particles," *Physical Review*, vol. 70, no. 11-12, pp. 965–971, 1946.
- [12] P. Sharma, T. J. Reece, D. Wu et al., "Nanoscale domain patterns in ultrathin polymer ferroelectric films," *Journal of Physics Condensed Matter*, vol. 21, no. 48, Article ID 485902, 2009.
- [13] A. Chernov, E. Givargizov, and Kh. Bagdasarov, *Modern Crystallography*, vol. 3, Springer, Berlin, Germany, 1980.
- [14] J. Li, Y. Luo, M. Bai, and S. Ducharme, "A continuum model on the nanomesa and nanowell formation in Langmuir-Blodgett ferroelectric polymeric films," *Journal of the Mechanics and Physics of Solids*, vol. 54, no. 10, pp. 2162–2182, 2006.

Research Article

Effect of the Thickness of Insulator Polymeric Films on the Memory Behavior: The Case of the Polymethylmethacrylate and the Polystyrene

J. A. Avila-Niño,¹ A. O. Sustaita,² M. Reyes-Reyes,¹ and R. López-Sandoval²

¹ Instituto de Investigación en Comunicación Óptica, Universidad Autónoma de San Luis Potosí, Alvaro Obregon 64, 78000 San Luis Potosí, SLP, Mexico

² División de Materiales Avanzados, IPICYT, Camino a la Presa San José 2055, Colonia Lomas 4a Sección, 78216 San Luis Potosí, SLP, Mexico

Correspondence should be addressed to R. López-Sandoval, sandov@ipicyt.edu.mx

Received 2 February 2011; Revised 7 July 2011; Accepted 20 July 2011

Academic Editor: Werner Blau

Copyright © 2011 J. A. Avila-Niño et al. This is an open access article distributed under the Creative Commons Attribution License, which permits unrestricted use, distribution, and reproduction in any medium, provided the original work is properly cited.

The effect of thickness variation on the memory behavior of the polymethylmethacrylate-(PMMA)-based devices has been investigated. The PMMA film thicknesses have been varied between 5 to 300 nm, and we have found that the film thickness determines the type of behavior: ohmic, write-once-read-many-times (WORM) memory with two ON states, WORM memory with a negative differential resistance (NDR) region, and WORM memory without NDR region. The fact that similar results were obtained using different solvents to dilute PMMA (chlorobenzene, chloroform, and dimethyl sulfoxide), as well as using an other insulating polymer such as polystyrene (PS), leads to the conclusion that the phenomenon of memory depends on the aluminum electrodes, organic film thickness, and the compliance current used during the electroformation whereas the type of organic layer (PMMA or PS) has minor influence. From here, we conclude that the conductivity switching of the insulator organic film is due to the injection of aluminum particles into the film during the first voltage cycle.

1. Introduction

Since the last decade, there has been an intensive research in the field of organic electronics, the organic memory devices being one of the emerging research areas in this field. A considerable number of architectures as well as materials for the development of devices with memory effect has been proposed [1–3]. Among the principal thin-film structures that have been reported are metal-organic insulator-metal (MIM) [4–14], metal-organic-metal-organic-metal [15–17], metal nanoparticles embedded in the organic layer in MIM architecture [18], devices where the embedded metal nanoparticles are replaced with organic particles such as fullerenes [19–21], and carbon nanoshells [22]. From all, the simplest architecture and one of the first to show memory behavior was the MIM architecture. One of the pioneer works was realized by Simmons and Verderber [23], who

used a thin film of SiO₂ inorganic insulator with a thickness in the order of nanometers between two metallic electrodes. The authors explained this phenomenon as the creation of charge traps in the inorganic film due to an electric field. However, different theories have been proposed in order to explain such phenomena, one of them by Thurstans and Oxley [24] who proposed the effect of electroformation. They mentioned that once a voltage was applied on the device, an electric field was induced and this field moves the metal particles coming from the electrodes into the organic film, where they form metallic islands. These islands are responsible of the charge conduction by tunneling through filamentary pathways. The same kind of memory behaviors, mentioned before, has been reported using organic insulators. For example, Tondelier et al. [4] have obtained basically the same effect reported by Simmons and Verderber [23] in Al/pentacene /Al devices, that is, the threshold voltage varies

almost linearly with the thickness of the organic film and, above certain critical thickness, the organic layer behaves like an insulator. On the other hand for thinner films, the device has an ohmic behavior. They argued that this phenomenon is due to the possible inclusion of aluminum nanoparticles in the pentacene film during the evaporation of the top electrode. On the other hand, Cölle et al. [5] explain the memory effect in organic devices arguing the existence of multiple filament pathways, which appear and disappear at the same place in the organic film at the moment of write and erase of the device, respectively. These filaments were associated with spots observed by infrared microscopy images. They have used polymers with different chemical structures and bandgaps, such as polystyrene (PS) and polyspirofluorene as organic insulator layers, and the thickness of spin-coated polymer films were varied between 60 nm and 170 nm. Their results suggest that an oxide film, inherent to the aluminum bottom electrode, is responsible for this phenomenon. In a last paper [6], this group included deliberately an Al_2O_3 film in polyspirofluorene MIM devices and, from here, they have concluded that the memory effect is related to a native aluminum oxide layer. This layer is responsible for the resistive switching effect and the organic film only acts as a series resistance. However, other authors have found bistable electrical switching in PS and other insulator polymer thin films (50–400 nm) fabricated by a glow discharge deposition technique, although they have used gold electrodes [25–27]. Even more, Joo et al. found that spin-coated PS and polymethyl methacrylate (PMMA) films sandwiched between a bottom aluminum electrode (80 nm) and top copper electrode (80 nm) did not show memory behavior [28]. Therefore, the memory behavior of insulator organic films depends on many experimental parameters, which must be studied.

In this work we use PMMA and PS as organic insulator layers of MIM devices. We have studied the effect of the film thickness on the memory behavior, varying their thicknesses from 7.5 nm up to 300 nm. We have found that the thin PMMA films as well as thin PS films show a WORM memory behavior beyond a critical thickness. In general, the state ON of these devices is obtained at 2 V. In addition, three different kinds of solvents were used in the spin-coating process and these solvents do not change the electrical behavior of the devices. This indicates that the effect is only associated to the film thickness. Furthermore, our results show that aluminum electrodes in Al/organic insulator/Al devices are responsible for WORM memory and that the type of organic insulator layer (PMMA and PS) only has a minor influence. Therefore, our results suggest that conductive filaments are formed under electrical stress that causes migration of electrode material into the polymeric film.

2. Experimental

Our device architecture is a sandwich type metal/organic insulator/metal deposited over a glass substrate (Figure 1). The substrates of Dow corning glass were ultrasonically cleaned, successively, in acetone, methanol, and isopropyl alcohol for

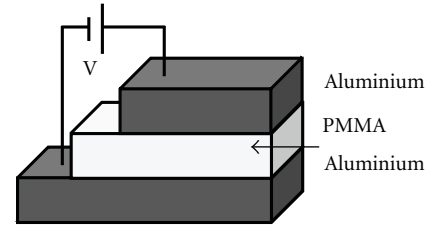


FIGURE 1: Schematic diagram of the memory device.

20 minutes at each step, dried in an oven at 50°C, and, finally, they were exposed in a UV-ozone ambient for 45 minutes. The bottom electrode was deposited by thermal evaporation at a pressure of 1×10^{-6} Torr. The metal used in these devices was aluminum, and, as organic films, we have used PMMA (Aldrich, Mw = 15,000) as well as PS (Aldrich, Mw = 97,400). After the deposition of the bottom aluminum electrode, the polymer solution was deposited by the spin-coating method at 4500 rpm for 40 seconds. The PMMA and PS were diluted in different solvents such as chloroform (CF), chlorobenzene (CB), and dimethyl sulfoxide (DMSO). The solutions prepared at different concentrations of PMMA (Table 1) were magnetically stirred by around 12 hours and then spin coated on the bottom electrode. The films were annealed at 80°C for 90 minutes in a controlled atmosphere of nitrogen. After that, the top aluminum electrode was evaporated using the same process described before for the bottom electrode. The thickness of both aluminum electrodes was around 50 nm and the active area of the cells was 6 mm². The thicknesses of the thermally evaporated metal electrodes and organic film were measured using an Alpha Step 500 surface profiler (from Tencor Instruments, Inc.). Electrical characterization of the devices was performed in ambient condition without any device encapsulation. The *I-V* measurements were performed by using a Keithley 236 source measure unit. The compliance current was set, in general, at 100 mA. The contacts between the Al electrodes and the Keithley source unit were made with gold spring probes. In general, the sweeps of the voltages were continuously applied and the speed of these measurements was 2 V/s. The electrical properties of the MIM devices were similar, no matter the polarity between the top and bottom electrodes during the voltage sweeps. The top electrode and the polymer films of the devices were examined by using scanning electron microscopy (SEM) and atomic force microscopy (AFM). SEM images were taken using an FEI FEG-XL30 operating at 8 kV.

3. Results and Discussion

First, we examined the memory behavior as a function of the PMMA film thickness obtained from the spin coating of PMMA/CB, PMMA/CF, and PMMA/DMSO solutions. The PMMA films are embedded between two aluminum electrodes. Figure 2 shows typical *I-V* curves of PMMA (using CB) thin-film devices, which are presented on semilogarithmic scale. The curves were measured applying a bias voltage between both electrodes and with a compliance current set

TABLE 1: Al/PMMA/Al devices fabricated by using different solvents.

Concentration	Solvent	Thickness	Response	Current (mA) read at 1 V
2.5 mg/mL	CB	7.5 nm	Ohmic	5×10^{-2}
5 mg/mL	CB	17 nm	WORM with two ON states	5×10^{-2} ON ₁ 10^{-3} ON ₂
10 mg/mL	CB	22 nm	WORM with NDR	10^{-3}
40 mg/mL	CB	90 nm	WORM	10^{-4}
60 mg/mL	CB	140 nm	WORM	10^{-6}
120 mg/mL	CB	250 nm	Insulator	10^{-9}
0.7 mg/mL	CF	5 nm	Ohmic	5×10^{-2}
1.5 mg/mL	CF	11 nm	WORM with two ON states	5×10^{-2} ON ₁ 10^{-3} ON ₂
2.5 mg/mL	CF	22 nm	WORM with NDR	10^{-3}
5 mg/mL	CF	37 nm	WORM	10^{-4}
20 mg/mL	CF	160 nm	WORM	10^{-7}
30 mg/mL	CF	300 nm	Insulator	10^{-9}
4 mg/mL	DMSO	5 nm	Ohmic	5×10^{-2}
9 mg/mL	DMSO	15 nm	WORM with two ON states	5×10^{-2} ON ₁ 10^{-3} ON ₂
17.5 mg/mL	DMSO	25 nm	WORM with NDR	10^{-3}
40 mg/mL	DMSO	40 nm	WORM	10^{-4}

at 100 mA, which is the default compliance current of the Keithley 236 source measure unit. The first voltage sweep was performed from 0 to 8 V, then from 8 to -8 V, and finally from -8 to 8 V. The I - V curves show different responses as a function of the thickness of the organic film (Figures 2(a)–2(d)). For a thickness around 7.5 nm, the device shows an ohmic behavior with no threshold voltage and the current is the order of 100 mA (Figure 2(a)). This behavior can be readily understood and it is related with electron tunneling processes [29]. In addition, it is also possible that some metallic particles are introduced into the polymer during the evaporation process of the top electrode forming metallic filaments.

As the film thickness continues increasing, the I - V curves begin to show memory effect with different behaviors, such as is observed in Figures 2(b)–2(d). The devices with thicknesses around 17 nm (Figure 2(b)) exhibit an abrupt transition occurring at a threshold voltage (V_{th}) of 2 V, where the I - V curve changes from a high-impedance (OFF) state to low-impedance (ON) state. In higher voltage region ($|V| > V_{th}$), during the positive and negative voltage sweeps, the electrical current was saturated. When the voltage was scanned from 8 to -8 V, the memory device switched to other ON state around -6 V. This implies that devices with this thickness and in this voltage interval show multilevel conductance states [5, 10]. After that the device switched to the second ON state, the conductivity remains basically at the same state during the following sweep cycles indicating that we have a write-once-read-many times (WORM) memory.

A third type of behavior occurs for a PMMA film with a thickness around 22 nm (Figure 2(c)). The device initially exhibited a low-conductivity state (the OFF state) and, as the applied voltage was increased, a threshold voltage at 2 V was observed. The device switched to ON state and exhibited a region of negative differential resistance (NDR), which only occurs in the first positive sweep ($0 \rightarrow 8$ V). During the opposite voltage sweep ($8 \text{ V} \rightarrow 0 \text{ V} \rightarrow -8 \text{ V}$), the device remains in the ON state and it does not show a threshold voltage. A second sweep shows that once the device has reached its ON state, this remains there (Figure 2(c)). In fact, this state was also observed over 1000 read voltages and even when the power is turned off. Once again, we have obtained a WORM memory. When the film thickness is bigger than those previously described, the memory devices present the same WORM behavior (Figure 2(d)). However, the electrical current of the ON state decreases respect to the thinner organic films (Figures 2(b) and 2(c)), such as is shown in Table 1. In addition, Figure 2(d) shows that the device, for thick films (140 nm), has very low conductivity. Finally, when the polymer film is thick enough (around 300 nm), the device has an insulator behavior. In general, all the WORM memory devices reported in this work, no matter the thickness, show good retention for thousands of cycles and even days, without any encapsulation such as is shown in Figure 3 for an Al/PMMA/Al device with a thickness of 22 nm.

To study the effect of different solvents on the electrical response of PMMA thin films, memory devices were fabricated using CF and DMSO. It was observed that I - V measurements are independent of the used solvent (CB, CF, and DMSO) and only depend of the thickness of the films. This means that the same memory behavior was observed at a specific range of thickness, no matter the solvent employed. However, as is shown in Table 1, the thickness depends on the used solvent as well as of the PMMA concentration. In general, we obtain that PMMA films (i) with thicknesses smaller than 10 nm show ohmic behavior, (ii) with thicknesses between 11–20 nm show WORM memory with two ON states, (iii) with thicknesses between 20–25 nm show WORM memory with NDR, (iv) with thicknesses bigger than 25 nm only show WORM memory, and, finally, (v) with thicknesses bigger than 300 nm show an insulator behavior. For the PS memory devices fabricated by using different solvents, the results were similar to those obtained with PMMA, such as is shown in Figure 4. We found only small differences in the thickness ranges for the different memory behaviors. For example, the WORM memory with multilevel ON states, it is now observed from 8 nm up to 14 nm and the WORM memory with NDR starting from 15 nm. In order to determine the exact thickness range, it is necessary to do more experiments. However, the results already show that small changes to some experimental parameters can lead to significant changes in the electrical behavior.

To understand the effect of the different thicknesses on the electrical properties of PMMA films, we have studied their morphology. Figure 5 shows the morphology of two PMMA films with two different thicknesses, 9 nm and 15 nm (Figures 5(a) and 5(b), resp.), which were fabricated using

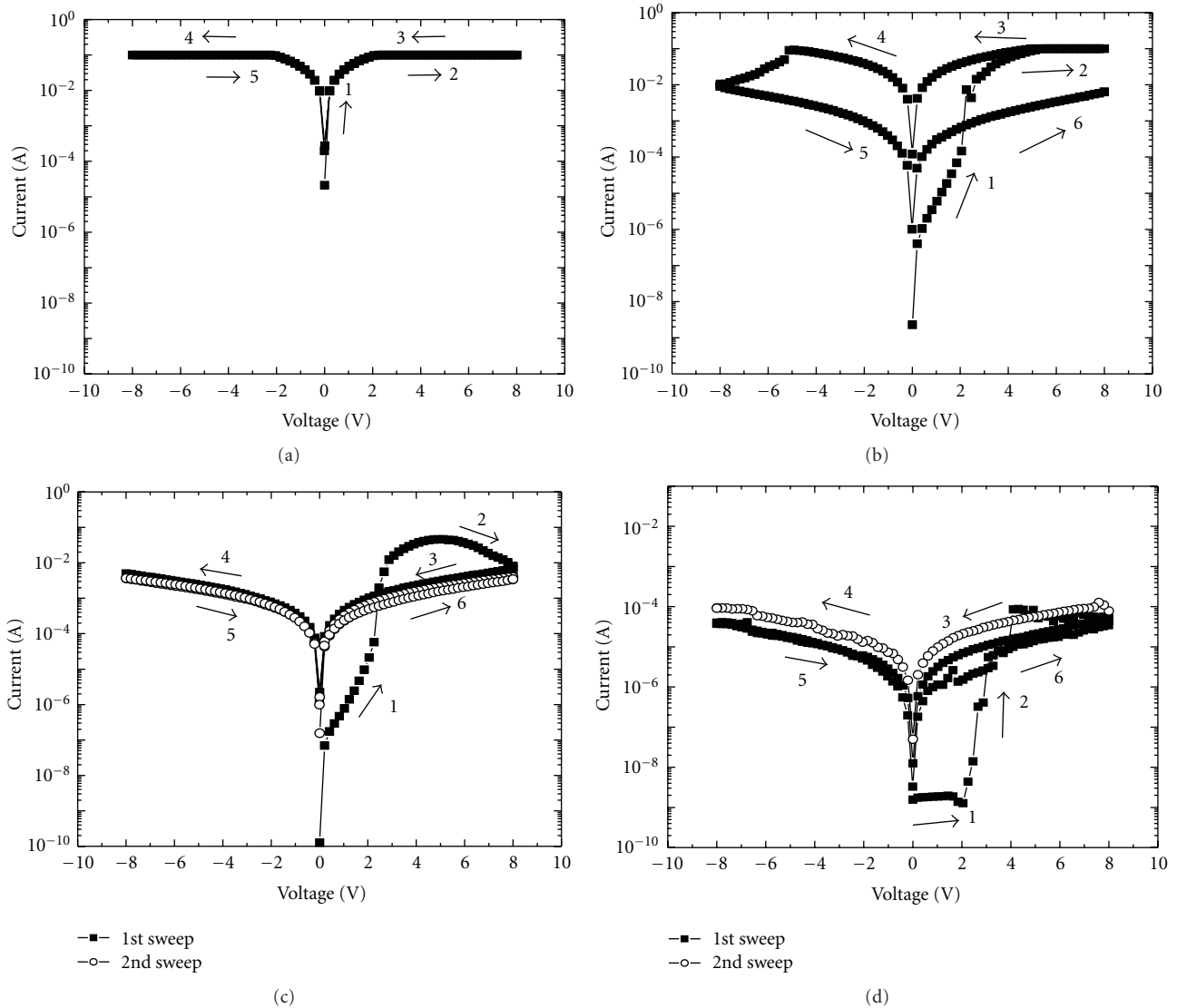


FIGURE 2: *I-V* response of the Al/PMMA/Al devices as a function of PMMA thickness: (a) 7.5 nm, (b) 17 nm, (c) 22 nm, and (d) 140 nm. The devices were fabricated using CB as solvent. It can be appreciated that the *I-V* response changes as a function of the PMMA thickness.

CB. They were studied by AFM and the film with 15 nm reveals a good deposition with a small roughness about 0.3 nm. In general, all the films processed with the different solvents show good deposition, except the films smaller than 10 nm. The latter present an ohmic behavior (Figure 5(a)) and they show holes inside the film of the same order of the film thickness. These holes are responsible for the ohmic behavior because they cause a short circuit between the electrodes. Similar AFM images were reported by Pyo and coworkers for AIDNC films in the same thickness range [30]. On the other hand, the films with thicknesses bigger than 10 nm do not show holes, therefore, they are not responsible of their WORM memory behavior. The changes in the electrical properties of the devices could be related with the introduction of metal particles into the polymeric films. These metal particles could come from the top electrode, when this is thermally evaporated, as well as from both

electrodes when the voltage is increased during the first voltage sweep. In this way, this injection of metal particles could produce metallic filaments inside the polymeric films, which would be responsible for the polymer conductivity increase. The switching from the first state ON to the second one in Figure 2(b) and the NDR in Figure 2(c) would correspond to the destruction of weakest metallic filaments due to the Joule heating, when a higher voltage is applied, which are not reformed during the subsequent voltage cycles. To elucidate if the filamentary formation is the responsible mechanism for the WORM memory behavior, we have examined the effect of the voltage on the films by SEM.

Reproducible bistable switching has been reported in devices based on PS thin films and other insulator polymers [5, 24–26]. To know if the WORM memory behavior of our devices is a consequence of the interval of used voltages, the interval was increased to study how this affects their electrical

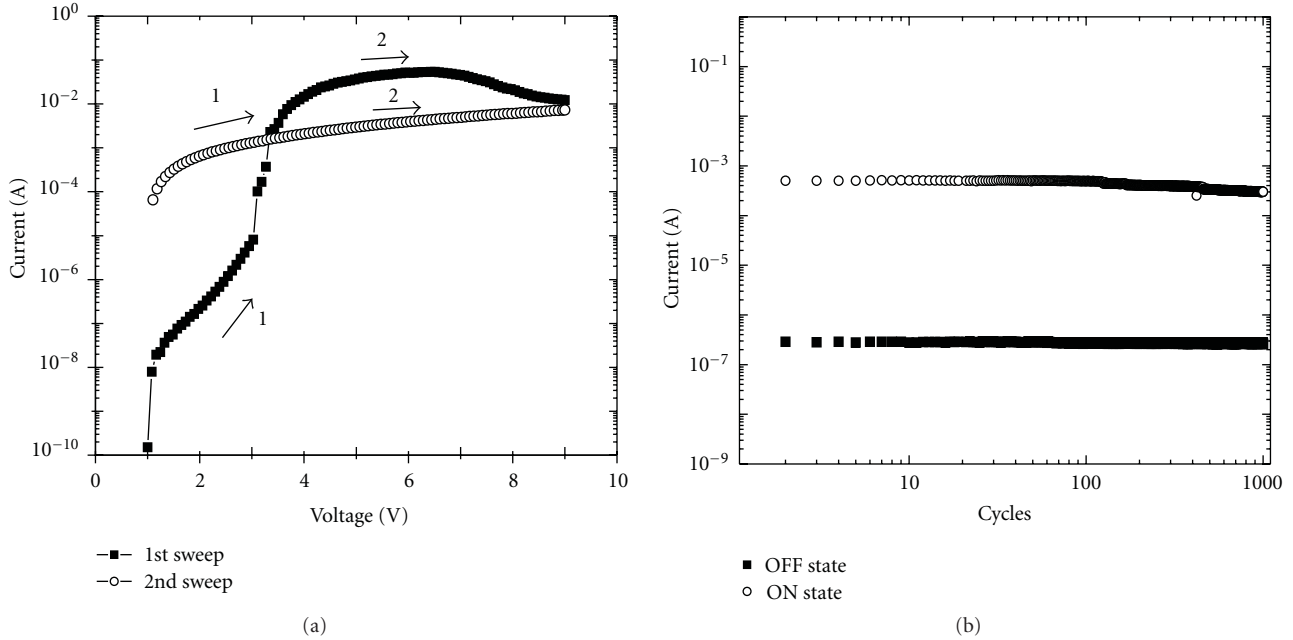


FIGURE 3: (a) I - V curve of an Al/PMMA (22 nm)/Al device. PMMA was dissolved with CB. (b) Effect of the read cycles on the stability of the On and Off states. The read voltage was set at 1 V.

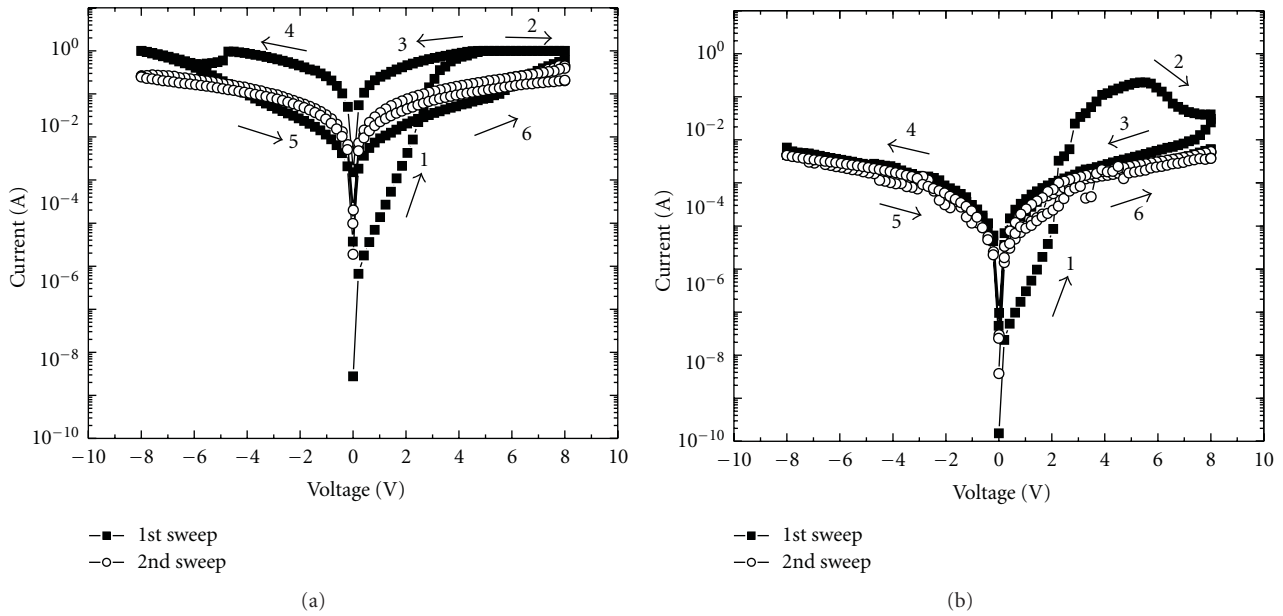


FIGURE 4: I - V response of Al/PS/Al devices. PS was dissolved with CB, for two different PS thicknesses: (a) 11 nm and (b) 18 nm. Note that the results are basically similar to those of PMMA devices in a similar thickness range.

and morphological properties. Figure 6 shows the I - V curves of Al/PMMA/Al devices with an organic thickness film of 22 nm. As it was mentioned earlier, the devices with this thickness showed a WORM memory behavior with NDR for voltage sweeps from 0 to 8, 8 to -8 , and -8 to 8 V. To study the morphological changes and damages caused by the application of voltage sweeps to the PMMA film [31], it is necessary to remove the top aluminum electrode. However,

removing the top electrode without damaging the polymer layer would be very complicated. Therefore for achieving this goal, a 10 nm polyvinyl alcohol (PVA) layer was spin coated between the top electrode and the 22 nm PMMA layer, which was removed with water after the voltage cycle application. Note that we are changing the total thickness of the device and, as a consequence, the I - V characteristics, but our goal here was to study in a qualitative way the effect

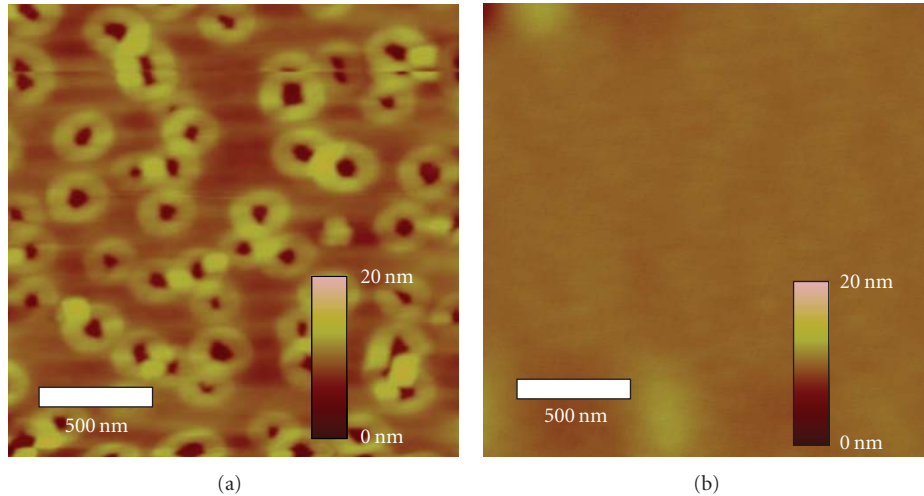


FIGURE 5: AFM images of the PMMA films over glass substrates with a thickness of (a) 9 nm, which corresponds to I - V ohmic response and (b) 15 nm, which corresponds to I - V response with two ON states.

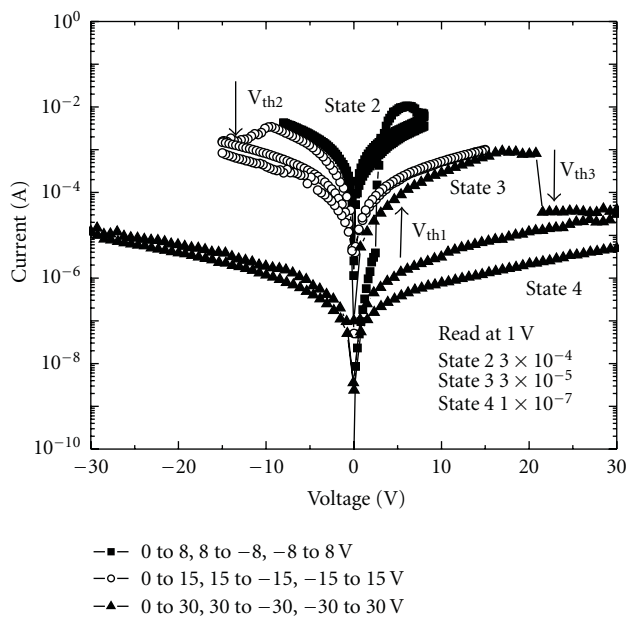


FIGURE 6: I - V response of an Al/PMMA (22 nm)/Al memory device. In addition to the threshold voltage at 2 V, threshold voltages at -12 and 20 V are observed.

of the electric field on the top electrode and PMMA film of the memory device. Furthermore, the total thickness (32 nm) of the PVA-PMMA layer is similar to films with WORM behavior (see Figure 2(d) and Table 1). The top electrode and the PMMA layer were observed by using SEM. From the Figures 7(a) and 7(b) no appreciable damages on PMMA layer and on the bottom surface of the top electrode were observed when cycles of 8 V were applied, compared with the pristine ones. From elemental mapping SEM photographs, we were unable to observe properly the aluminum particles in the films because the signal coming from the bottom

aluminum electrode interfered. However, this inconvenience was resolved using ITO as the bottom electrode, instead of Al. From the elemental mapping, we observe the injection of aluminum particles into the film, in this way filamentary formation is occurring.

When the interval of used voltages was extended, the MIM device with 22 nm of thickness showed other threshold voltages at -15 and 20 V (Figure 6), which indicate the formation of several levels of electrical conduction. These new levels of electrical conductance were obtained by using the following procedure. A voltage sweep from 0 to -15 V was applied and, at around -12 V (V_{th2}), the device conductivity switched from state 2 to state 3 (3×10^{-5} A read at 1 V). During this voltage sweep, we note that the top electrode begins to burn, possibly due to the Joule heating. We consider that this damage on the top electrode is the responsible mechanism of the decrease in the conductivity [25, 26, 32]. In the subsequent voltage scans (from -15 to 15 V and from 15 to -15 V) the device remains in the state 3, even when the supply is turned off. Finally, a voltage scan was performed from 0 to 30 V. In this sweep, the device shows another conductivity switching at around 20 V (V_{th3}) from state 3 to state 4 (1×10^{-7} A read at 1 V). The conductivity remains there for the following voltage sweep (from 30 to -30 V and from -30 to 30 V). To quantify the damages of the higher voltage cycle on the top electrode and PMMA layer, we have realized the same procedure described before in order to study, by using SEM, the physical damages on the devices as a consequence of the voltage application. For this, cycles from 0 to 20 V, from 20 to -20 V, and from -20 to 20 V were applied to a device fabricated with a PVA layer of 10 nm and PMMA layer of 22 nm. We observe that at voltage around 20 V, the PVA-PMMA device begins to burn similarly to the films without PVA. Figures 7(c) and 7(d) show the effects of the strong electric fields in the polymer and aluminum layers, respectively. From Figure 7(c), the formation of circular craters in the polymer layer can be appreciated, where material appears

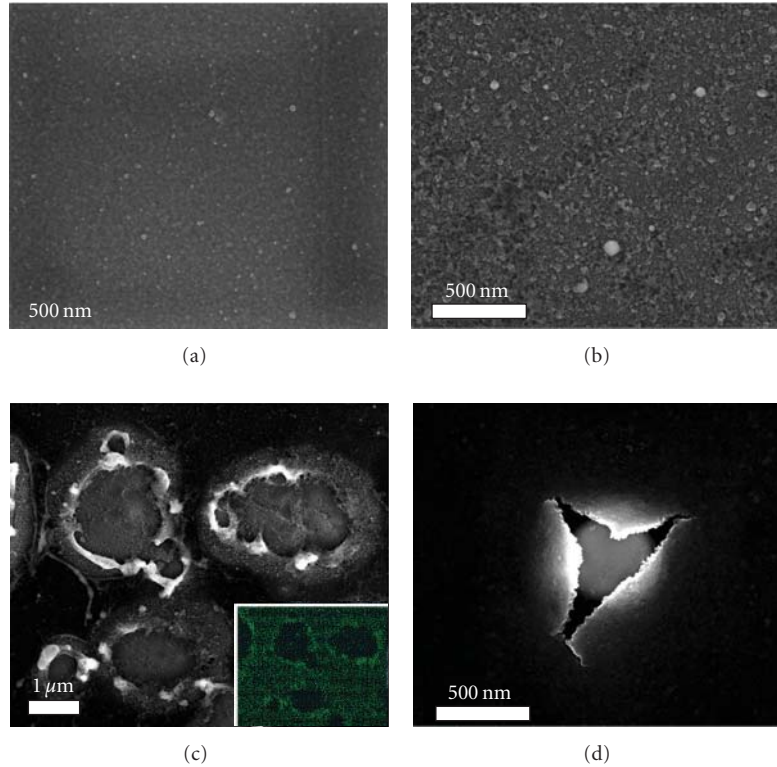


FIGURE 7: SEM images of (a) polymer layer and (b) the top aluminum electrode show no damage when cycles of 8 V were applied to the Al/PVA (10 nm)-PMMA (22 nm)/Al device. Contrary to the first case, when cycles of 20 V were applied, SEM images show physical damages in both, (c) the PMMA layer and the (d) top aluminum electrode. The inset of (c) shows the aluminum elemental mapping of the PMMA layer.

to be ejected, and, from the inset of the figure, the removal of the aluminum particles from the craters. On the other hand, Figure 7(d) shows the rupture on the bottom surface of the top aluminum layer. Therefore, these damages in the top electrode and in the PMMA film come from Joule heating as well as the intense electric fields, and they are responsible for the conductivity decrease. Thus, the existence of these ON multistates for high-voltage application is consequence of damages to the device and suggests that once the metallic filaments have been broken, it is impossible for them to be reformed. Other possible explanation could be that the rate of rupture or destruction of filaments is bigger than their formation.

Other important variable in the filamentary formation is the compliance current. In Figure 8, we compare the effect of the compliance current on the electrical properties of a 17 nm PMMA memory. First, we have electroformed the device using a compliance current of 20 mA and the voltage bias was swept from 0 to 8 V. After that, we have studied as the formation and rupture of filaments depend on the compliance current and the voltage interval. Note that all experiments were performed on the same device. When the compliance current is low, 40 mA, we observe (Figure 8(a)) that the I - V curves almost remain the same. This may occur because at low-compliance currents, possibly, there is no rupture or formation of new filaments. Another possible explanation is that the rate of formation of new filaments is

equal to the rate of their rupture. The increase of the compliance current to 60 mA (Figure 8(b)) shows similar results to those reported for 40 mA, although in the first sweep of the voltage, we observe the formation of new filaments and, possibly, the rupture of the weakest. When the compliance current was increased to 80 mA (Figure 7(c)), we observe formation of new filaments, in the first sweep of voltage, but since the second sweep, the destruction of filaments due to Joule heating is much larger than their formation. Thus, the conductivity of the MIM device decreases sharply. We performed five sweeps of voltage on the device, and we did not observe the recovery of the initial conductivity. This indicates that at high-compliance currents, once the filaments are broken due to Joule heating, these are difficult to reform or the rate of formation of filaments is much less than their rupture. In addition, we have studied the possibility of increasing the rate of formation of filaments with respect to their rupture. For this, the bias voltage was swept from 0 to 12 V, and the compliance current was decreased from 80 mA to 60 mA. Figure 7(d) shows that the conductivity increases in the first and second voltage sweeps, indicating that the rate of filament formation is higher than its rupture or destruction. This conductivity recovery can be related with a new influx of metallic particles coming from fractures of the electrodes due to the electric field and, as consequence, the formation of new filaments. In the third sweep of the voltage, the rate of broken filaments is higher

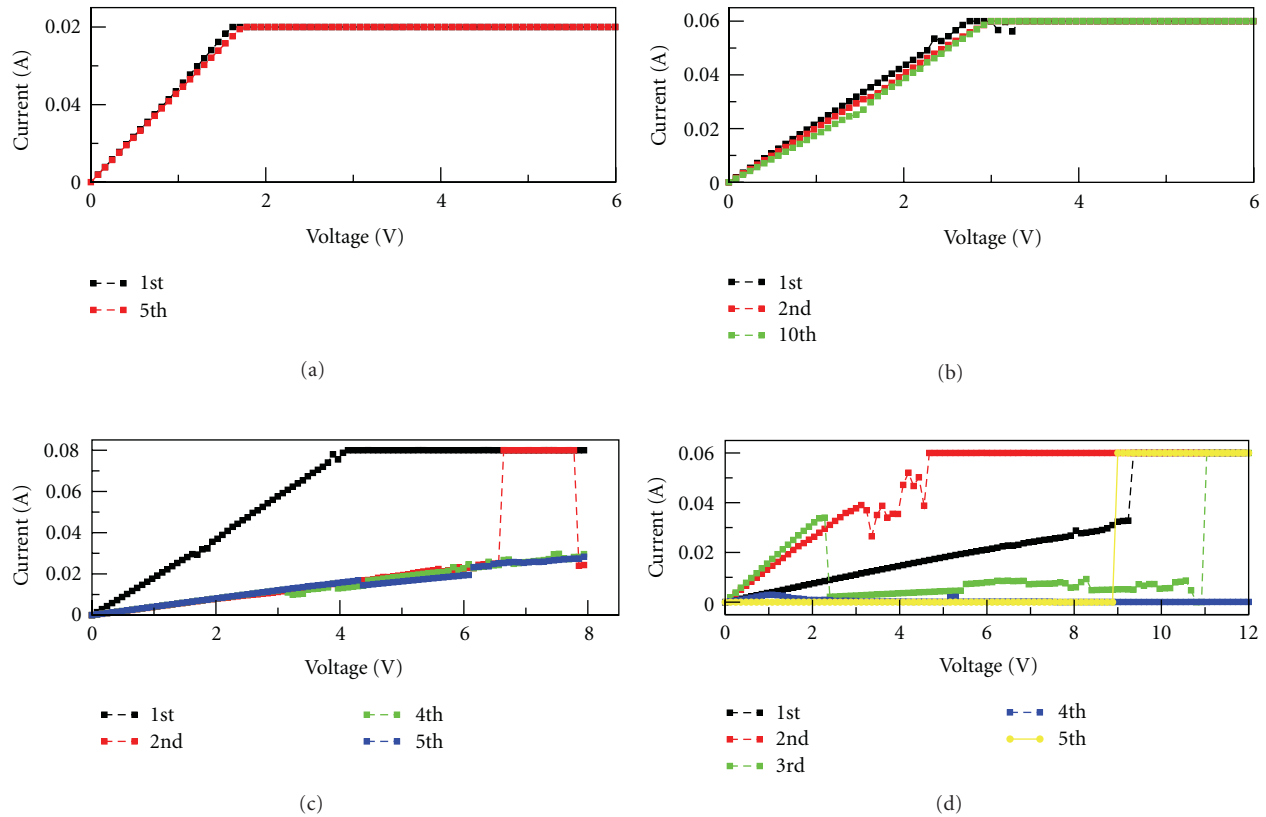


FIGURE 8: I - V behavior of a 17 nm PMMA device as a function of the compliance current. The electroforming of the device was realized using a compliance current of 20 mA, and the bias voltage was swept from 0 to 8 V. To study the effect of the compliance current on the formation and rupture of filaments, these were set at (a) 40 mA, (b) 60 mA, (c) 80 mA, and (d) 60 mA (see text). The I - V measurements were sequentially performed on the MIM device.

than their formation and, therefore, the conductivity begins to decrease. In the fourth sweep, almost all the filaments were broken and the conductivity is minimal. The filamentary formation is initiated again in the following scan of the voltage. During sweeps performed in this voltage interval, it has been observed at first glance that the top electrode begins to degrade due to the intense electric fields and Joule heatings. All these results show that the compliance currents and voltage intervals are fundamental parameters for the formation and rupture of filaments in MIM devices.

4. Conclusion

We have obtained WORM memory devices by using the simple structure aluminum/insulator polymer/aluminum. In particular, we have used PMMA as well as PS like the insulator polymer, and the films have been deposited by spin coating technique using different solvents. The I - V behavior of the devices is independent of the solvent and polymer used, but this strongly depends on the thickness of the organic layer, the compliance current, and voltage intervals used during the voltages sweeps. The MIM devices show different behaviors as a function of the film thickness: (i) films having a thickness smaller than 10 nm are in short circuit, (ii) when the film thickness is between 11 and 20 nm

the device shows a WORM behavior with two ON states, (iii) films with thicknesses between 20 and 25 nm present WORM memory with strong NDR, (iv) with thicknesses bigger than 25 nm, polymer films show WORM memory, (v) finally, organic films bigger than 300 nm have insulator behavior. The negligible dependence of the insulator polymer type used for the memory devices leads us to conclude that the influence of the organic layer is minimal and we can attribute the memory effect to the metal electrodes. We consider that small metallic particles coming from the aluminum electrodes are introduced during the evaporation of the top electrode and/or from both electrodes during the voltage application. The introduction of these particles is the responsible mechanism of the conductivity switching in the devices and of the formation of metallic filaments. Thus, the existence of some devices with two ON state or with NDR region is obtained when some weak metallic filaments are irreversible broken due to the Joule heating.

Acknowledgments

The authors acknowledge Gladis Labrada, Francisco Ramírez Jacobo, and Dr. Miguel Avalos for technical assistance as well as LINAN at IPICYT for providing access to their characterization facilities. This paper was supported at UASLP

by SEP-PROMEP through Grant no. 103.5/07/2574 and by CONACYT through Grant no. S-3148 and for scholarships (J. A. A.-Niño and A. O. Sustaita).

References

- [1] J. C. Scott and L. D. Bozano, "Nonvolatile memory elements based on organic materials," *Advanced Materials*, vol. 19, no. 11, pp. 1452–1463, 2007.
- [2] Q. D. Ling, D. J. Liaw, E. Y. H. Teo et al., "Polymer memories: bistable electrical switching and device performance," *Polymer*, vol. 48, no. 18, pp. 5182–5201, 2007.
- [3] Y. Yang, J. Y. Ouyang, L. Ma, R. J. H. Tseng, and C. W. Chu, "Electrical switching and bistability in organic/polymeric thin films and memory devices," *Advanced Functional Materials*, vol. 16, no. 8, pp. 1001–1014, 2006.
- [4] D. Tondelier, K. Lmimouni, D. Vuillaume, C. Fery, and G. Haas, "Metal/organic/metal bistable memory devices," *Applied Physics Letters*, vol. 85, no. 23, pp. 5763–5765, 2004.
- [5] M. Cölle, M. Büchel, and D. M. de Leeuw, "Switching and filamentary conduction in non-volatile organic memories," *Organic Electronics*, vol. 7, no. 5, pp. 305–312, 2006.
- [6] F. Verbakel, S. C. J. Meskers, R. A. J. Janssen et al., "Reproducible resistive switching in nonvolatile organic memories," *Applied Physics Letters*, vol. 91, no. 19, Article ID 192103, 2007.
- [7] Y. S. Lai, C. H. Tu, D. L. Kwong, and J. S. Chen, "Bistable resistance switching of poly(N-vinylcarbazole) films for non-volatile memory applications," *Applied Physics Letters*, vol. 87, no. 12, Article ID 122101, pp. 1–3, 2005.
- [8] H. S. Majumdar, A. Bolognesi, and A. J. Pal, "Memory applications of a thiophene-based conjugated polymer: capacitance measurements," *Journal of Physics D*, vol. 36, no. 2, pp. 211–215, 2003.
- [9] M. Beinhoff, L. D. Bozano, J. C. Scott, and K. R. Carter, "Design and synthesis of new polymeric materials for organic nonvolatile electrical bistable storage devices: poly(biphenylmethylene)s," *Macromolecules*, vol. 38, no. 10, pp. 4147–4156, 2005.
- [10] M. Lauters, B. McCarthy, D. Sarid, and G. E. Jabbour, "Multi-level conductance switching in polymer films," *Applied Physics Letters*, vol. 89, no. 1, Article ID 013507, 2006.
- [11] A. R. Elsharkawi and K. C. Kao, "Switching and memory phenomena in anthracene thin films," *Journal of Physics and Chemistry of Solids*, vol. 38, no. 1, pp. 95–96, 1977.
- [12] C. H. Tu, Y. S. Lai, and D. L. Kwong, "Memory effect in the current—voltage characteristic of 8-hydroquinoline aluminum salt films," *IEEE Electron Device Letters*, vol. 27, no. 5, pp. 354–356, 2006.
- [13] M. Terai, K. Fujita, and T. Tsutsui, "Electrical bistability of organic thin-film device using Ag electrode," *Japanese Journal of Applied Physics*, vol. 45, no. 4, pp. 3754–3757, 2006.
- [14] S. Baek, D. Lee, J. Kim, S. H. Hong, O. Kim, and M. Ree, "Novel digital nonvolatile memory devices based on semiconducting polymer thin films," *Advanced Functional Materials*, vol. 17, no. 15, pp. 2637–2644, 2007.
- [15] L. P. Ma, J. Liu, and Y. Yang, "Organic electrical bistable devices and rewritable memory cells," *Applied Physics Letters*, vol. 80, no. 16, pp. 2997–2999, 2002.
- [16] T. Ouisse and O. Stéphan, "Electrical bistability of polyfluorene devices," *Organic Electronics*, vol. 5, no. 5, pp. 251–256, 2004.
- [17] L. D. Bozano, B. W. Kean, V. R. Deline, J. R. Salem, and J. C. Scott, "Mechanism for bistability in organic memory elements," *Applied Physics Letters*, vol. 84, no. 4, pp. 607–609, 2004.
- [18] J. Y. Ouyang, C. W. Chu, C. R. Szmanda, L. Ma, and Y. Yang, "Programmable polymer thin film and non-volatile memory device," *Nature Materials*, vol. 3, no. 12, pp. 918–922, 2004.
- [19] C. W. Chu, J. Y. Ouyang, J. H. Tseng, and Y. Yang, "Organic donor-acceptor system exhibiting electrical bistability for use in memory devices," *Advanced Materials*, vol. 17, no. 11, pp. 1440–1443, 2005.
- [20] J. K. Baral, H. S. Majumdar, A. Laiho et al., "Organic memory using [6,6]-phenyl-C61 butyric acid methyl ester: morphology, thickness and concentration dependence studies," *Nanotechnology*, vol. 19, no. 3, Article ID 035203, 2008.
- [21] H. S. Majumdar, J. K. Baral, R. Österbacka, O. Ikkala, and H. Stubb, "Fullerene-based bistable devices and associated negative differential resistance effect," *Organic Electronics*, vol. 6, no. 4, pp. 188–192, 2005.
- [22] J. A. Ávila-Niño, E. Segura-Cárdenas, A. O. Sustaita, I. Cruz-Cruz, R. López-Sandoval, and M. Reyes-Reyes, "Nonvolatile write-once-read-many-times memory device with functionalized-nanoshells/PEDOT:PSS nanocomposites," *Materials Science and Engineering B*, vol. 176, no. 5, pp. 462–466, 2011.
- [23] G. Simmons and R. R. Verderber, "New conduction and reversible memory phenomena in thin insulating films," *Proceedings The Royal Society A*, vol. 301, no. 1464, pp. 77–102, 1967.
- [24] R. E. Thurstans and D. P. Oxley, "The electroformed metal-insulator-metal structure: a comprehensive model," *Journal of Physics D*, vol. 35, no. 8, pp. 802–809, 2002.
- [25] H. Carchano, R. Lacoste, and Y. Segui, "Bistable electrical switching in polymer thin films," *Applied Physics Letters*, vol. 19, no. 10, pp. 414–415, 1971.
- [26] Y. Segui, B. Ai, and H. Carchano, "Switching in polystyrene films: transition from on to off state," *Journal of Applied Physics*, vol. 47, no. 1, pp. 140–143, 1976.
- [27] L. F. Pender and R. J. Fleming, "Memory switching in glow discharge polymerized thin films," *Journal of Applied Physics*, vol. 46, no. 8, pp. 3426–3431, 1975.
- [28] W. J. Joo, T. L. Choi, J. Lee et al., "Metal filament growth in electrically conductive polymers for nonvolatile memory application," *Journal of Physical Chemistry B*, vol. 110, no. 47, pp. 23812–23816, 2006.
- [29] G. Dearnaley, A. M. Stoneham, and D. V. Morgan, "Electrical phenomena in amorphous oxide films," *Reports on Progress in Physics*, vol. 33, no. 3, pp. 1129–1191, 1970.
- [30] S. Pyo, L. Ma, J. He, Q. Xu, Y. Yang, and Y. Gao, "Experimental study on thickness-related electrical characteristics in organic/metal-nanocluster/organic systems," *Journal of Applied Physics*, vol. 98, no. 5, Article ID 054303, 6 pages, 2005.
- [31] D. C. Prime, *Switching mechanisms, electrical characterization and fabrication of nanoparticle based non-volatile polymer memory devices*, Ph.D. thesis, De Montfort University, Leicester, UK, 2010.
- [32] W. L. Kwan, B. Lei, Y. Shao, S. V. Prikhodko, N. Bodzin, and Y. Yang, "Direct observation of localized conduction pathways in photocross-linkable polymer memory," *Journal of Applied Physics*, vol. 105, no. 12, Article ID 124516, 2009.

Research Article

Effect of Processing Parameters on Performance of Spray-Deposited Organic Thin-Film Transistors

Jack W. Owen,¹ Natalia A. Azarova,¹ Marsha A. Loth,² Markos Paradinas,³ Mariona Coll,³ Carmen Ocal,³ John E. Anthony,² and Oana D. Jurchescu¹

¹Department of Physics, Wake Forest University, Winston-Salem, NC 27109, USA

²Department of Chemistry, University of Kentucky, Lexington, KY 40506, USA

³Institut de Ciència de Materials de Barcelona, ICMA-B-CSIC, Campus UAB, 08193-Barcelona, Spain

Correspondence should be addressed to Oana D. Jurchescu, jurcheod@wfu.edu

Received 1 February 2011; Accepted 14 March 2011

Academic Editor: Marisol Reyes-Reyes

Copyright © 2011 Jack W. Owen et al. This is an open access article distributed under the Creative Commons Attribution License, which permits unrestricted use, distribution, and reproduction in any medium, provided the original work is properly cited.

The performance of organic thin-film transistors (OTFTs) is often strongly dependent on the fabrication procedure. In this study, we fabricate OTFTs of soluble small-molecule organic semiconductors by spray-deposition and explore the effect of processing parameters on film morphology and device mobility. In particular, we report on the effect of the nature of solvent, the pressure of the carrier gas used in deposition, and the spraying distance. We investigate the surface morphology using scanning force microscopy and show that the molecules pack along the π -stacking direction, which is the preferred charge transport direction. Our results demonstrate that we can tune the field-effect mobility of spray-deposited devices two orders of magnitude, from 10^{-3} cm²/Vs to 10^{-1} cm²/Vs, by controlling fabrication parameters.

Organic semiconductors have emerged as novel materials for electronic devices which combine the advantages of low cost with high diversity and compatibility with a broad range of substrates [1, 2]. A wide variety of polymers and small-molecule organic semiconductors have been developed and investigated in devices such as organic thin-film transistors (OTFTs), organic photovoltaic cells (OPVs), and organic light-emitting diodes (OLEDs) [3, 4]. Single crystals of small-molecule organic semiconductors have demonstrated impressive properties, such as high mobility [5–8], metallic-like behavior [9], and long-range exciton diffusion [10]. Remarkable transistor properties were reported in solution-deposited soluble small molecules having strong π -stacking interactions [11–15]. Solution-processable small-molecule organic semiconductors offer attractive properties which are of interest across the spectrum of organic electronic devices from OPV, to OTFTs and OLEDs. These attributes include low-complexity synthesis and purification procedures, superior charge carrier mobilities, and better chemical stability compared to polymers. Moreover, they are monodisperse, and parameters such as polydispersity, regioregularity, and

batch-to-batch variations are not an issue, which greatly improves reproducibility. Fabrication methods based on solution deposition, such as spin-coating, drop-casting, or ink-jet printing are of particular interest as they meet the manufacturing requirements for low-cost electronics. Unfortunately, these methods are not necessarily compatible with large-area electronics, and given the strong dependence of film electrical properties on microstructure, which in turn is severely driven by processing details, it is not clear that the impressive performance derived from these materials can be reproduced over larger areas. We have recently demonstrated high-performance small-molecule organic semiconductor TFTs fabricated by spray-coating [16]. This method offers fast deposition over large areas at low cost and thus meets manufacturing requirements for large-area electronics. Our results on spray-deposited transistors have demonstrated transistor performance similar to spin-coated devices, while utilizing 20 times smaller amount of organic semiconductor than the wasteful spin-coating procedure.

In this paper, we will explore the effect of processing parameters on the performance of spray-deposited OTFTs

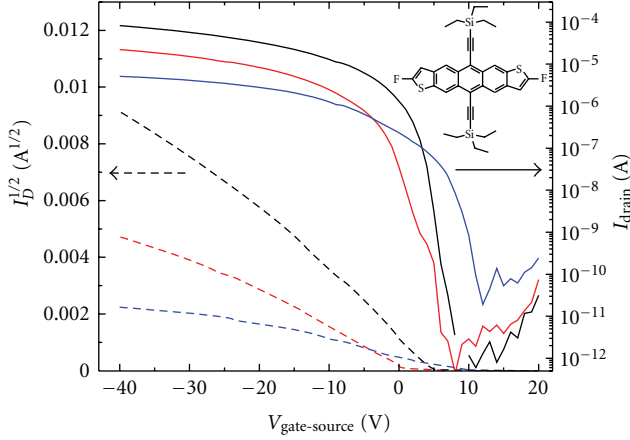


FIGURE 1: Current-voltage characteristics (drain current I_D versus gate-to-source voltage V_{GS} in saturation regime, $V_{DS} = -40$ V) for diF TES ADT devices sprayed from chlorobenzene (black), toluene (red) and dichlorobenzene (blue) solutions. The right axis corresponds to the solid lines and represents $\log(I_D)$, and the left axis corresponds to the dotted lines and shows the $\sqrt{I_D}$.

and demonstrate that the field-effect mobility can span several orders of magnitude in thin films of nominally the same material upon choice of solvent used for fabrication or variations in pressure of the carrier gas, spraying distance, and solution concentration. The dependence of device parameters on processing conditions may represent a serious issue for the reproducibility and reliability of OTFTs, and for this reason a good insight into the effect of these parameters should offer better control over device performance. By using local probe techniques, we demonstrate that the morphology of the spray-deposited devices showing the best performance is in agreement with that of spin-coated devices, and for this reason comparable performance is achieved.

In order to investigate the effect of processing parameters on device structure, we have fabricated OTFTs by spray coating a solution of 2,8-difluoro-5,11-bis(triethylsilylethynyl) anthradithiophene (diF-TESADT, chemical structure shown in the inset of Figure 1) over prefabricated device structures. These test beds consist of heavily doped Si gate electrode, 200 nm thermally grown SiO_2 , and e-beam evaporated Ti/Au (5 nm/45 nm) source and drain contacts. The substrates were cleaned with hot acetone, isopropyl alcohol, followed by UV ozone cleaning and DI water rinse. The contacts were chemically modified using PFBT (pentafluorobenzene thiol) self-assembled monolayer (SAM), which was demonstrated to improve charge injection and film morphology [3, 11]. The organic semiconductor was dissolved in a solvent, and the solution was sprayed in atmospheric conditions, by using an Iwata Kustom TH K9200 air brush, under pressurized high purity argon, held at a controlled distance above the device substrate. The air brush was held in a fixed position, aiming perpendicular to the substrate, and the spraying process took about 20 s. More details on fabrication were reported elsewhere [16]. In Figure 1, we present the electrical properties of diF-TES ADT TFTs, with the organic film being spray-coated from three different solvents: chlorobenzene

(black), toluene (red), and dichlorobenzene (blue). All electrical measurements were performed in ambient atmosphere. On the right axis, in solid lines, we show the evolution of the drain current (I_D) with the gate-to-source voltage (V_{GS}) in the saturation regime (drain-to-source voltage $V_{DS} = -40$ V). On the left axis, in dotted lines, we present the evolution of the $\sqrt{I_D}$ versus V_{GS} for the same devices. The latter plot was used to determine the field-effect mobility in the saturation regime, from the following expression:

$$I_D = \frac{1}{2} \frac{W}{L} C_i \cdot \mu \cdot (V_{GS} - V_T)^2, \quad (1)$$

where W and L are the channel width and length, respectively, C_i is the gate oxide capacitance per unit area ($C_i = 1.7 \cdot 10^{-4}$ F/m²), μ represents the field-effect mobility, and V_T is the threshold voltage. The channel geometries are $L = 20 \mu\text{m}$ and $L = 1000 \mu\text{m}$ for all three devices presented in Figure 1, and the corresponding mobilities are $\mu = 0.3$ cm²/Vs for the film deposited from a chlorobenzene solution, $\mu = 0.1$ cm²/Vs for the toluene sample, and $\mu = 0.01$ cm²/Vs for the dichlorobenzene sample. These represent typical values obtained in over 10 OTFTs for each solvent. Because the semiconductor does not incorporate solvent into its crystal packing, the differences in the value of mobility come from the fact that the three solvents present different evaporation rates, leading to different crystal formation environment, which is mirrored in the electronic properties. High-vapor-pressure solvents, such as toluene, promote faster solvent evaporation, which substantially reduces the ability of the semiconductor molecules to organize in a highly ordered fashion. On the contrary, low-vapor-pressure solvents, such as chlorobenzene, promote slower evaporation rates and thus longer crystal formation time, allowing for molecular arrangement prior to transition to the solid phase. For this reason, a lower mobility is measured in toluene (vapor pressure ~ 24 mmHg at 22°C) than in chlorobenzene (vapor pressure ~ 10 mmHg at 22°C). This figure also points out that the vapor pressure of the solvent does not always scale with mobility and is thus not sufficient to describe the differences measured in electrical properties: the film deposited from dichlorobenzene exhibited the lowest mobility ($\mu = 0.01$ cm²/Vs), in spite of the fact that this solvent has the lowest vapor pressure (~ 1.5 mmHg at 22°C). Optical inspection of the film deposited from dichlorobenzene points out that the film presents poor connectivity between the crystalline domains and the ring-like-shape “coffee stain” features. This result suggests that with spray-coating, film formation is more complex, and it is critically affected by other factors such as the surface energy of the substrate, and the wettability of the solvent. When the solvent evaporates, the solution becomes supersaturated and crystals are formed on the substrate via a nucleation and growth mechanism. This is a very dynamic and complex process, driven by the interplay between solvent/substrate, solvent/vapor, solute/substrate, and solute/solvent interactions. Figure 1 also points out that not only the mobility, but also the threshold voltage of devices is affected by the choice of solvent: OTFTs deposited from dichlorobenzene and chlorobenzene showed positive

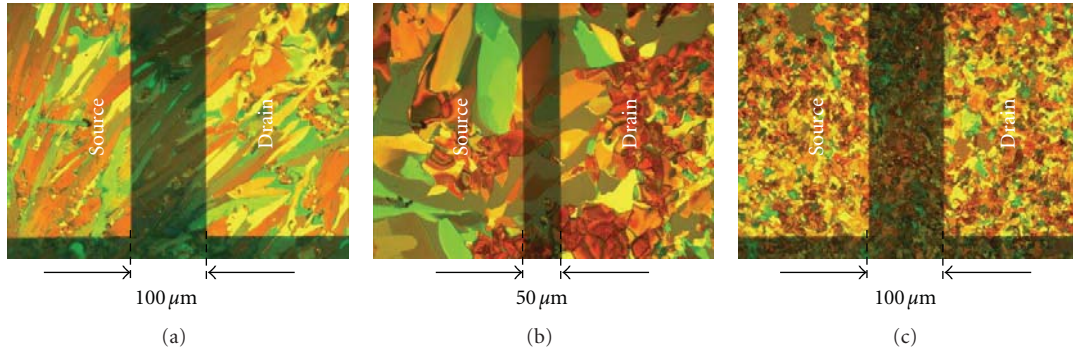


FIGURE 2: Optical micrograph of TFTs sprayed from a solution in chlorobenzene, under three argon pressures: (a) 5 psi, (b) 10 psi, and (c) 25 psi. The source and drain gold contacts are indicated.

TABLE 1: Field-effect mobility for diF TES-ADT devices spray-coated under various carrying gas pressure.

Ar pressure (psi)	5	9	10	18	25
μ (cm^2/Vs)	0.15 (± 0.05)	0.03 (± 0.007)	0.04 (± 0.008)	0.05 (± 0.02)	0.08 (± 0.02)

shifts, possibly due to the polarity of the solvent, in agreement with reports on drop-cast 5,11-bis(triethylsilylethynyl) anthradithiophene [17]. This effect is not as pronounced in the value of the on/off ratio, which is remarkably high for samples sprayed from chlorobenzene (values of 10^8 , similar to toluene transistors), but it is clearly observed in dichlorobenzene samples, where it drops to 10^5 .

Purity of organic semiconductor is known to critically affect the electronic properties. In pentacene, for example, the reduction of pentacenequinone content from 0.68% to 0.028% allowed the demonstration of mobilities as high as $35 \text{ cm}^2/\text{Vs}$ and band-like behavior [5, 6]. For this reason, we have performed the spray coating under high-purity argon, to avoid material degradation and/or the introduction of impurities during deposition. We have observed that the pressure of the carrier gas can play a determining role in the electrical properties of the devices, as it can be observed from Table 1. Here, we present the effect of the argon pressure on the device mobility for devices sprayed from a chlorobenzene solution, with the nozzle placed at distance of 13 cm from the substrate.

The mobility values reported in Table 1 are averaged over 10 devices. At low carrier gas pressures (5 psi), the TFTs present the best performance, with an average mobility of $0.15 \text{ cm}^2/\text{Vs}$. As the gas pressure is increased, the gas “blows away” the solution from the substrate, resulting in lower-quality films, which is in agreement with the lower values of mobility measured in these films. However, a small increase in mobility is observed when the pressure increases from 9 psi to 25 psi. This effect can be understood by a careful examination of the optical images presented in Figure 2. Here, devices fabricated at 5 psi (Figure 2(a)), 10 psi (Figure 2(b)), and 25 psi (Figure 2(c)) are presented. The source and drain contacts are indicated. At low pressures (Figure 2(a)),

the film covering the transistor channel consists of large crystallites spanning between the source and drain contacts, in agreement with the high mobility measured here. At higher pressures (Figure 2(b)), the continuity of the film becomes problematic: the crystallites are much smaller and they only cover a fraction of the transistor channel, yielding lower currents. When the pressure is increased even further, in spite of the fact that the grains become even smaller (Figure 2(c)), their density increases, resulting in better surface coverage and improved performance. The coverage obtained for $P = 25$ psi is similar to that resulting from 5 psi, but the mobility mitigates by a factor of two. We believe that this is a result of smaller crystalline domains present in this sample and the increased density of grain boundaries connecting them. This is in agreement with earlier reports that demonstrated significant voltage drops at the grain boundaries present in transistor channels [18] and one order of magnitude larger resistance across the grain boundaries than within the grains measured using conducting probe atomic force microscopy [19]. The films obtained by spray-coating consist of high-mobility regions within crystalline grains and low-mobility regions connecting them, and the field-effect mobility of OTFTs is a weighted sum of the two. The measured mobility is thus a function of the intrinsic mobility of the organic semiconductors (intragrain mobility) as well as the concentration of the grain boundaries (intergrain mobility). Larger grain size is usually beneficial for charge transport, as demonstrated by Lee et al. in 5,11-bis(triethylsilylethynyl) anthradithiophene TFTs [20], and this phenomenon can also be observed by comparing the devices deposited at 5 psi and 25 psi, for which the coverage is similar but the grain size is different.

To obtain a better picture of the morphology of the sprayed films, we have performed scanning force microscopy (SFM) and explored structural details such as crystalline quality, film lateral continuity, and the presence of point and extended defects. All SFM measurements were carried out under N_2 atmosphere ($\text{RH} < 2\%$) to diminish any possible humidity effects. Figure 3 shows SFM images (dynamic mode) carried out on a device spray coated from a 1.1 mg/mL solution in chlorobenzene, at 5 psi argon, from 13 cm, in a region within the organic film between metallic electrodes

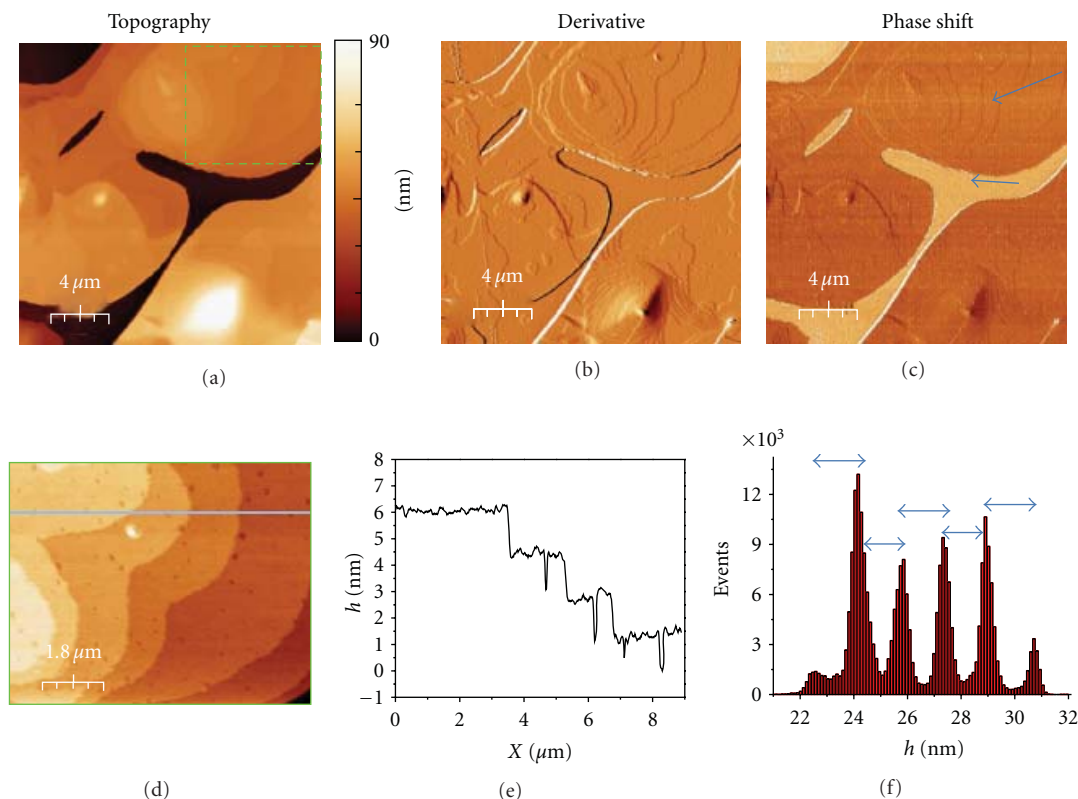


FIGURE 3: SEM data of a spray-deposited diF-TES ADT, partially covering the interelectrode device region. (a) Topographic image, (b) topography derivative image, (c) phase shift image, (d) magnification topography taken on the dotted area in (a). (e) Line profile taken along the blue segment in (d) crossing three single steps and some one-layer-deep vacancy defects. (f) Height histogram of image (d).

(transistor channel). Regions of well-developed terraces separated by steps (a–d) indicate the formation of a crystalline organic film. The derivative image in (b) highlights the presence of typical defects (e.g., screw dislocations, vacancy islands) and the pancake morphology of some grains, with up to about 7 different levels in this case. Figure 3(c) shows the phase shift image that will be described in detail later. The image in Figure 3(d) is a zoom into the film region within the dotted green lines in Figure 3(a). The profile (e) taken along the blue segment in the topographic image (d), as well as the height histogram (f) of the whole image, shows a mean step height of $h \approx 1.65$ nm, in agreement with the interlayer separation of single crystals and spin-coated diF-TES ADT crystalline films. Thus, we conclude that the growth mode of spray-deposited diF-TES ADT is similar to that of analogous spin-cast films on PFBT-treated substrates, which show a (001) molecular orientation [3, 21], with the ADT backbone of the molecules cofacially packed. This molecular arrangement is the most favorable for charge transport, as predicted by the theoretical calculations of Brédas et al. [22], and it is similar to the single-crystal structure, in which mobilities as high as $6 \text{ cm}^2/\text{Vs}$ were reported [23, 24]. This observation is important in its ability to explain the similar mobilities obtained in spray-coated and spin-coated devices, as a result of the same molecular packing. With diF-TES ADT, a mobility in the order of $10^{-3} \text{ cm}^2/\text{Vs}$ is measured when the molecules adopt

a mixed orientation in the film, and mobilities as high as $0.2\text{--}0.5 \text{ cm}^2/\text{Vs}$ can be achieved upon surface treatment that induces a (001) molecular orientation [11]. In spite of the fact that the film formation for the sprayed and spin-coated samples is very different, with significantly shorter time allowing for solvent evaporation in the spin-coating process, the interactions at the surfaces dominate the film-forming environment, and highly ordered cofacially packed molecules are present in both type of films. The clear two level contrast observed and indicated by blue arrows in the corresponding phase shift image (Figure 3(c)) is directly correlated to the highest topographic difference (≈ 30 nm) in (a). This excitation frequency contrast is known to come from a difference in total tip-sample interaction at different locations and is a consequence of different local surface properties, for instance due to the presence of different materials, chemical terminations, wetting properties, electrostatic interactions, and so forth. No phase contrast exists between the single-layer terraces of the grains, as otherwise expected from a unique crystallographic termination of the organic film, and the larger phase shift value (i.e., a more dissipative response) at the lower topographic level is most probably due to noncovered substrate regions. In order to elucidate if the differences observed in the phase shift image are due to film discontinuity and verify if these inhomogeneities reach the underlying substrate, the same surface area (containing the two regions of interest)

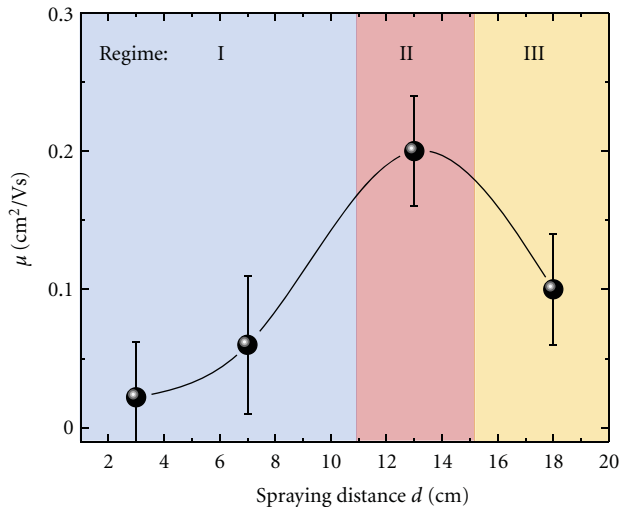


FIGURE 4: Measured field-effect mobility (μ) as a function of the spraying distance (d). Three distinct regimes can be identified.

was analyzed using a combination of dynamic operation (phase shift) and contact-mode friction force microscopy, FFM [25] (see Supporting information). A clear contrast between the two regions was observed in the dissipation-response channels (phase shift and lateral force images). The calculated friction supports the larger dissipation measured on the lower surface level with no differences among the film terrace levels, thus confirming the different tribological behavior of the two regions as corresponding to two different material properties. Moreover, the lower surface level has a root mean squared roughness of about 0.4 nm, as expected from uncovered SiO₂ substrate regions.

In this section we were interested in the effect that the spraying distance has on the performance of the devices. Figure 4 presents the evolution of field-effect mobility with the distance between the substrate and the spray nozzle, d , when the gas pressure was held constant, $p = 5$ psi. This plot indicates three distinct regimes. For short distances (regime I, $0 \text{ cm} < d < 11 \text{ cm}$), the air brush is too close to the substrate and it has an effect similar to high gas pressure: the solution on the substrate is partially blown away by the incoming flow. This effect becomes less pronounced, and the mobility improves as the distance is increased, reaching the best values for $11 \text{ cm} < d < 15 \text{ cm}$ (regime II). With further increase of the spraying distance (regime III, $d > 15 \text{ cm}$), the mobility drops to lower values, possibly due to lower film crystallinity as a result of the fact that the solvent evaporates before the small aerosolized solution droplets reach the substrate. We expect that the boundaries between the three regimes will shift when a different carrier pressure gas is used, with larger distances being optimal at higher pressures, to minimize the solution removal by the incoming flow.

In summary, we have demonstrated that the nature of solvent, pressure of the carrying gas, and the distance between the substrate and the air brush dramatically affect film forming properties in spray-deposited organic thin-film transistors and that this is reflected in significant variations

in device performance, with field-effect mobility varying two orders of magnitude upon using different processing parameters. Our best spray-coated OTFTs have mobility of $0.3 \text{ cm}^2/\text{Vs}$ and on/off ratio of 10^8 .

Acknowledgment

The authors thank Dr. David Gundlach from the National Institute of Standards and Technology for supplying the substrates coated with SiO₂ and Au.

References

- [1] T. Sekitani, U. Zschieschang, H. Klauk, and T. Someya, "Flexible organic transistors and circuits with extreme bending stability," *Nature Materials*, vol. 9, no. 12, pp. 1015–1022, 2010.
- [2] J. E. Anthony, "The larger acenes: versatile organic semiconductors," *Angewandte Chemie - International Edition*, vol. 47, no. 3, pp. 452–483, 2008.
- [3] D. J. Gundlach, J. E. Royer, S. K. Park et al., "Contact-induced crystallinity for high-performance soluble acene-based transistors and circuits," *Nature Materials*, vol. 7, no. 3, pp. 216–221, 2008.
- [4] G. Dennler, M. C. Scharber, and C. J. Brabec, "Polymer-fullerene bulk-heterojunction solar cells," *Advanced Materials*, vol. 21, no. 13, pp. 1323–1338, 2009.
- [5] O. D. Jurchescu, J. Baas, and T. T. M. Palstra, "Effect of impurities on the mobility of single crystal pentacene," *Applied Physics Letters*, vol. 84, no. 16, pp. 3061–3063, 2004.
- [6] O. D. Jurchescu, M. Popinciuc, B. J. Van Wees, and T. T. M. Palstra, "Interface-controlled, high-mobility organic transistors," *Advanced Materials*, vol. 19, no. 5, pp. 688–692, 2007.
- [7] M. E. Gershenson, V. Podzorov, and A. F. Morpurgo, "Colloquium: electronic transport in single-crystal organic transistors," *Reviews of Modern Physics*, vol. 78, no. 3, pp. 973–989, 2006.
- [8] J. Takeya, J. Kato, K. Hara et al., "In-crystal and surface charge transport of electric-field-induced carriers in organic single-crystal semiconductors," *Physical Review Letters*, vol. 98, no. 19, Article ID 196804, 2007.
- [9] I. N. Hulea, S. Fratini, H. Xie et al., "Tunable Fröhlich polarons in organic single-crystal transistors," *Nature Materials*, vol. 5, no. 12, pp. 982–986, 2006.
- [10] H. Najafov, B. Lee, Q. Zhou, L. C. Feldman, and V. Podzorov, "Observation of long-range exciton diffusion in highly ordered organic semiconductors," *Nature Materials*, vol. 9, no. 11, pp. 938–943, 2010.
- [11] O. D. Jurchescu, B. H. Hamadani, H. D. Xiong et al., "Correlation between microstructure, electronic properties and flicker noise in organic thin film transistors," *Applied Physics Letters*, vol. 92, no. 13, Article ID 132103, 2008.
- [12] S. K. Park, J. E. Anthony, and T. N. Jackson, "Solution-processed TIPS-pentacene organic thin-film-transistor circuits," *IEEE Electron Device Letters*, vol. 28, no. 10, pp. 877–879, 2007.
- [13] S. K. Park, T. N. Jackson, J. E. Anthony, and D. A. Mourey, "High mobility solution processed 6,13-bis(triisopropylsilyl)ethynyl pentacene organic thin film transistors," *Applied Physics Letters*, vol. 91, no. 6, Article ID 063514, 2007.
- [14] S. K. Park, D. A. Mourey, S. Subramanian, J. E. Anthony, and T. N. Jackson, "High-mobility spin-cast organic thin film transistors," *Applied Physics Letters*, vol. 93, no. 4, Article ID 043301, 2008.

- [15] T. Uemura, Y. Hirose, M. Uno, K. Takimiya, and J. Takeya, "Very high mobility in solution-processed organic thin-film transistors of highly ordered [1]benzothieno[3,2-b]benzothiophene derivatives," *Applied Physics Express*, vol. 2, no. 11, Article ID 111501, 2009.
- [16] N. A. Azarova, J. W. Owen, C. A. McLellan et al., "Fabrication of organic thin-film transistors by spray-deposition for low-cost, large-area electronics," *Organic Electronics: Physics, Materials, Applications*, vol. 11, no. 12, pp. 1960–1965, 2010.
- [17] C. S. Kim, S. Lee, E. D. Gomez, J. E. Anthony, and Y. L. Loo, "Solvent-dependent electrical characteristics and stability of organic thin-film transistors with drop cast bis(triisopropylsilyl)ethynyl pentacene," *Applied Physics Letters*, vol. 93, no. 10, Article ID 103302, 2008.
- [18] L. C. Teague, B. H. Hamadani, O. D. Jurchescu et al., "Surface potential imaging of solution processable acene-based thin film transistors," *Advanced Materials*, vol. 20, no. 23, pp. 4513–4516, 2008.
- [19] T. W. Kelley and C. D. Frisbie, "Gate voltage dependent resistance of a single organic semiconductor grain boundary," *Journal of Physical Chemistry B*, vol. 105, no. 20, pp. 4538–4540, 2001.
- [20] S. S. Lee, C. S. Kim, E. D. Gomez et al., "Controlling nucleation and crystallization in solution-processed organic semiconductors for thin-film transistors," *Advanced Materials*, vol. 21, no. 35, pp. 3605–3609, 2009.
- [21] R. J. Kline, S. D. Hudson, X. Zhang et al., "Controlling the microstructure of solution-processable small molecules in thin-film transistors through substrate chemistry," *Chemistry of Materials*, vol. 23, no. 5, pp. 1194–1203, 2011.
- [22] J. L. Brédas, D. Beljonne, V. Coropceanu, and J. Cornil, "Charge-transfer and energy-transfer processes in π -conjugated oligomers and polymers: a molecular picture," *Chemical Reviews*, vol. 104, no. 11, pp. 4971–5003, 2004.
- [23] O. D. Jurchescu, S. Subramanian, R. J. Kline et al., "Organic single-crystal field-effect transistors of a soluble anthradithiophene," *Chemistry of Materials*, vol. 20, no. 21, pp. 6733–6737, 2008.
- [24] O. D. Jurchescu, D. A. Mourey, S. Subramanian et al., "Effects of polymorphism on charge transport in organic semiconductors," *Physical Review B - Condensed Matter and Materials Physics*, vol. 80, no. 8, Article ID 085201, 2009.
- [25] C. Munuera, E. Barrena, and C. Ocal, "Chain-length dependence of metastable striped structures of alkanethiols on Au(111)," *Langmuir*, vol. 21, no. 18, pp. 8270–8277, 2005.

Research Article

Inkjet-Printed Organic Field-Effect Transistor by Using Composite Semiconductor Material of Carbon Nanoparticles and Poly(3-Hexylthiophene)

Chih-Ting Lin,^{1,2} Chun-Hao Hsu,¹ Chang-Hung Lee,¹ and Wen-Jung Wu³

¹Graduate Institute of Electronics Engineering, National Taiwan University, Taipei 10617, Taiwan

²Department of Electrical Engineering, National Taiwan University, Taipei 10617, Taiwan

³Department of Engineering Science and Ocean Engineering, National Taiwan University, Taipei 10617, Taiwan

Correspondence should be addressed to Chih-Ting Lin, timlin@cc.ee.ntu.edu.tw and Wen-Jung Wu, wjwu@ntu.edu.tw

Received 26 February 2011; Revised 28 April 2011; Accepted 20 May 2011

Academic Editor: Werner Blau

Copyright © 2011 Chih-Ting Lin et al. This is an open access article distributed under the Creative Commons Attribution License, which permits unrestricted use, distribution, and reproduction in any medium, provided the original work is properly cited.

Poly(3-hexylthiophene), P3HT, has been widely used in organic electronics as a semiconductor material. It suffers from the low carrier mobility characteristics. This limits P3HT to be employed in applications. Therefore, the blending semiconductor material, carbon nanoparticle (CNP), and P3HT, are developed and examined by inkjet-printing organic field-effect transistor technology in this work. The effective carrier mobility of fabricated OFETs can be enhanced by 8 folds with adding CNP and using O₂ plasma treatment. At the same time, the transconductance of fabricated OFETs is also raised by 5 folds. Based on the observations of SEM, XRD, and FTIR, these improvements are contributed to the local field induced by the formation of CNP/P3HT complexes. This observation presents an insight of the development in organic semiconductor materials. Moreover, this work also offers a low-cost and effective semiconductor material for inkjet-printing technology in the development of organic electronics.

1. Introduction

Organic electronics have received tremendous interests due to their potential applications in flexible electronics. Moreover, characteristics of organic electronics including low-cost and low-temperature process also promote the value of this research field. Therefore, various organic electronic devices have been proposed and implemented, such as organic thin film transistors (OTFTs) [1], large-area displays [2], solar cells [3–5], organic light-emitting diodes (OLEDs) [6, 7], radio frequency identification tags (RFIDs) [8], and sensors [9]. Among various fabrication methods to implement these organic electronics, printing technology is emphasized because of its compatibility to large-area fabrications and industrial mass productions. The printing techniques can be achieved by spin coating, roll-to-roll printing, screen printing, gravure printing, and inkjet printing. In these established printing techniques, inkjet-printing is one of the most intriguing techniques. Without any prepatterned process, it can directly deposit

ink materials following a designed pattern on substrates in an in-situ manner [10]. Compared with other solution-based printing processes, inkjet printing can reduce the ink material consumption by drop-on-demand design. It also overcomes the traditional contact and pattern-transferring problems. In addition, the high-resolution inkjet-printing techniques have been demonstrated up to 1 μm or less [11, 12]. As a consequence, organic materials with nanowires, nanoparticles, and nanocrystal-polymer composites have been successfully used to implement organic electronics devices by inkjet-printing process [13–16].

On the other hand, the major obstacle of organic electronics, such as OFET, to be overcome is electrical characteristics. For example, the characteristics to be improved are transistor on-off ratio, threshold voltage, and transistor transconductance. To address these, previous research works have been proposed and demonstrated. For instance, self-organized layer [17] or self-assembly monolayer (SAM) [18–20] have been employed to enhance mobility; the surface modification of electrodes [13] has been used to reduce

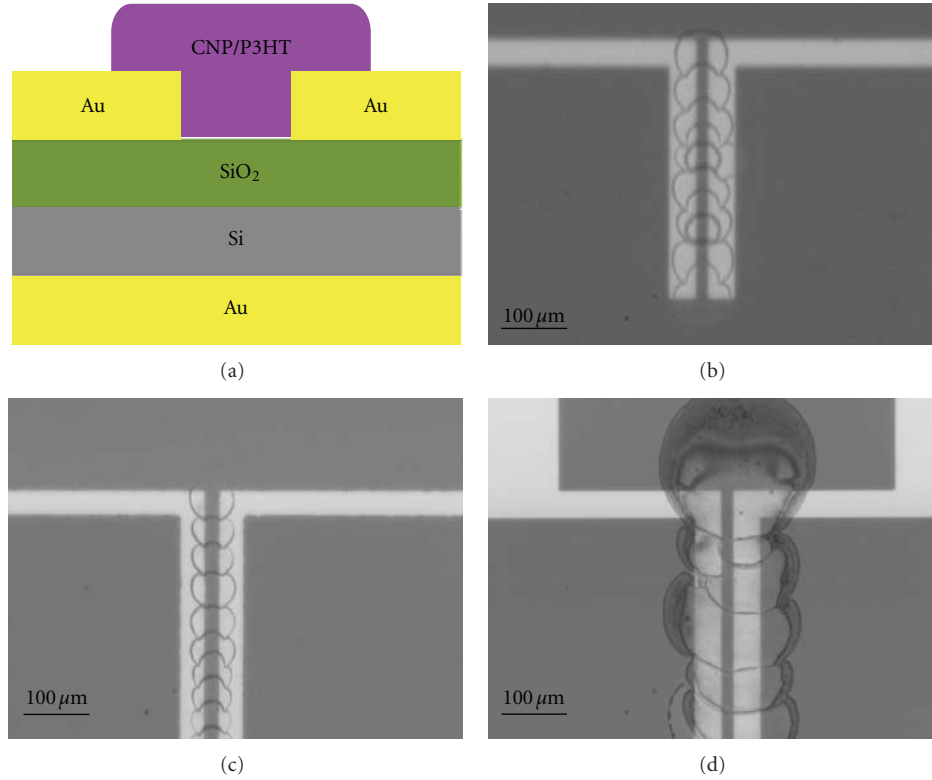


FIGURE 1: (a) Schematic representation of cross section of the inkjet-printed OFETs, (b), (c), and (d) microscope images of the OFETs for pristine P3HT, CNP/P3HT = 0.1 wt.%, and CNP/P3HT = 10 wt.%, respectively.

contact resistance; and blending organic materials [10] has been utilized to increase stability. Among various methods to improve the electrical characteristics of OFET, the composite of organic semiconductor and carbon nanostructure is attractive because of high compatibilities between these materials. For instance, carbon nanotubes were added into organic semiconductors to form composites serving as conducting bridge between organic semiconductors [21–24]. This can be used to improve the field-effect mobility. Because of CNT precipitation, however, the previously proposed methods of carbon nanotubes cannot be implemented with inkjet-printing technologies. As a result, it is necessary to develop a method compatible with inkjet printing to harness printing advantages.

In this work, poly(3-hexylthiophene) (P3HT) incorporated with carbon nanoparticles (CNPs) is used as the organic semiconductor material. The suspension capability of CNPs gives the feasibility to be implemented with inkjet-printing technologies. Utilizing this developed inkjet-printed CNP/P3HT blending semiconductor material, the mobility and transistor transconductance can be experimentally improved for 10 folds.

2. Experiments

The p-type silicon wafer with 200 nm thermal oxide is used as the substrate in this work. To form the source/drain electrodes, 20 nm Cr and 200 nm Au are deposited on the top

of the thermal oxide by evaporation. In addition, the oxide on the back side of the wafer is etched by BHF to expose the p-type silicon substrate. And gate contact is formed by deposition of 20 nm Cr and 200 nm Au after BHF etching. On the other hand, the CNP/P3HT semiconductor blending material is made at various concentrations (0, 0.1, 1, and 10 wt.% with respect to P3HT). In specific, CNPs (Qf-Nano Tech. Co. Ltd., Taiwan, model: GF-PHG-1P) with different weights are added to the P3HT (Sigma Aldrich) solution to form the blending material in different concentration. At the same time, the P3HT solution is 0.3 wt.% P3HT dissolved in p-xylene. It should be noted that the CNP/P3HT blending solutions are prepared in nitrogen glove box ($\text{H}_2\text{O} < 1$ ppm and $\text{O}_2 < 1$ ppm) and stirred on the hotplate at 90°C for 1 hour.

Before depositing the CNP/P3HT semiconductor-composite material with different concentration, the substrate with fabricated electrodes are treated by O₂ plasma (Harrick plasma, PDC-001, 10.2W) for 2 min. Then CNP/P3HT can be inkjet printed on the top of electrodes to form the OFET structure under atmosphere conditions with relative humidity (RH) maintained at 20%. After printing process, the printed CNP/P3HT semiconductor layer is cured at 70°C for 1 hour and annealed at 150°C for 10 min in nitrogen oven. In the last step to finish the device fabrication, the epoxy (Hisin Han Co. Ltd) is coated on the devices to serve as a protective layer. This protective layer is cured at 130°C for 30 min in a vacuum oven. The schematic and picture

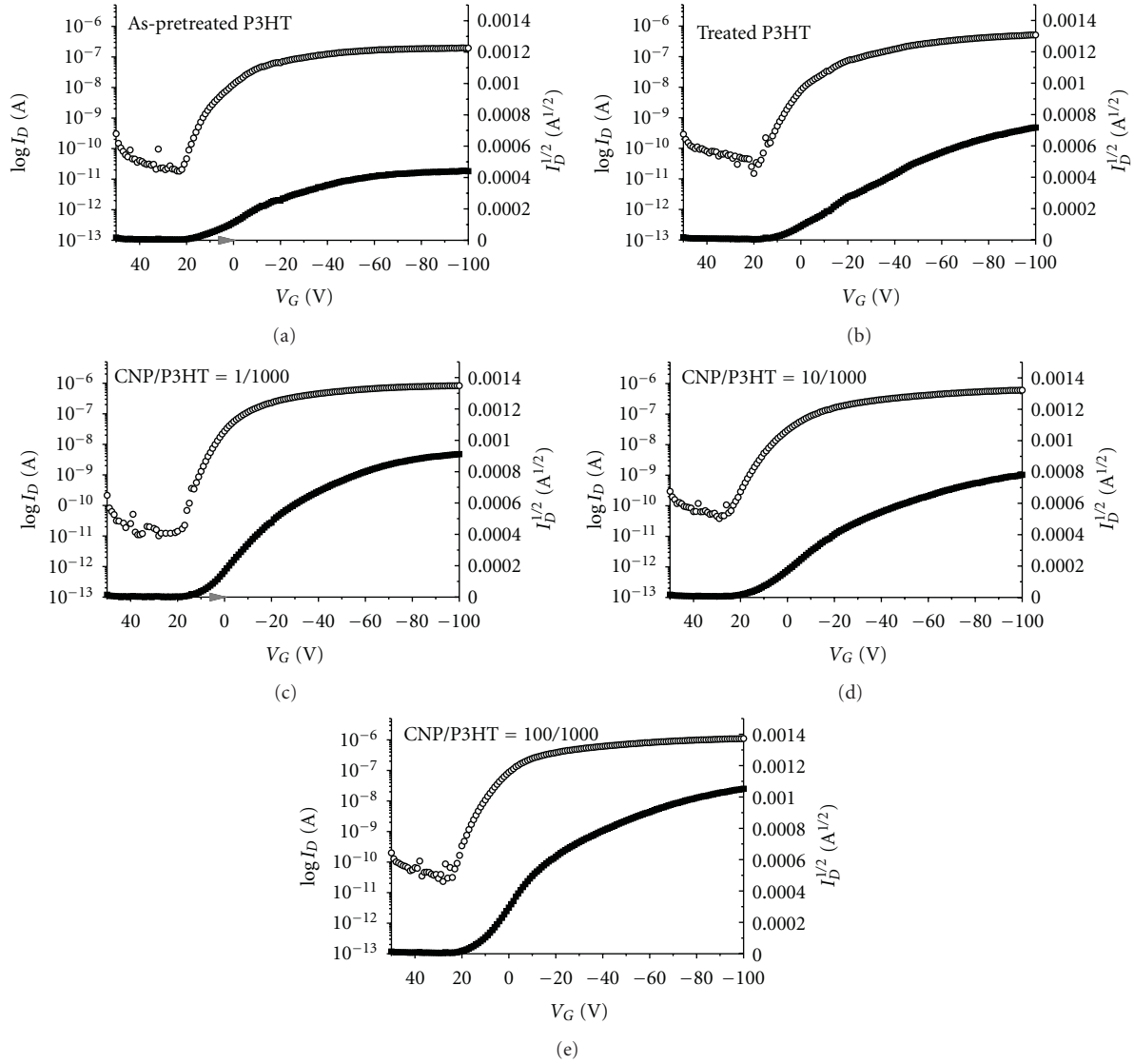


FIGURE 2: The I_D - V_{GS} of fabricated OFETs. (a) Pristine P3HT without O_2 plasma treatment; (b) pristine P3HT with O_2 plasma treatment; (c) CNP/P3HT = 0.1 wt.% with O_2 plasma treatment; (d) CNP/P3HT = 1 wt.% with O_2 plasma treatment; (e) CNP/P3HT = 10 wt.% with O_2 plasma treatment.

of fabricated inkjet-printing device are shown in Figure 1. In specific, the channel length and channel width of the fabricated OFETs are $40\ \mu\text{m}$ and $800\ \mu\text{m}$, respectively.

To evaluate the performance of the fabricated OFETs, the electrical characteristics of the OFETs are measured by using Agilent 4156C semiconductor parameter analyzer under dark-atmosphere conditions with $RH < 25\%$. Moreover, XRD (PANalytical, X' Pert PRO) and FTIR (Thermo Nicolet, Nexus470) are also performed to analyze CNP/P3HT composite material property.

3. Results and Discussions

To clearly demonstrate the transistor performance in different CNP/P3HT concentration, the I_D - V_{GS} characteristic of each OFET can be shown as Figure 2. Based on Figures 2(a)

and 2(b), the drain current of O_2 plasma-treated pristine P3HT OFET is larger than that without plasma treatment by 2 folds. From Figures 2(c), 2(d), and 2(e), in addition, this experimental result shows that the on-off ratio of different OFET keeps above 10^4 even with different concentration of CNPs. To determine the on-off ratio, the maximum drain current in I_D - V_{GS} is defined as the on current. On the contrary, the minimum drain current in I_D - V_{GS} is defined as the off current. Moreover, Figure 3 illustrates I_D - V_{DS} of each OFET to have the direct comparison. As the result obtained from Figure 2 shows, for the following CNP/P3HT OFET experiments, the devices are treated by O_2 plasma before the printing of CNP/P3HT blending semiconductors. For CNP/P3HT = 0 wt.%, 0.1 wt.%, 1 wt.%, and 10 wt.%, shown in Figure 3, the on-off ratio are 3.4×10^4 , 8.2×10^4 , 1.6×10^4 , and 4.8×10^4 , respectively. In addition, the

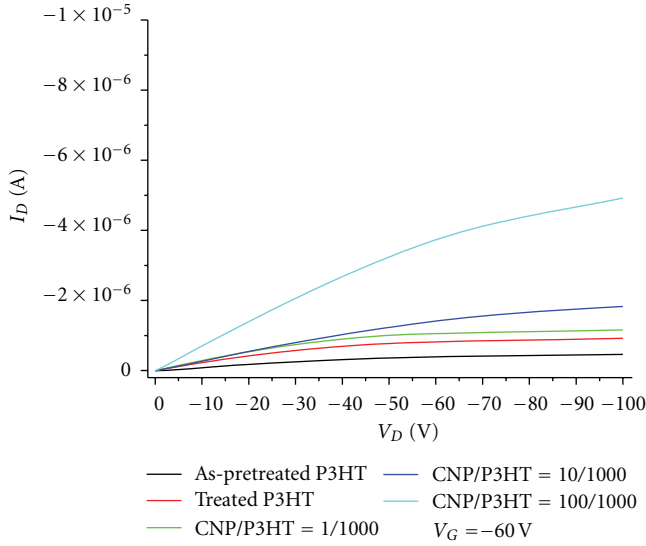


FIGURE 3: Output characteristics I_D - V_{DS} at $V_{GS} = -60V$ for various CNP/P3HT concentrations.

threshold voltage, V_{th} , can also be extracted from $I_D^{1/2}$ - V_{GS} as the device is biased in the linear region. It is identified as the extrapolation of the fitting line intercepts with zero drain current. Following this method, the threshold voltages are 8, 9.5, 13, and 15 V, respectively. Finally, the average field-effect mobility was determined in the saturation region ($V_{DS} = -100V$). Utilizing the V_{th} extracted above and the saturation current equation, the average mobility can be calculated. The calculated mobility of each OFET is 0.0014, 0.0016, 0.0017, and 0.0060 cm^2/Vs , respectively. These results can be further summarized in Table 1.

From Table 1, we can find the fact that the threshold voltage of pristine P3HT OFET is shifted to negative V_{GS} direction after O_2 plasma treatment. In addition, the increase of drain current after O_2 plasma treatment can be also found in both Figures 2 and 3. This threshold voltage shifting and current increase might be resulted from the elimination of space charges existing on the gold electrode surface by O_2 plasma [25]. This charge elimination is because of the bombardment to form a thin film of AuO_x (Au-O band formation). This oxygen chemisorptions at the surface of Au increase the work function because of the electron transfer from gold to chemisorbed oxygen. As a consequence, the space charge can be reduced [26]. These space charges limit the current flowing through the interface. Therefore, O_2 plasma can reduce the contact resistance by removing the space charges. At the same time, O_2 plasma can also clean the electrode surface by removing carbohydrates, the barrier of current flows. Moreover, the surface potential of electrodes is also modified by O_2 plasma. This promotes the adhesion of P3HT molecules and enhances the crystalline structure of CNP/P3HT thin film [27]. Both of these effects can improve the carrier diffusion length, decrease the resistance at gold/P3HT interface, and increase the drain current of OFETs. On the other hand, O_2 plasma also charges the surface of the oxide. This induces oxygen vacancy defect and

residual positive charge in the oxide [28]. This positive charge forms an opposite potential respect to the gate potential. As a consequence, the threshold voltage of OFETs is shifted to negative V_{GS} direction after O_2 plasma treatment.

For the effect of adding CNP in P3HT, from Table 1, the threshold voltage is shifted from 8 V to 15 V and the mobility is enhanced 5 folds, that is, from 0.0014 to 0.0060 cm^2/Vs , as increasing CNP concentration. This shift in threshold voltage is contributed to the formation of CNP/P3HT complexes. Since CNPs have much better conductance than P3HT, there is a local-induced field near CNPs as an external electrical field is applied. This localized electrical field can be enhanced because of the CNP's curvature [22]. As a result, the effective electrical field around CNP is larger than the electrical field generated by gate voltages. Therefore, the threshold voltage is moved toward positive V_{GS} . In addition, it can be observed that the off current will not be increased significantly before the CNP amount is increased to a critical concentration. This critical concentration leads to the percolation of CNP. And the CNP percolation generates the additional conduction path and enhances the off current of fabricated devices. As a consequence, the carrier transportation can be enhanced without degrading on-off ratio before CNP concentration is larger than the critical percolation concentration.

To further understand the detail of the developed CNP/P3HT blending semiconductor material, scanning electron microscopy (SEM), X-ray diffraction (XRD), Fourier transform infrared spectroscopy (FTIR) measurement are carried out. The SEM picture of different concentration of CNP/P3HT is shown in Figure 4. Through Figure 4, the granule diameter of CNP/P3HT is around hundreds of nm. Compared with the average diameter of CNP, that is, 35 nm, it is clear that the CNP aggregation occurred even when CNP/P3HT blending solution is ultrasonicated before printing. These SEM pictures also indicate the formation of CNP/P3HT complexes. It should be noted that the aggregation becomes severed at the concentration of 10 wt.%. This leads to the alternative conduction path formed by the CNP aggregation.

At the same time, X-ray diffraction (XRD) measurement is used to study the crystalline behavior of different concentration of CNP/P3HT blending material. This result can be shown in Figure 5. In the case of the pristine P3HT thin film, the intensity of the (100) reflection is resulted from the lamellar layer structure. The relative weak peak around the (101) is resulted from π - π interchain stacking. It is clear that the pristine P3HT has a well-organized crystalline structure. As the ratio of CNP/P3HT increases from 0.1 wt.% to 10 wt.%, the (100) XRD peak decreases. This result reveals that CNPs affect P3HT molecular alignment and destroy the crystalline structure of P3HT. This result can be clearly visualized in Figure 4 that the CNP aggregation is disordered.

To understand the material property through the bonding structure, FTIR is used to study the CNP/P3HT complex and shown as Figure 6. It shows the strong absorption bands at 2956, 2925, and 2855 cm^{-1} , which means aliphatic C-H stretching of P3HT. As the concentration of CNP/P3HT increases, the absorption peak remains and no new absorption peak occurs. In other words, there

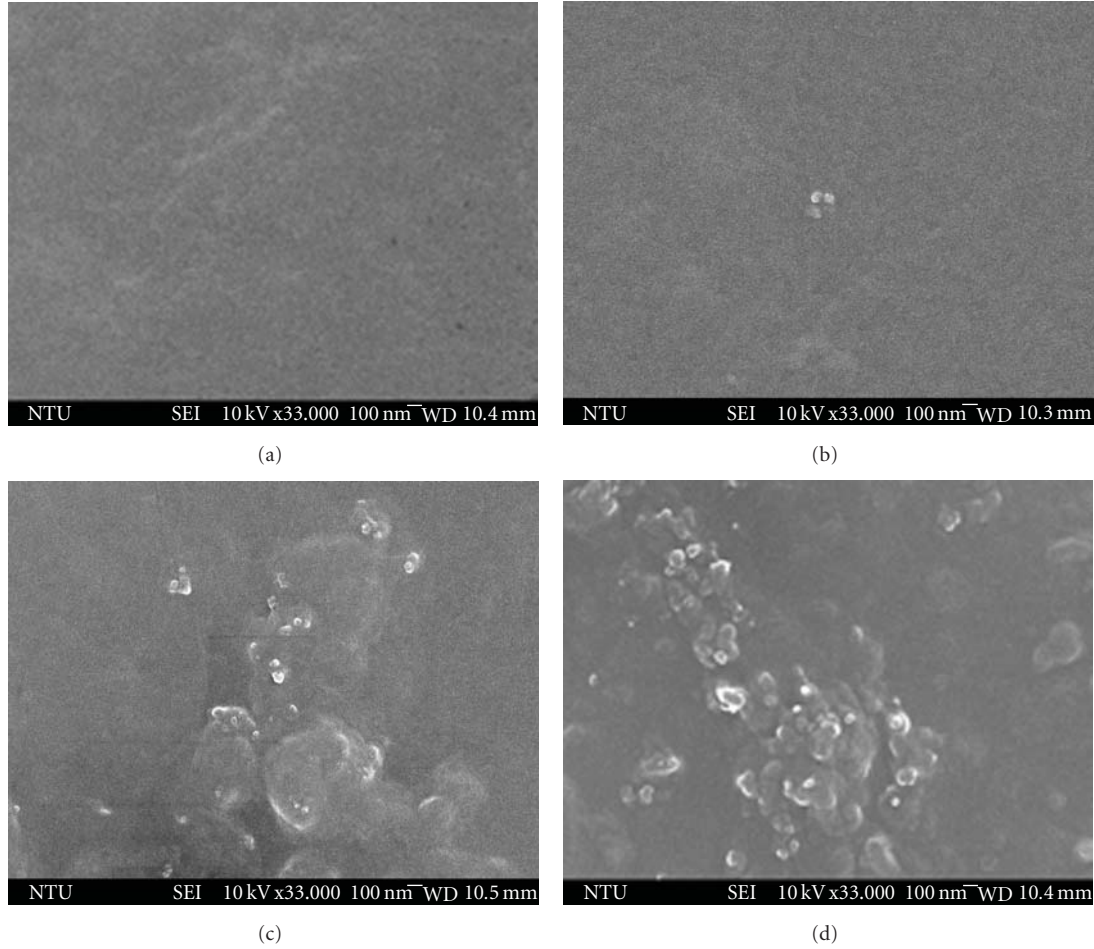


FIGURE 4: The SEM image for various concentration of CNP/P3HT blending solution (a) pristine P3HT; (b) CNP/P3HT = 0.1 wt.%; (c) CNP/P3HT = 1 wt.%; (d) CNP/P3HT = 10 wt.%.

TABLE 1: The experiment result of different OFETs.

	Pristine P3HT (as-pretreated)	Pristine P3HT	CNP/P3HT = 1/1000	CNP/P3HT = 10/1000	CNP/P3HT = 100/1000
On/Off ratio	1.07E4	3.41E4	8.24E4	1.60E4	4.76E4
V _{th} (V)	12	8	9.5	13	15
Mobility (cm ² /Vs)	0.0007	0.0014	0.0016	0.0017	0.0060

is no additional bonding formation through the addition of CNPs. As a result, there is no bonding formation within the CNP/P3HT complex. In the previous research work [24], the chemically functionalized multiwall carbon nanotubes (MWCNTs) formed the P3HT-grafted-MWCNTs (g-MWCNTs) to enhance the carrier mobility by establishing chemical bonds for charge transferring. Compared with this previous research work, CNP/P3HT complexes developed at this work promote the carrier mobility without bonding formation between CNP and P3HT. This leads to the major advantage of reducing the cost and complexity to prepare the material.

In general, the disorderliness in crystalline structure leads to a decrease in carrier mobility. In addition, there is no

chemical-bonding formation within CNP/P3HT complex. In other words, the direct carrier transportation between CNPs and P3HT cannot be promoted within CNP/P3HT complex. Since there is less alternative conduction path in low concentration of CNP/P3HT, that is, 0.1 wt.% and 1 wt.%, adding CNP should decrease the drain current and effective mobility. However, our experimental result indicates an enhancement in carrier mobility with an increase in CNP concentration. This result can be contributed to the localized field enhancement induced by CNP/P3HT complex [22]. Moreover, the hole-injection barrier of P3HT can be reduced by adding carbon nanostructures [29]. As a consequence, the overall performance of developed OFETs is enhanced by using CNP/P3HT as semiconductor layers. This

TABLE 2: The experimental transconductance of developed OFETs.

	Pristine P3HT (as pretreated)	Pristine P3HT	CNP/P3HT = 1/1000	CNP/P3HT = 10/1000	CNP/P3HT = 100/1000
Transconductance (nS)	2.8	4.5	11	7.2	16

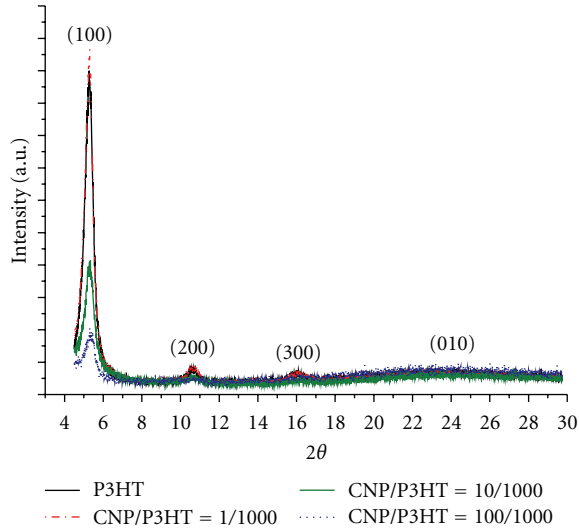


FIGURE 5: XRD image of pristine CNP/P3HT and different CNP concentrations.

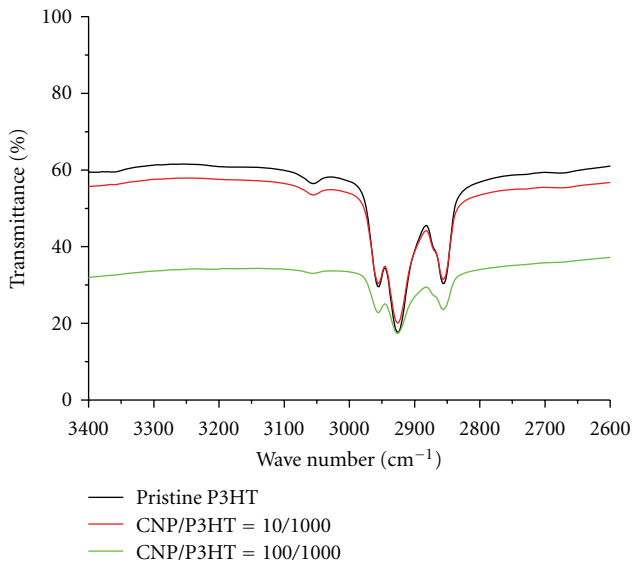


FIGURE 6: FTIR image of pristine CNP/P3HT and different CNP concentrations.

enhancement can be demonstrated as the transconductance improvement shown as Table 2. It should be noted that this transconductance is extracted from $I_D^{1/2}$ - V_{GS} curve. The transconductance can be determined at $V_{DS} = -20$ V by using the linear region drain current equation.

4. Conclusions

In summary, we have examined a CNP/P3HT blending semiconductor material for inkjet-printed OFETs. As CNP/P3HT concentration increases, the effective carrier mobility of each fabricated OFET increases. This carrier mobility enhancement is 8 folds for the comparison between pristine P3HT without O_2 plasma treatment and CNP/P3HT = 10 wt.%. At the same time, the on-off ratio of fabricated OFETs is kept above 10^4 . Based on the observation of SEM, XRD, and FTIR, this improvement can be contributed to the local field enhancement and the hole-injection lowering by CNP/P3HT complexes. This work offers a low-cost and effective semiconductor material for inkjet-printing technology in the development of organic electronics.

Acknowledgments

the authors would like to thank Dr. Yi-Jun Lin of Taiwan Textile Research Institute for her suggestion in material experiments. This work is supported by National Science Foundation (Grant no. NCS 98-2218-E-002-042, NSC 98-2221-E-002-139-MY, NSC 98-2627-E-002-003, and NSC99-2911-I-002-001).

References

- [1] T. Shimoda, Y. Matsuki, M. Furusawa et al., "Solution-processed silicon films and transistors," *Nature*, vol. 440, no. 7085, pp. 783–786, 2006.
- [2] G. H. Gelinck, H. E. A. Huitema, E. V. Veenendaal et al., "Flexible active-matrix displays and shift registers based on solution-processed organic transistors," *Nature Materials*, vol. 3, no. 2, pp. 106–110, 2004.
- [3] S. H. Eom, S. Senthilarasu, P. Uthirakumar et al., "Polymer solar cells based on inkjet-printed PEDOT:PSS layer," *Organic Electronics*, vol. 10, no. 3, pp. 536–542, 2009.
- [4] C. N. Hoth, P. Schilinsky, S. A. Choulis, and C. J. Brabec, "Printing highly efficient organic solar cells," *Nano Letters*, vol. 8, no. 9, pp. 2806–2813, 2008.
- [5] Y. K. Kim, K. Lee, N. E. Coates et al., "Efficient tandem polymer solar cells fabricated by all-solution processing," *Science*, vol. 317, no. 5835, pp. 222–225, 2007.
- [6] C. D. Müller, A. Falcou, N. Reckefuss et al., "Multi-colour organic light-emitting displays by solution processing," *Nature*, vol. 421, no. 6925, pp. 829–833, 2003.
- [7] S. I. Park, Y. J. Xiong, R. H. Kim et al., "Printed assemblies of inorganic light-emitting diodes for deformable and semi-transparent displays," *Science*, vol. 325, no. 5943, pp. 977–981, 2009.
- [8] P. F. Baude, D. A. Ender, M. A. Haase, T. W. Kelley, D. V. Muyres, and S. D. Theiss, "Pentacene-based radio-frequency identification circuitry," *Applied Physics Letters*, vol. 82, no. 22, pp. 3964–3966, 2003.

- [9] B. Crone, A. Dodabalapur, A. Gelperin et al., "Electronic sensing of vapors with organic transistors," *Applied Physics Letters*, vol. 78, no. 15, pp. 2229–2231, 2001.
- [10] J. A. Lim, J. H. Kim, L. Qiu et al., "Inkjet-printed single-droplet organic transistors based on semiconductor nanowires embedded in insulating polymers," *Advanced Functional Materials*, vol. 20, no. 19, pp. 3292–3297, 2010.
- [11] C. W. Sele, T. von Werne, R. H. Friend, and H. Sirringhaus, "Lithography-free, self-aligned inkjet printing with sub-hundred-nanometer resolution," *Advanced Materials*, vol. 17, no. 8, pp. 997–1001, 2005.
- [12] Y. Y. Noh, N. Zhao, M. Caironi, and H. Sirringhaus, "Downscaling of self-aligned, all-printed polymer thin-film transistors," *Nature Nanotechnology*, vol. 2, no. 12, pp. 784–789, 2007.
- [13] J. Y. Z. Zhang, Z. Wei, Y. Sum et al., "Inkjet-printed organic electrodes for bottom-contact organic field-effect transistors," *Advanced Functional Materials*, vol. 21, no. 4, pp. 786–791, 2011.
- [14] E. Tekin, P. J. Smith, S. Hoepfner et al., "Inkjet printing of luminescent CdTe nanocrystal-polymer composites," *Advanced Functional Materials*, vol. 17, no. 1, pp. 23–28, 2007.
- [15] Y. D. Park, H. S. Lee, Y. J. Choi et al., "Solubility-induced ordered polythiophene precursors for high-performance organic thin-film transistors," *Advanced Functional Materials*, vol. 19, no. 8, pp. 1200–1206, 2009.
- [16] S. Gamerith, A. Klug, H. Scheiber, U. Scherf, E. Moderegger, and E. J. W. List, "Direct ink-jet printing of Ag-Cu nanoparticle and Ag-precursor based electrodes for OFET applications," *Advanced Functional Materials*, vol. 17, no. 16, pp. 3111–3118, 2007.
- [17] H. Sirringhaus, P. J. Brown, R. H. Friend et al., "Two-dimensional charge transport in self-organized, high-mobility conjugated polymers," *Nature*, vol. 401, no. 6754, pp. 685–688, 1999.
- [18] F. M. Li, A. Nathan, Y. L. Wu, and B. S. Ong, "A comparative study of plasma-enhanced chemical vapor gate dielectrics for solution-processed polymer thin-film transistor circuit integration," *Journal of Applied Physics*, vol. 104, no. 12, Article ID 124504, 2008.
- [19] G. C. Yuan, Z. S. Lu, Z. Xu et al., "Microstructure transformations induced by modified-layers on pentacene polymorphic films and their effect on performance of organic thin-film transistor," *Organic Electronics*, vol. 10, no. 7, pp. 1388–1395, 2009.
- [20] L. Jiang, J. Zhang, D. Gamota, and C. G. Takoudis, "Enhancement of the field-effect mobility of solution processed organic thin film transistors by surface modification of the dielectric," *Organic Electronics*, vol. 11, no. 2, pp. 344–350, 2010.
- [21] J. Tsukamoto, J. Mata, and T. Matsuno, "Organic field effect transistors using composites of semiconductive polymers and single-walled carbon nanotubes," *Japanese Journal of Applied Physics*, vol. 46, no. 17–19, pp. L396–L398, 2007.
- [22] S. H. Liu, S. C. B. Mannsfeld, M. C. Lemieux, H. W. Lee, and Z. N. Bao, "Organic semiconductor-carbon nanotube bundle bilayer field effect transistors with enhanced mobilities and high on/off ratios," *Applied Physics Letters*, vol. 92, no. 5, Article ID 053306, 2008.
- [23] Y. D. Park, J. A. Lim, J. A. Yunseok et al., "Enhancement of the field-effect mobility of poly(3-hexylthiophene)/functionalized carbon nanotube hybrid transistors," *Organic Electronics*, vol. 9, no. 3, pp. 317–322, 2008.
- [24] Y. J. Song, J. U. Lee, and W. H. Jo, "Multi-walled carbon nanotubes covalently attached with poly(3-hexylthiophene) for enhancement of field-effect mobility of poly(3-hexylthiophene)/multi-walled carbon nanotube composites," *Carbon*, vol. 48, no. 2, pp. 389–395, 2010.
- [25] M. W. Lee and C. K. Song, "Oxygen plasma effects on performance of pentacene thin film transistor," *Japanese Journal of Applied Physics*, vol. 42, no. 7 A, pp. 4218–4221, 2003.
- [26] B. J. Song, K. Hong, W. K. Kim, K. Kim, S. Kim, and J. L. Lee, "Effect of oxygen plasma treatment on crystal growth mode at pentacene/Ni interface in organic thin-film transistors," *Journal of Physical Chemistry B*, vol. 114, no. 46, pp. 14854–14859, 2010.
- [27] M. Bruening, E. Moons, D. Cahen, and A. Shanzer, "Controlling the work function of CdSe by chemisorption of benzoic acid derivatives and chemical etching," *Journal of Physical Chemistry*, vol. 99, no. 20, pp. 8368–8373, 1995.
- [28] A. Paskaleva and E. Atanassova, "Bulk oxide charge and slow states in Si-SiO₂ structures generated by RIE-mode plasma," *Microelectronics Reliability*, vol. 40, no. 12, pp. 2033–2037, 1999.
- [29] Y. D. Park, J. A. Lim, J. A. Yunseok et al., "Enhancement of the field-effect mobility of poly(3-hexylthiophene)/functionalized carbon nanotube hybrid transistors," *Organic Electronics*, vol. 9, no. 3, pp. 317–322, 2008.

Research Article

Molecular Engineering of Nonplanar Porphyrin and Carbon Nanotube Assemblies: A Linear and Nonlinear Spectroscopic and Modeling Study

Éimhín M. Ní Mhuircheartaigh,¹ Silvia Giordani,¹ Donal MacKernan,² Sharon M. King,¹ David Rickard,¹ Lisa M. Val Verde,^{1,3} Mathias O. Senge,⁴ and Werner J. Blau¹

¹ School of Physics, Trinity College Dublin, Dublin 2, Ireland

² School of Physics, University College Dublin, Dublin 4, Ireland

³ Materials Research Laboratory, University of California, Santa Barbara, CA 93106-5121, USA

⁴ School of Chemistry, SFI Tetrapyrrole Laboratory, Trinity College Dublin, Dublin 2, Ireland

Correspondence should be addressed to Werner J. Blau, wblau@tcd.ie

Received 2 March 2011; Accepted 13 June 2011

Academic Editor: Marisol Reyes-Reyes

Copyright © 2011 Éimhín M. Ní Mhuircheartaigh et al. This is an open access article distributed under the Creative Commons Attribution License, which permits unrestricted use, distribution, and reproduction in any medium, provided the original work is properly cited.

The importance of molecular conformation to the nature and strength of noncovalent interactions existing between a series of increasingly nonplanar tetraphenylporphyrin (TPP) derivatives and carbon nanotubes was systematically investigated experimentally in solution using a range of linear and nonlinear optical techniques. Additional complementary molecular dynamics studies were found to support the experimental observations. Convincing evidence of binding between single walled nanotubes (SWNTs) and some of these porphyrins was discovered, and a nonplanar macrocycle conformation was found to increase the likelihood of noncovalent binding onto nanotubes. Nonlinear optical studies showed that the optical limiting behavior of the TPP derivatives deteriorated with increasing porphyrin nonplanarity, but that formation of nanotube composites dramatically improved the optical limiting properties of all molecules studied. It was also found that the significant photoluminescence quenching behavior reported in the literature for such porphyrin/SWNT composites is at least partly caused by photoluminescence and excitation self-absorption and is, therefore, an artifact of the system.

1. Introduction

Natural cofactors are often found to be tetrapyrroles, due to the high versatility of these organic structures. The functional variety afforded by this class of compounds is related to the flexibility of their molecular conformations, as the physicochemical properties of such molecules may be tuned through the manipulation of the macrocycle. In recent years, porphyrins with such nonplanar macrocyclic conformations have thus attracted considerable attention in an attempt to understand the relationship between conformational distortion and photophysical properties [1–3]. Single-walled carbon nanotubes (SWNTs) are promising materials for future nanoscale devices, because of their unique structural, mechanical, and electronic properties and have thus attracted much attention since their discovery in

1991 [4]. However, SWNT solubility in aqueous and organic solutions remains a concern and may be achieved chemically while maintaining the superior nanotube electronic structure through noncovalent functionalization [5–9]. Since the initial report by Murakami et al. on nanocomposites formed by van der Waals forces between SWNT and zinc protoporphyrin IX, much research has been conducted on such noncovalent SWNT–porphyrin hybrid materials. Through functionalization with porphyrins, it is hoped that SWNT may gain the superior physicochemical properties of the porphyrin moiety. Indeed, in a previous report by the authors [10], it has been shown that the solubility and optical limiting (OL) properties of carbon nanotubes are enhanced upon interaction with the planar porphyrins tetraphenylporphyrin and protoporphyrin IX in solution [11, 12]. At least,

two distinct processes are widely believed to contribute to optical limiting of noncovalently bonded porphyrin-SWCNT complexes in solution. The first, nonlinear scattering is due to the formation of bubbles in the solvent. This happens at the beginning of a laser pulse, when the leading edge helps heat carbon nanoparticles to form solvent nanobubbles, a process which takes place on a nanosecond time scale. The resulting liquid-gas interface and the associated abrupt change in refractive index lead to intense nonlinear scattering and optical limiting. The second process is considered to consist of reverse saturable absorption (where the absorption cross-section of excited states exceeds that of the ground state) by the porphyrin of the laser, followed by electron, or possibly energy transfer from the excited porphyrin to the SWCNT. Either of these transfer processes is greatly enhanced if the distance between the donor and acceptor is small, as would be the case were the porphyrin to have a tendency to bind noncovalently to the SWCNT. In this scenario, the excited SWCNT relaxes to its ground state nonradiatively through internal electronic-phonon coupling, and interactions with the solvent. Noncovalent interactions between SWCNT and nonplanar porphyrins are, therefore, a very interesting novel nanotech approach. Up until now, interactions have been studied between SWCNT and predominantly planar porphyrin systems. The correlation, if any, existing between the degree of macrocycle nonplanarity and the strength of the subsequent binding for these nanotube composites is potentially very interesting. Engineering molecules which map onto the nanotube surface appears the logical approach, and, for this reason, a series of six β -ethyl-substituted tetraphenylporphyrins were synthesized using a technique previously reported [13, 14] with varying graded degrees of distortion due to *peri*-interactions ranging from that of tetraphenylporphyrin (H_2 TPP) to the standard nonplanar porphyrin 2,3,7,8,12,13,17,18-octaethyl-5,10,15,20-tetraphenylporphyrin (H_2 OETPP) [15]. Porphyrins are also well known for their novel optical nonlinear properties and are, therefore, one of the most studied class of compounds in this field [2, 16, 17]. It has been shown that SWCNTs and multiwalled nanotubes (MWNTs) in suspension excited with high intensity at 532 nm and 1064 nm also behave as reverse saturable absorbers [18–20]. The interactions between SWCNT and the sterically crowded, nonplanar porphyrins investigated in this report in solution are likely to give rise to interesting optical nonlinear behavior for these composite solutions. Thus, the optical properties of carbon nanotubes noncovalently functionalized with nonplanar porphyrin molecules are of enormous interest from the point of view of both their photophysical and nonlinear optical properties and potential applications.

In this paper, we present a comprehensive linear and nonlinear optical characterization of the interaction between the porphyrin and nanotube moieties. We also present evidence that much of the optical evidence attributed to strong noncovalent binding in these systems by other authors is likely to be an artifact, resulting from a well-known optical phenomenon. The experimentally determined linear and nonlinear optical characteristics of these porphyrin composite systems in solution are also compared with the

results of a molecular dynamics simulation performed in the NVT ensemble (i.e., the number of particles N , the volume V , and the temperature T of the system are kept constant), where the tendency exhibited by these tetraphenylporphyrin derivatives to aggregate close to a nanotube surface in the same solvent was investigated.

2. Experimental Section

The purified SWCNTs used in this work were prepared by the HiPCO process [21], supplied by Carbon Nanotechnologies Inc., and used without further treatment. The nonplanar tetraphenylporphyrin (TPP) derivatives were prepared as described earlier [13, 14]. The TPP molecules used were purchased from Aldrich. Two identical sets of solutions of each porphyrin were made with concentrations ranging from approximately $1\ \mu\text{M}$ – $500\ \mu\text{M}$ in dimethylformamide (DMF). Pure HiPCO SWCNT was added to one porphyrin solution at each concentration yielding solutions with porphyrin-SWCNT mass ratios of 1 : 1, 5 : 1, and 10 : 1.

Photoluminescence measurements were carried out using an LS-55 Perkin-Elmer luminescence spectrometer. The linear absorption spectra were recorded using a Shimadzu UV3100 UV-Vis-NIR spectrometer. Nonlinear optical experiments were performed using the open aperture Z-scan technique [22]. This technique involves scanning the sample through the focus of a Gaussian laser beam, thereby, subjecting it to a large range of intensities. Negligible nonlinear activity occurs initially, when the beam energy density is low, and as the sample approaches the focus, the energy density increases exciting the nonlinear activity within the sample medium. The open aperture Z-scan spectrum acquired during such a scan is the measured beam transmittance as a function of position from the focus, from which the nonlinear extinction coefficient can be extracted. Fitting theory previously reported was used in the calculation of effective absorption coefficients for all systems studied [23]. All experiments were performed using 6 ns Gaussian pulses from a Q-switched Nd:YAG laser with energies of approximately 0.2–0.3 mJ per pulse. The beam was spatially filtered to remove the higher-order modes and tightly focused. The laser was operated at its second harmonic, 532 nm, with a pulse repetition rate of 10 Hz. All linear and nonlinear optical measurements were performed in quartz cells of either 1 cm or 2 mm path length.

A molecular simulation of the series of nonplanar TPP derivatives in the presence of a 7-7 SWCNT in the solvent DMF was also undertaken. All of the simulations were performed using the “COMPASS” force field [24], which is the first force field which has been parameterized and validated using condensed phase properties in addition to various ab initio and empirical data. This molecular force field includes 2, 3, and 4 body terms describing nonbond and bond interactions. The nonbond contributions consist of coulomb (via partial charges) and Van der Waals interactions. The bond (or valence) interactions consist of bond stretching terms, valence angle bending terms, dihedral angle torsion terms, and inversion (also called out-of-plane interactions) terms.

A 7-7 SWNT has a radius close to that of HiPCO SWNT. This computational work utilized a molecular dynamics simulation (NVT ensemble) to investigate whether the TPP derivatives exhibited enhanced tendencies to aggregate onto the surface of a SWNT in the presence of DMF solvent molecules at standard density (0.944 g/cm^3) and temperature (298 Kelvin). Each system was simulated in a periodic box of size roughly $65 \times 65 \times 41.81 \text{ \AA}^3$, with small differences made to take into account small differences in effective volume of different porphyrin derivatives. The initial conditions in all cases consisted of three layers. The left and right layers each consisted of ten porphyrin molecules in a solvent of 500 DMF molecules, while the middle layer consisted of an uncapped 7-7 SWNT of length 41 \AA . Each system thus consisted of 20 TPP derivative molecules, 1000 DMF molecules and a single SWNT. Each system was equilibrated for at least 1 ns, and statistics were subsequently collected for a further 0.2 ns. The COMPASS force field was used, and Coulombic and Van der Waals contributions to the forces were computed using a fast: cell multipole technique due to rapid convergence and high precision (almost the same as that obtained with Ewald sums). The NVT ensemble was then sampled using Anderson thermostated molecular dynamics, and an integrating time step of 1 fs.

3. Results and Discussion

In order to study the correlation between macrocycle nonplanarity for porphyrin molecules and their noncovalent interactions with carbon nanotubes, a series of porphyrins with graded degree of macrocycle distortion was synthesized via mixed condensation of pyrrole, diethylpyrrole, and benzaldehyde as previously described [13, 14]. The behavior of the nanotube composites formed with these nonplanar porphyrins was compared with that of the more planar molecule tetraphenylporphyrin (TPP).

Limited solubility was observed for the HiPCO SWNT solely in DMF for concentrations below 0.01 gL^{-1} . It was found that TPP and its more distorted derivatives 2,3-diethyl-5,10,15,20-tetraphenylporphyrin (DETTP), 2,3,12,13-tetraethyl-5,10,15,20-tetraphenylporphyrin (tTETTP), 2,3,7,8-tetraethyl-5,10,15,20-tetraphenylporphyrin (cTETTP), 2,3,7,8,12,13-hexaethyl-5,10,15,20-tetraphenylporphyrin (HETTP), and 2,3,7,8,12,13,17,18-octaethyl-5,10,15,20-tetraphenylporphyrin (OETTP) could all dissolve SWNT in DMF. Crystallographic studies have previously shown that the macrocycle distortion in the solid state for these molecules increases gradually in the order $\text{TPP} < \text{DETTP} < \text{tTETTP} < \text{cTETTP} < \text{HETTP} < \text{OETTP}$ [13, 14]. Negligible precipitation was noticed in these composite solutions even after several months of storage.

Porphyrin molecules are expected to bind noncovalently to carbon nanotubes through Van der Waals interactions as a result of their high degree of conjugation. Several reports of such noncovalently functionalized carbon nanotube systems exist, including previous studies performed by the authors [10, 25]. Adhesion of Zn-TPP molecules to the surface of carbon nanotubes has previously been

observed with TEM, providing some evidence of interaction between the two moieties in solution. A slow aggregation of the porphyrin: SWNT composite solutions were noticed when the concentration of the dispersion was greater than $59 \mu\text{M}$ for solutions where the porphyrin: nanotube mass ratio was 1:1, and approximately $100 \mu\text{M}$ for the 5:1 and 10:1 porphyrin: nanotube solutions. This confirmed that noncovalent porphyrin interaction enhanced the solubility of carbon nanotubes in DMF.

The TPP derivative molecules in dimethylformamide all displayed typical absorption spectra, with Soret bands observed ranging between 417 nm and 453 nm (Figure 1(a)). The Soret band of each porphyrin was found to shift to a lower energy with increasing porphyrin non-planarity relative to the TPP molecule with bands observed at 417, 420, 424, 432, 442, and 453 nm for TPP, DETTP, tTETTP, cTETTP, HETTP, and OETTP, respectively. The porphyrin nonplanarity results from a gradual distortion of the porphyrin macrocycle due to steric crowding with each additional ethyl group added [13, 14]. These absorption band red shifts are characteristic of nonplanar porphyrins, where the degree of non-planarity of a molecule is often determined by examination of such spectral shifts [2, 26, 27].

Upon interaction with the carbon nanotubes, the composite visible-NIR absorption spectra are intermediate between the spectrum of the SWNT suspension and the porphyrin spectrum, with Q bands and Van Hove peaks present, but slightly shifted in some cases (HETTP and OETTP) for the 1:1 composite solutions. For the 5:1 and 10:1 composites, no change in the absorption spectrum was observed, with the composite displaying peaks originating from both the individual porphyrin molecules and the carbon nanotube Van Hove absorption peaks at 377, 409, 451, 504, 559, 602, and 658 nm. Further evidence of increased nanotube solubility in the presence of the porphyrins was confirmed by the intensity increase of the Van Hove peaks for the composite solutions using UV-visible-near IR absorption spectroscopy (Figure 1(b)).

The fluorescence spectra for excitation at the Soret band of each solution present two emission peaks characteristic of porphyrin photoluminescence for the two most planar samples, TPP and DETTP. The emission deviates from this pattern with increasing macrocycle distortion, with one broad peak observed for tTETTP, cTETTP, and HETTP displaying PL which is barely resolved into two peaks. As the porphyrin macrocycle becomes more perturbed, the luminescence becomes increasingly less intense, with no measurable fluorescence observed for OETTP. The emission wavelengths were also found to red shift with increasing macrocycle nonplanarity [28, 29]. It was not possible to determine if this was true for the nonfluorescent molecule OETTP. The Stokes shift also increased with increasing molecule nonplanarity, with values of 232, 232, 246, 269, and 308 nm for TPP, DETTP, tTETTP, cTETTP, and HETTP, respectively. Upon the formation of a (1:1) composite with the SWNT, the emission profile was unchanged for all porphyrins studied.

In a previous report [10], it was found that both TPP and its metalloporphyrin derivative Zn-TPP displayed

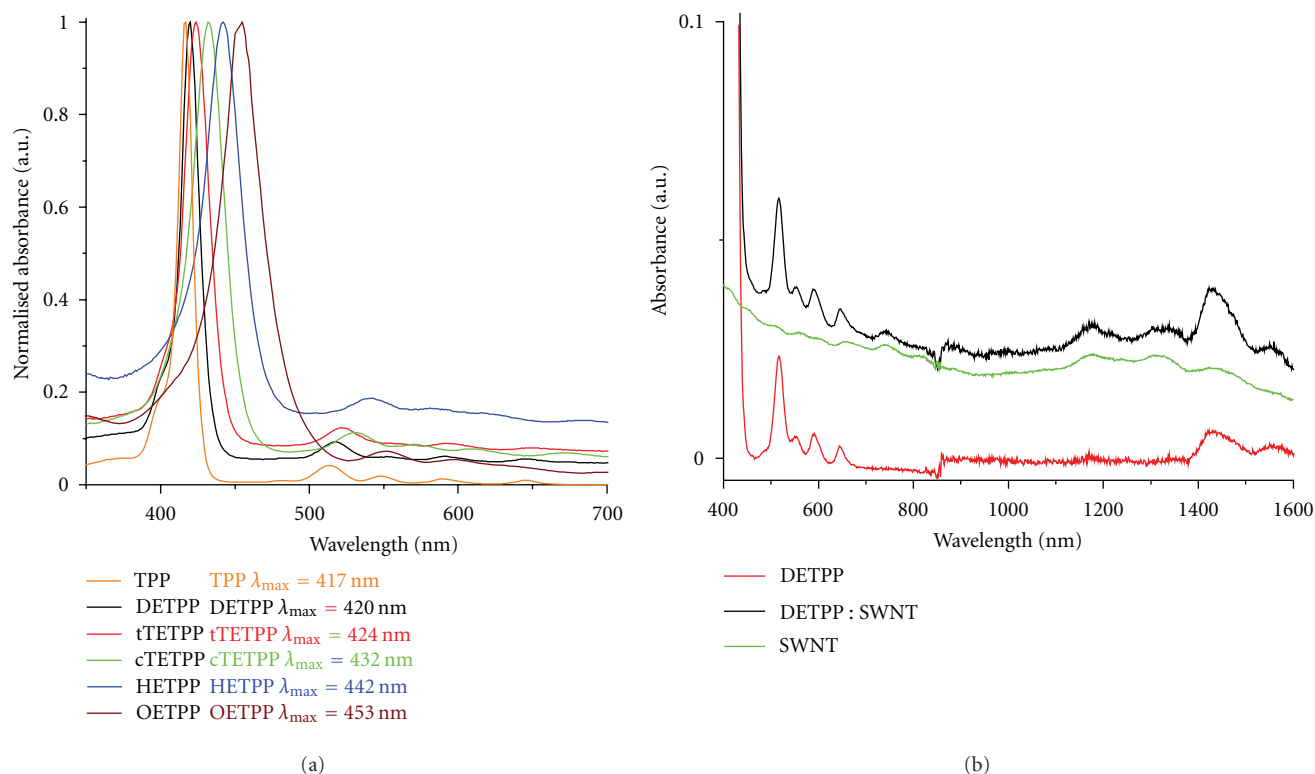


FIGURE 1: (a) Normalized UV-VIS absorption spectra of TPP, DETPP, tTETPP, cTETPP, HETPP, and OETPP and their (1 : 1) SWNT composites (0.001 mg/mL, DMF, 25 °C). (b) The VIS-NIR absorption spectra of DETPP, its (1 : 1) SWNT composite, and a dispersion of SWNT alone in DMF show the characteristic Q Bands and Van Hove peaks and show that the absorption spectrum of the composite solution is intermediate between that of the porphyrin and the SWNT with characteristics of both.

negligible quenching for (1 : 1) composite solutions at porphyrin concentrations below $6.5 \mu\text{M}$, with self-aggregation of the solutions appearing evident at higher concentrations where strong PL quenching was observed for the composite solutions. In the context of this paper, we define aggregation as a generic term which describes any interaction between individual molecules which in turn affects the electronic structure of the individual molecule (including π - π stacking and other nonpolar interactions). These findings were consistent with the literature, where strong photoluminescence quenching of composite solutions was attributed to evidence of noncovalent binding of porphyrin molecules to carbon nanotubes [30–33]. Such studies were typically performed at only one concentration at the same high concentrations where we had also found strong quenching [10]. In this report, we present evidence that this reported photoluminescence behavior for porphyrin composite solutions is not an effect entailing significant electronic changes in the SWNT's but is largely the result of a common photoluminescence phenomenon. Our findings imply that many of the optical findings which support noncovalent porphyrin functionalization reported in the literature may be artifacts and not actually attributable to either energy transfer or photoinduced electron transfer from the bound porphyrins to the SWNT as suggested. Under commonly used experimental conditions, the observed fluorescence signal from a solution can be found to decrease relative to the

sample concentration as the solution becomes increasingly concentrated. This decrease is due, in part, to an attenuation of the excitation beam in regions of the solution in front of the point from which the fluorescence is collected by the detector, and to the absorption of the emitted fluorescence within the solution [34]. This effect is known as the inner filter effect, as defined by Parker and Rees [35].

The variation in photoluminescence intensity was studied as a function of concentration for composite solutions over a wide concentration range. Assuming noncovalent binding of the porphyrins onto the carbon nanotube surface through Van der Waals interactions, the photoluminescence of the composite solutions is expected to be quenched relative to that of the same concentration of porphyrin, consistent with a model developed by Coleman et al. [36] which accurately describes noncovalent nanotube interactions with the conjugated polymer poly [*m*-phenylenevinylene-co-(1,5-dioctyloxy-2,6-naphthylene vinylene)] (pmNV). Due to constant porphyrin adsorption/desorption from the nanotubes, the extent of this photoluminescence quenching is predicted to be highly nonlinear with concentration approaching 1 at very low concentrations.

Concentration-dependent PL studies were performed upon the series of tetraphenylporphyrin derivatives and their 1 : 1, 5 : 1 and 10 : 1 composites formed with SWNT in order to determine the extent of the noncovalent binding. For the 1 : 1 DETPP : SWNT solutions, quenching behavior was

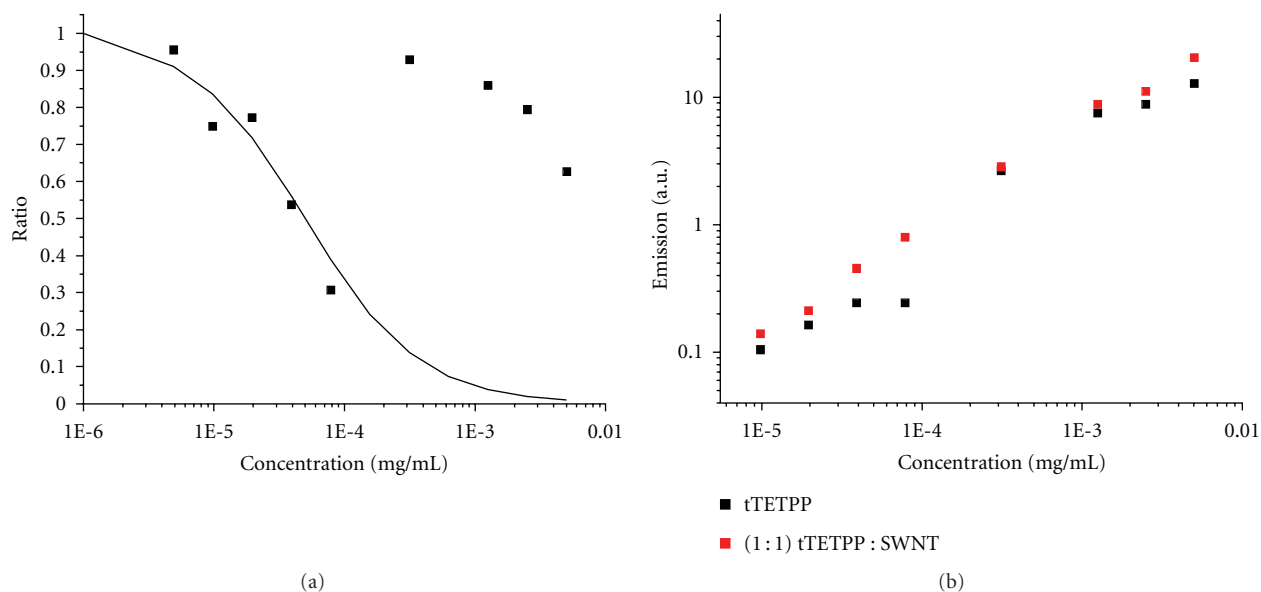


FIGURE 2: The PL quenching behaviour of tTETPP appeared to be in conservative agreement with the binding model at concentrations sufficiently dilute display an appreciable level of emission quenching.

observed for the composite solutions for concentrations greater than approximately 1×10^{-4} mg/mL with an appreciable reduction in the porphyrin fluorescence for SWNT composites observed. Our data initially appeared to be in tenuous agreement with the binding model proposed by Coleman et al., with very weak interaction indicated between the nanotubes and the porphyrin solutions. However, this occurred at the onset of the concentration-dependent emission quenching, similar to the behavior previously found for TPP and Zn-TPP. The PL behavior of DETPP displayed only 15% quenching at sufficiently dilute concentrations where emission intensity was directly proportional to concentration (i.e., for concentrations $< 5 \times 10^{-4}$ mg/mL). Negligible quenching was observed in this concentration range for cTETPP and HETPP. It was also observed that both emission bands, particularly the more intense band at 654 nm, were much lower in intensity at higher concentration solutions for spectra normalized at 693 nm. This effect became more marked with increasing concentration, consistent with the inner filter effect. Only (1:1) composite solutions of one of the porphyrin molecules studied—tTETPP—appeared to display an appreciable level of emission quenching, in conservative agreement with the binding model (Figure 2) at these dilute concentrations. It is worth noting that OETPP was nonfluorescent, and so it was not possible to probe the interaction of this molecule with SWNT using this technique.

Two steps were taken in order to examine the role of the inner filter effect in our studies. Firstly, as one characteristic of the inner filter effect is that fluorescence emission spectra excited in regions of high absorbance are suppressed, the effects on the PL of exciting at different wavelengths were examined. Secondly, it is well documented that cell geometry is of great importance in the inner filter effect. To minimize this phenomenon at high concentrations, the 1 cm quartz cuvette was replaced with a 2 mm quartz

cuvette, which was mounted in a specially designed holder within the fluorimeter. The influence of the inner filter effect was immediately apparent upon examination of composite solutions containing 10:1 porphyrin: SWNT when both steps were taken to minimize this effect. Additionally, the solutions were all photoexcited at a number of wavelengths, namely, in the Soret and Q-bands of the porphyrin, and in a region of no absorbance. The difference in the emission for higher concentration solutions was significant. Concentration-induced self-absorption was greatly reduced by altering the excitation wavelength. It is apparent that the inner filter effect is responsible for much of the PL quenching observed for composite solutions at high concentration, as this effect was greatly enhanced in the presence of SWNT. This is probably due to the combination of light being scattered by the nanotubes in addition to the self-absorption of the porphyrin molecules present. Hence, strong apparent composite PL quenching was observed for all molecules studied when appropriate precautions were not taken to counter the effects of the inner filter effect.

Taking this into account, PL studies of all molecules were conducted. Plots of TPP and its 10:1 composite emission upon photoexcitation in the Soret band region at 417 nm (top) and the Q band region at 590 nm (bottom) for TPP as a function of concentration for high concentration solutions are shown in Figure 3. Also shown is the ratio of composite to porphyrin emission as a function of concentration upon excitation at both wavelengths. The 2 mm cuvette was used for all solutions at concentrations higher than 0.001 mg/mL. It is evident that negligible quenching is found for the composite solutions upon excitation at both wavelengths. This is in direct contrast to our previous studies with 1:1 TPP:SWNT composites, where 92% “quenching” was observed for composites at a concentration of 0.036 mg/mL. As this result was consistent with those reported in literature,

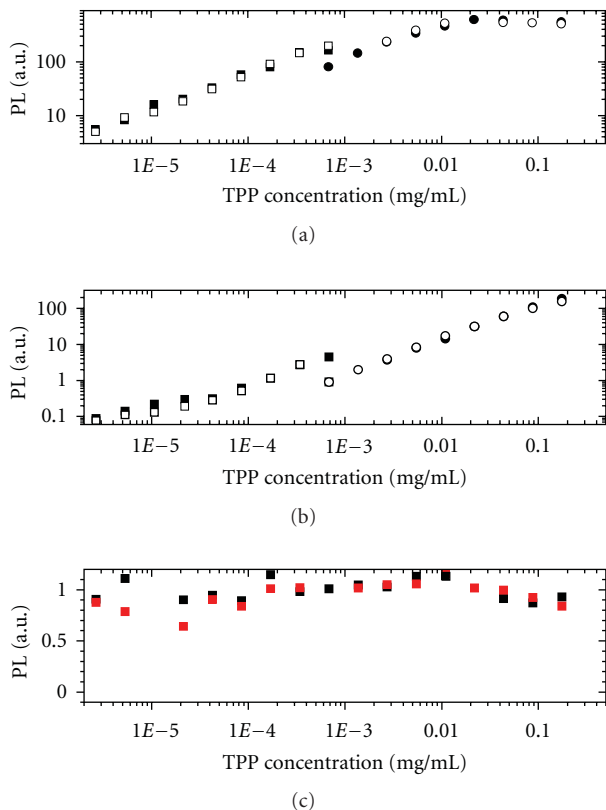


FIGURE 3: PL emission of TPP and its 10:1 SWNT composite upon photoexcitation in the Soret band region at 417 nm (a) and the Q band region at 590 nm (b) as a function of concentration for high concentration solutions. Also shown is the ratio of composite to porphyrin emission as a function of concentration upon excitation at both wavelengths. The 2-mm cuvette was used for all solutions at concentrations higher than 0.001 mg/mL.

it is likely that many other studies have failed to correct for the inner filter effect.

Some quenching was in fact found for the 10:1 tTETPP composites. However, the quenching remained approximately constant over the concentration range 0.001–0.175 mg/mL, yielding a median quenching of 25.2%. No quenching whatsoever was evident for (10:1) solutions of cTETPP, HETPP, and DETPP. For comparison purposes, (10:1) solutions of the planar molecule octaethylporphyrin (OEP) were also studied, and no change was noted in the PL intensity levels upon the addition of nanotubes, except that the luminescence was possibly slightly enhanced.

A series of (5:1) porphyrin:SWNT solutions were also examined for the planar molecules TPP and OEP. In both cases, the composite luminescence appeared to be enhanced relative to that of the same concentration of porphyrin. As the interaction of the porphyrin molecules with nanotubes is expected to quench the emission intensity, if anything, it is clear that the system is not as straightforward as initially thought. One possible explanation for this behavior is that the porphyrin molecules aggregate in DMF, and that interaction with the nanotubes prevents this aggregation from occurring. Although these molecules do not bind to

the nanotube surface in a way which facilitates photoinduced electron transfer, the noncovalent interactions between them appear stronger than the attractive forces between adjacent porphyrin molecules. Interestingly, (1:1) Zn-TPP:SWNT solutions also exhibited composite luminescence which was approximately 17% higher than those of the porphyrin solutions for concentrations lower than 1.7×10^{-4} mg/mL. Our results for (1:1) TPP:SWNT were inconclusive at these concentrations.

The absence of PL quenching observed for the (10:1) composite solutions of these molecules is also consistent with this theory. With a greater mass of porphyrins than nanotubes present in these solutions by an order of magnitude, it is clear that this quantity of nanotubes has no measurable impact on the degree of self-aggregation. With fewer SWNT present in solution, fewer sites for porphyrin aggregation are provided, and consequently the SWNTs have less effect on the porphyrins present in solution. The ratio of composite to porphyrin PL as a function of concentration is shown below for the 5:1 TPP:SWNT solutions, showing that the composite luminescence is higher than that of its corresponding TPP solution over the concentration range studied. These results are consistent with the molecular simulation results where a pronounced tendency to aggregate both onto the SWNT surface and onto each other was exhibited by these porphyrin molecules (Figure 4).

Increasing the ratio of porphyrin to SWNT in solution from 1:1 (to 5:1 and 10:1) porphyrins to nanotube by weight, it was found that maximum porphyrin concentrations of 0.04375 mg/mL and 0.175 mg/mL were achieved for the 5:1 and 10:1 composites, respectively, before the SWNT aggregated out of solution, equivalent to 0.00875 mg/mL and 0.0175 mg/mL of SWNT, respectively. As a maximum SWNT concentration of approximately 0.01 mg/mL was achieved for the 1:1 composite solutions, the maximum nanotube concentration appears to remain approximately constant, irrespective of the number of porphyrin molecules available to aid solubilization.

3.1. Nonlinear Optical Results. The open aperture of a Z-scan experiment was used to measure the total transmittance through the samples [37]. Effective absorption coefficients were calculated by fitting theory previously reported [23]. Normalized transmittance as a function of position z , $T_{\text{Norm}}(z)$ was given by

$$T_{\text{Norm}}(z) = \frac{\ln[1 + q_0(z)]}{q_0(z)}, \quad (1)$$

where $q_0(z) = q_{00}/(1 + (z/z_0)^2)$, z_0 is the diffraction length of the beam, $q_{00} = \beta_{\text{eff}} I_0 L_{\text{eff}}$.

Here, $L_{\text{eff}} = [1 - \exp(-\alpha_0 L)]/\alpha_0$, β_{eff} is the effective intensity-dependent nonlinear absorption coefficient, and I_0 is the intensity of the light at focus. L_{eff} is known as the effective length of the sample defined in terms of the linear absorption coefficient, α_0 , and the true optical path length through the sample, L . The imaginary third-order optical susceptibility $\text{Im}\{\chi^{(3)}\}$ is directly related to the intensity-dependent absorption coefficient β_I and is expressed as

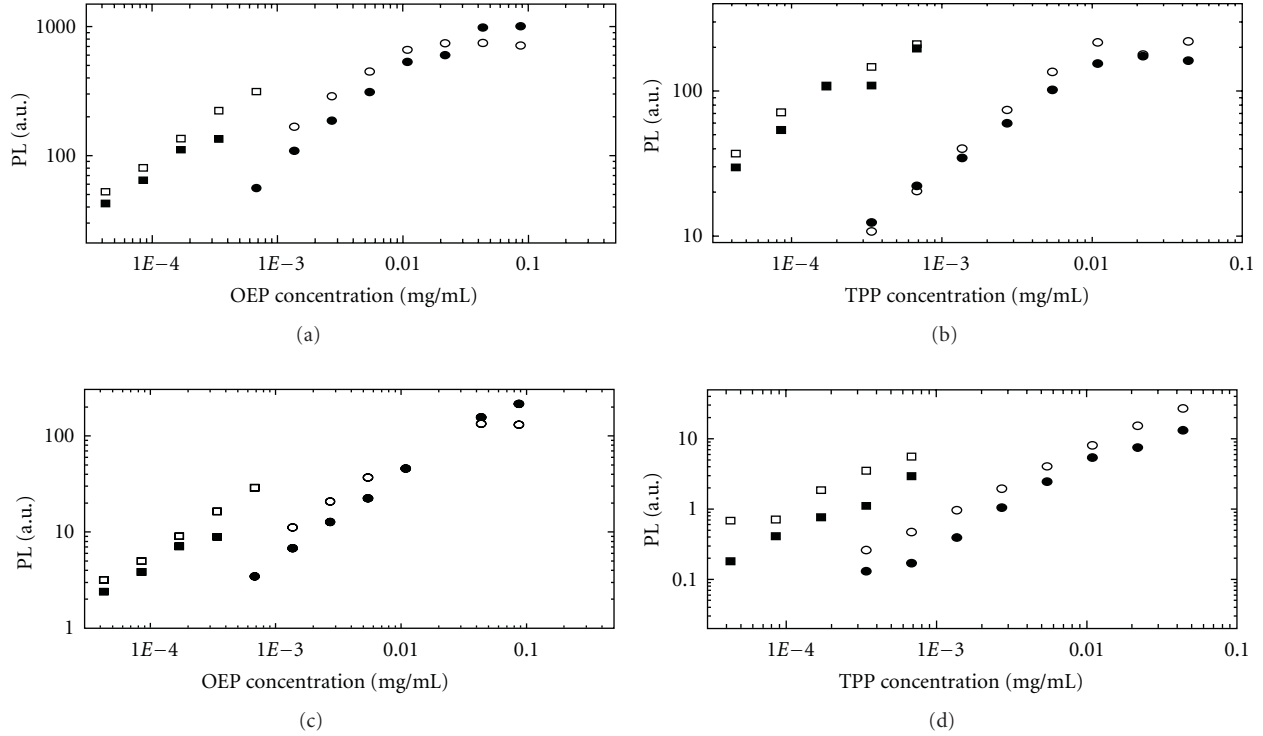


FIGURE 4: PL intensity as a function of concentration for 5 : 1 porphyrin : SWNT solutions for OEP (a, c) and TPP (b, d) show enhanced luminescence for composites. These solutions were photoexcited at the Soret band (a, b) (396 nm and 417 nm for OEP and TPP, resp.) and Q band (c, d) (529 nm and 590 nm for OEP and TPP, resp.) wavelengths. Measurements were performed in 2 mm quartz cuvettes for concentrations higher than 0.0003 mg/mL. A 1 cm quartz cuvette was used for all other measurements.

$\text{Im}\{\chi^{(3)}\} = n_0^2 \epsilon_0 c \lambda \beta_I / 2\pi$, where n_0 is the linear refractive index, ϵ_0 is the permittivity of free space, c is the speed of light, and λ is the wavelength of the incident light. All experiments described in this study were performed using 6 ns Gaussian pulses from a Q-switched Nd:YAG laser with energies of approximately 0.2–0.3 mJ per pulse. A normalized energy transmission without an aperture (i.e., open aperture) is shown in Figure 5 for a range of input energies at low onfocus intensities. All tetraphenylporphyrin derivatives were studied at a concentration of 0.01 mg/mL along with their single-wall nanotube composite solutions, with linear transmission in the region of 50–80%. These solutions were prepared and studied in DMF.

All Z scans performed in this study exhibited a reduction in transmittance about the focus at low intensities (see Figure 5). This is typical of nonlinear absorption of incident light being induced in the sample. For higher incident intensities ($I_0 > \sim 0.2 \text{ GW/cm}^2$), all of the nonplanar porphyrins were found to completely decompose the transmission of the porphyrin solutions about the focus displaying apparent saturable absorption (SA). Confirmation that this was a degradation effect as opposed to genuine SA taking place came from examination of the Z-scan traces obtained. Similar degradation effects have been seen in recent studies of optical limiting effects in linear carbon chains in water [38].

For an open aperture scan, the transmission as a function of distance from the focus typically changes symmetrically. More importantly, the initial and final transmission should

be the same for a given scan (i.e., 100% after normalization of these plots). It can clearly be seen that this is not the case for the nonplanar porphyrin scans, an example of which is shown in Figure 5(f). For each case, the transmittance after the scan is much higher than the initial transmittance, indicating the destruction of materials present in the solution.

All composite Z scans performed in this study exhibited a reduction in transmittance about the focus. This is typical of nonlinear absorption of incident light being induced in the sample. As previously [10] reported for TPP composites, introduction of carbon nanotubes into the system completely prevented this degradation at all irradiances, most likely due to the remarkable thermal conduction properties of carbon nanotubes preventing local heating in these solutions.

The nonlinear absorption coefficient, β_I , experienced by the incident pulses was determined from these spectra as a function of the onfocus intensity. The values of β_I and $\text{Im}\{\chi^{(3)}_{\text{eff}}\}$ were found to decrease in magnitude as nonplanarity increased. This means that deteriorating optical limiting behavior is observed as molecules become more nonplanar. No trend was observed in the value of $\text{Im}\{\chi^{(3)}\}$ as a function of planarity for the composite solutions. The composites were found to be better optical limiters than porphyrin molecules alone. All nonplanar porphyrins were found to be inferior optical limiters to TPP, SWNTs alone were found to be superior optical limiters to all porphyrins studied except TPP and DETPP, and inferior to all composite solutions.

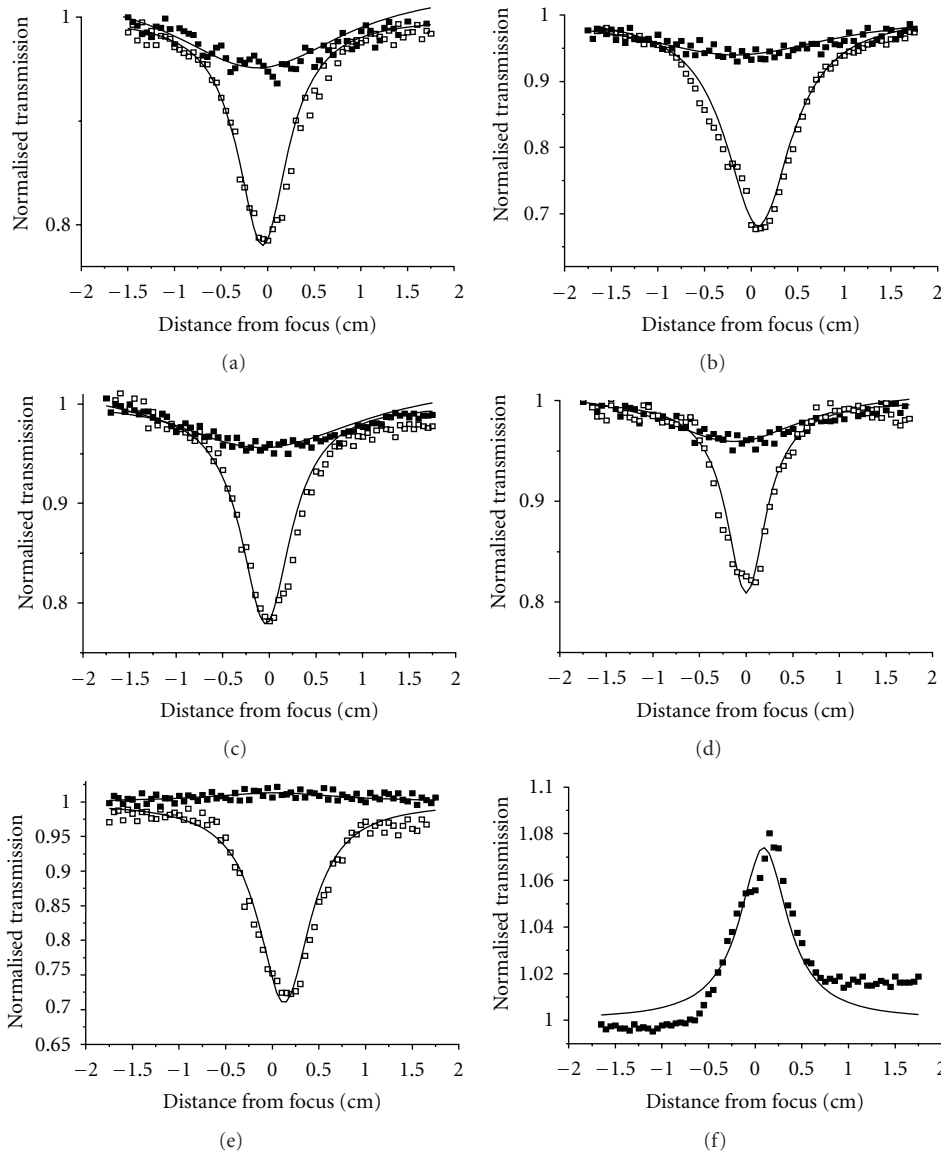


FIGURE 5: Plots of normalised transmission versus distance from focus for porphyrin and composite solutions at low energies for (a) DETPP, (b) tTETPP, (c) cTETPP, (d) HETPP, and (e) OETPP. (f) The higher final transmittance compared with the initial transmittance indicates the destruction of molecules present in the solution. Porphyrin and composite solutions were at concentrations of 0.01 mg/mL, with onfocus intensities of (a) 0.12, (b) 0.13, (c) 0.14, (d) 0.25, (e) 0.23, and (f) 1.63575 GW/cm² for porphyrin solutions and (a) 0.25, (b) 0.16, (c) 0.24, (d) 0.23, and (e) 0.19 GW/cm² for composite solutions.

In the case of three of the nonplanar molecules—tTETPP, HETPP, and OETPP—the optical limiting characteristics of the composites were found to be superior to the combination of the composite components. This was determined by comparing the product of the % transmittance of the constituent porphyrin and SWNT with the % transmittance of the composite at the same concentration for a range of energies. If the superior OL behavior of a composite was simply due to an addition of its two optical limiting components, then the transmission shown by the composite should be equal to the product of the transmittance spectra of its porphyrin and nanotube parts. This was found to be the case for DETPP and cTETPP, indicating negligible interaction between these porphyrins and the carbon nanotubes in solution.

The optical limiting curves are shown in Figure 6. Normalized transmission (T_{norm}) was plotted as a function of incident pulse energy density (J cm^{-2}). The nonlinear absorption coefficient $\alpha(F, F_{\text{sat}}, \kappa)$ was used to fit the normalized transmission as a function of this energy density to the data sets of all open aperture Z scans performed for each compound over a concentration range. Here, $\alpha(F, F_{\text{sat}}, \kappa)$ is derived from laser rate equations for the steady state and is defined as $\alpha(F, F_{\text{sat}}, \kappa) \approx \alpha_0(1 + F/F_{\text{sat}})^{-1}(1 + \kappa F/F_{\text{sat}})$, where F represents the energy density, F_{sat} the saturation energy density, and κ the ratio of the excited to ground state absorption cross-sections, as previously described [10]. The optical limiting (OL) curves (plots of normalized transmission against pulse energy density) for all solutions

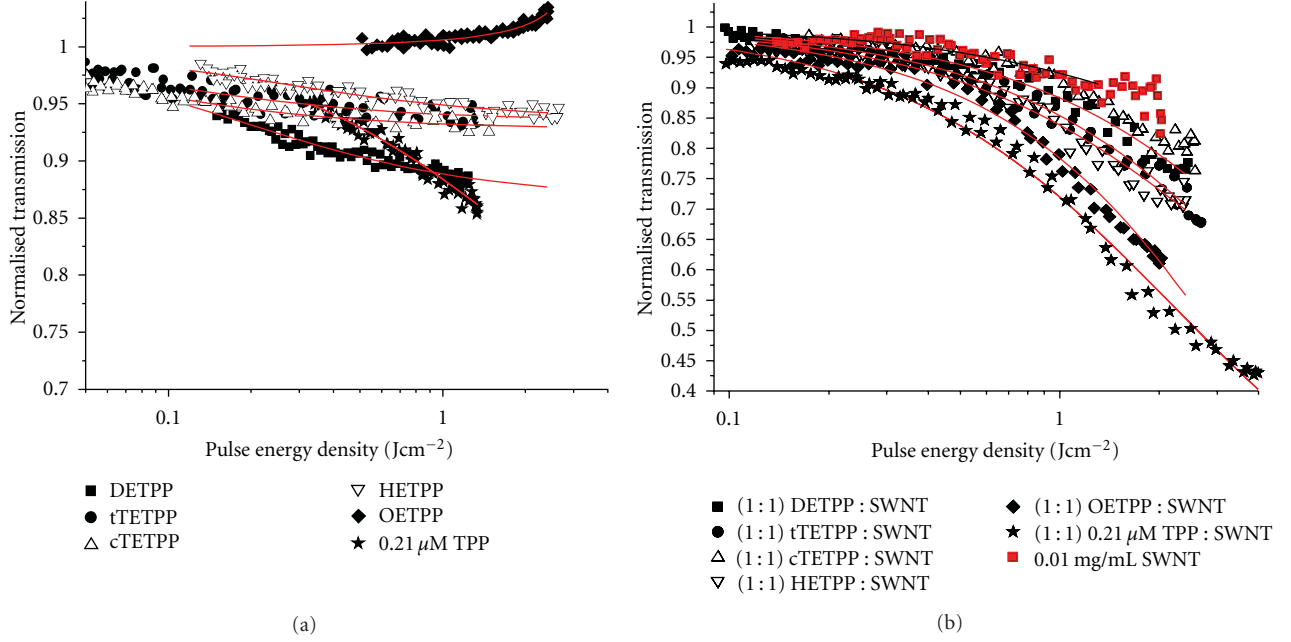


FIGURE 6: Superior optical limiting behaviour of porphyrin composites is clearly to be seen in these plots of normalised transmission versus pulse energy density. All plots are for onfocus beam intensity I_0 of 0.2 GW/cm^2 (approximately).

TABLE 1: Optical coefficients for the materials measured.

Sample	c μM	Solvent	α_0 cm^{-1}	β_I Cm W^{-1}	$\text{Im}\{\chi_{\text{eff}}^{(3)}\}$ Esu	I_0 GW cm^{-2}	F_{sat} J cm^{-2}	κ $\sigma_{\text{ex}}/\sigma_0$
TPP	21.5	DMF	0.11	2.84×10^{-9}	9.74×10^{-13}	0.13	2.14 ± 0.22	4.38 ± 0.24
TPP + SWNT	21.5	DMF	0.42	6.22×10^{-9}	2.14×10^{-12}	0.19	4.14 ± 0.31	3.62 ± 0.15
DETPP	$0.01 \text{ g/L} = c. 16 \mu\text{M}$	DMF	0.25	2.63×10^{-9}	9.03×10^{-13}	0.12	0.20 ± 0.01	1.57 ± 0.01
DETPP + SWNT	$c. 16 \mu\text{M}$	DMF	0.55	5.49×10^{-9}	1.89×10^{-12}	0.25	$17.86 \pm 7.0 2$	5.30 ± 1.54
tTETPP	$c. 16 \mu\text{M}$	DMF	0.24	1.17×10^{-9}	4.03×10^{-13}	0.13	0.09 ± 0.01	1.28 ± 0.01
tTETPP + SWNT	$c. 16 \mu\text{M}$	DMF	0.57	1.06×10^{-8}	3.65×10^{-12}	0.16	14.30 ± 3.42	5.27 ± 0.90
cTETPP	$c. 16 \mu\text{M}$	DMF	0.42	1.33×10^{-9}	4.57×10^{-13}	0.14	0.07 ± 0.004	1.18 ± 0.003
cTETPP + SWNT	$c. 16 \mu\text{M}$	DMF	0.69	3.35×10^{-9}	1.15×10^{-12}	0.24	18.42 ± 8.60	3.81 ± 1.19
HETPP	$c. 16 \mu\text{M}$	DMF	0.20	5.6×10^{-10}	1.92×10^{-13}	0.25	0.26 ± 0.02	1.33 ± 0.01
HETPP + SWNT	$c. 16 \mu\text{M}$	DMF	0.65	5.84×10^{-9}	2.01×10^{-12}	0.23	6.74 ± 1.20	3.11 ± 0.30
OETPP	$c. 16 \mu\text{M}$	DMF	0.20	-2.82×10^{-10}	-9.68×10^{-14}	0.23	-3.79 ± 0.21	1.08 ± 0.01
OETPP + SWNT	$c. 16 \mu\text{M}$	DMF	0.73	1.18×10^{-8}	4.07×10^{-12}	0.19	n/a*	n/a*
SWNT	0.01 g/L	DMF	0.29	1.87×10^{-9}	6.41×10^{-13}	0.19	5.28 ± 2.18	2.72 ± 0.56

*These data did not conform to the model, probably because the optical nonlinearities were predominantly caused by scattering in this composite system, whereas the fit assumes purely absorption-based optical nonlinearities.

are shown in Figure 6 where the solid lines are theoretical fits to the experimental data. All values of α_0 , κ , and F_{sat} calculated for each compound are presented in Table 1. Reported values calculate an absorption cross-section κ of (30 ± 6) and β_I of approximately $4.5 \times 10^{-8} \text{ cm/W}$ at an irradiation of 0.4 GW/cm^2 for the benchmark molecule chloro (phthalocyaninato) indium [39].

3.2. Computational Results. It was found through molecular simulation of these porphyrin composite systems that some porphyrin molecules DETPP and tTETPP in particular did exhibit a pronounced tendency to aggregate onto the SWNT

surface, or at closest remove within 4-5 angstroms of the SWNT with no DMF solvation layer present. However, other porphyrins—TPP and cTETPP—in particular exhibited no tendency to aggregate onto the SWNT in these studies. All porphyrin molecules studied exhibited a tendency to self-aggregate. These observations are summarized in Table 2 below, where N denotes the number of porphyrin molecules in contact with the SWNT, and M denotes the largest porphyrin derivative self-aggregate. The observations were made over .2 ns interval subsequent to the 1 ns equilibration period, by which time the values of N and M did not fluctuate appreciably.

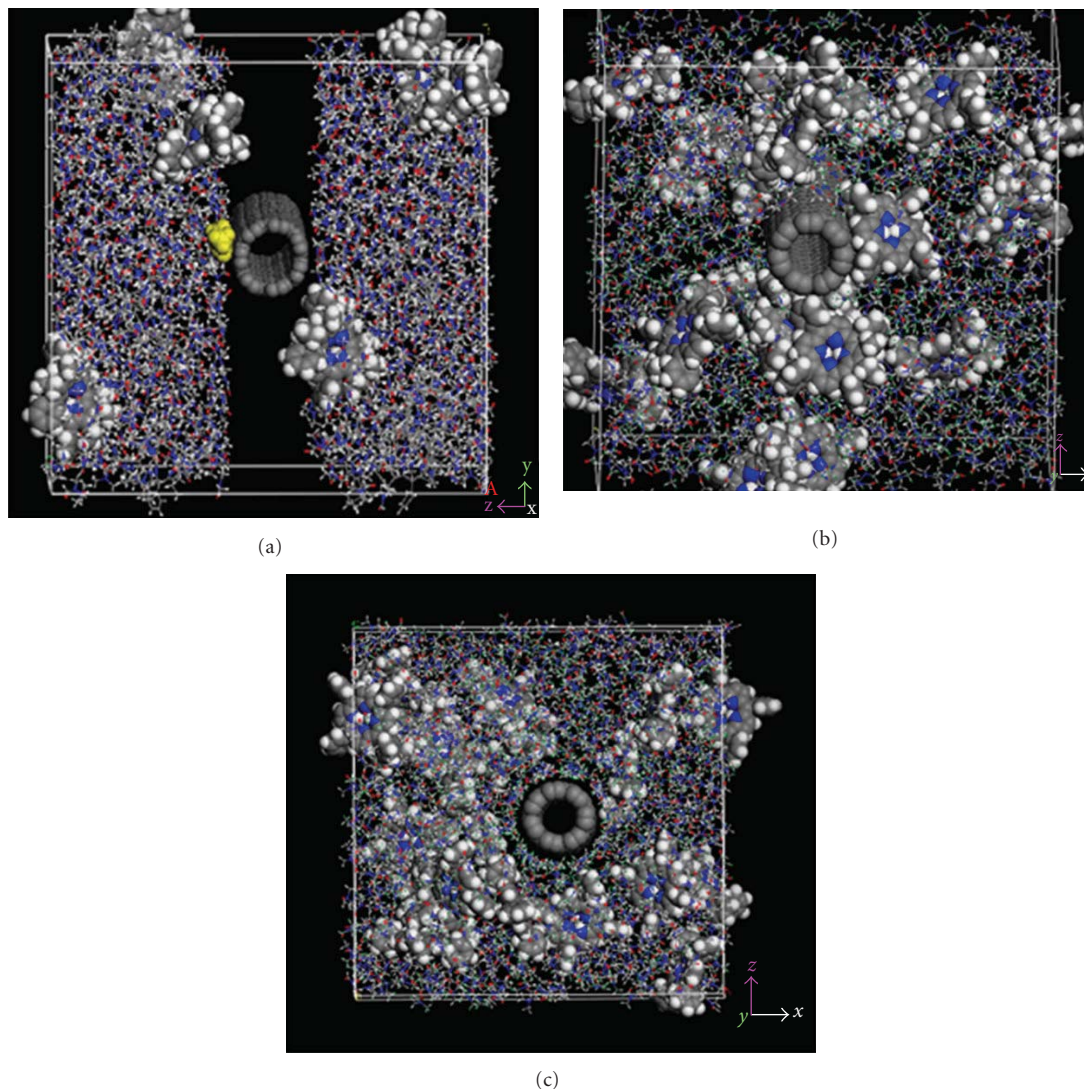


FIGURE 7: (a) Simulation initial conditions are shown for the HETPP-SWNT-DMF system. While there are 20 HETPP molecules, only 4 HETPP molecules, a single DMF (yellow) molecule, and the SWNT are actually rendered using effective Van der Waals diameters. The box is in fact repeated in all directions periodically, to simulate a bulk solvent, and an infinitely long SWNT. (b) The DETPP-SWNT-DMF solvent system. The pronounced tendencies of DETPP to aggregate on, and close to the SWNT, are evident. (c) The TPP-CNT-DMF solvent system. There is no tendency for TPP to aggregate on or close to the CNT.

TABLE 2: Summary of porphyrin aggregation behaviour.

Sample	N	M
TPP	0	3
DETPP	4	5
tTETPP	4	3
cTETPP	0	3
HETPP	3	3
OETPP	3	5

N denotes the number of porphyrin molecules in contact with the SWNT, and M denotes the largest porphyrin derivative self-aggregate.

The two extreme cases, DETPP and TPP, are presented in Figure 7 below, along with the starting conditions for the simulations. The simulations revealed the tendency of

certain porphyrin molecules to have enhanced aggregation abilities onto the CNT, roughly in line with experiment. All porphyrin derivatives additionally exhibited a tendency to self-aggregate. This tendency was confirmed by running simulations for the porphyrin molecules alone both in pure DMF solvent and in vacuum in the absence of SWNT.

4. Conclusion

In conclusion, linear and nonlinear optical techniques have been of value in clarifying the existence and extent of noncovalent interaction between a series of aromatic tetraphenylporphyrin derivatives and carbon nanotubes in solution. This series of TPP derivatives provided a means of systematically investigating the importance of porphyrin

macrocycle conformation on the strength of this noncovalent interaction between these two moieties. Convincing evidence of binding between SWNT and three of these porphyrins was discovered using a number of experimental techniques. Absorption spectroscopy indicated binding of HETPP and OETPP, the two most non-planar porphyrins studied, onto the surface of the SWNT in solution. The evidence for their binding came from shifts in the porphyrin Q bands and some of the carbon nanotube Van Hove peaks in the absorption spectra measured for these systems. The tTETPP molecule did not show these shifts in the absorption spectra but was found to exhibit photoluminescence quenching for the composite solutions. The PL quenching followed by this system was found to be highly nonlinear when plotted as a function of nanotube concentration, and in excellent agreement with a theoretical model which has been found to accurately describe the noncovalent binding of conjugated organic moieties onto the surfaces of SWNT in solution. The tTETPP molecule was the only porphyrin found to obey this binding model. DETPP also displayed weak (~15%) PL quenching for dilute 1:1 composite solutions. It was not possible to assess the interaction of the most nonplanar molecule OETPP with SWNT using these concentration-dependent PL studies, as this molecule did not emit any measurable fluorescence. Nonlinear optical studies using the Z-scan technique showed that the nonlinear absorption coefficient, and, therefore, the optical limiting behavior, of the TPP derivatives studied deteriorated with increasing porphyrin nonplanarity. It was found that the formation of nanotube composites dramatically improved the optical limiting properties of all molecules studied. Evidence of interaction between the SWNT and the porphyrin molecules was found for tTETPP, HETPP, and OETPP from their optical limiting performance, consistent with the results found from the linear optical studies. No evidence of interaction was found experimentally for the molecules TPP and cTETPP. In general, while it was found that the more nonplanar porphyrin molecules have a higher likelihood of noncovalent binding onto nanotubes, it is clear that this is not the only factor determining the noncovalent interaction between them. It was also found that the significant photoluminescence quenching behavior reported in literature for porphyrin composite solutions, and subsequently attributed to electron or energy transfer from the porphyrin molecule to the nanotube, is at least partly caused by photoluminescence and excitation self absorption. Complementary molecular dynamics studies were in striking agreement with these experimental observations. It should be noted that DMF is a very polar solvent, and other solvents may exhibit different properties. Therefore, it may also be of interest to examine other solvents and their effects on these systems.

Acknowledgments

This work was supported by research Grants from Science Foundation Ireland SFI P.I. 09/IN.1/B2650 (for M. O. Senge), SFI/05RFP/CHE0100 (for W.J.Blau), and by SFI 08-IN.1-I1869 (for D.Mackernan).

References

- [1] M. O. Senge, "The conformational flexibility of tetrapyrroles—current model studies and photobiological relevance," *Journal of Photochemistry and Photobiology. B*, vol. 16, no. 1, pp. 3–36, 1992.
- [2] M. O. Senge, "Exercises in molecular gymnastics—bending, stretching and twisting porphyrins," *Chemical Communications*, no. 3, pp. 243–256, 2006.
- [3] M. Ravikanth and T. K. Chandrashekar, "Nonplanar porphyrins and their biological relevance: ground and excited state dynamics," *Structure and Bonding*, vol. 82, pp. 105–188, 1995.
- [4] S. Iijima, "Helical microtubules of graphitic carbon," *Nature*, vol. 354, no. 6348, pp. 56–58, 1991.
- [5] H. Murakami, T. Nomura, and N. Nakashima, "Noncovalent porphyrin-functionalized single-walled carbon nanotubes in solution and the formation of porphyrin-nanotube nanocomposites," *Chemical Physics Letters*, vol. 378, no. 5-6, pp. 481–485, 2003.
- [6] H. Li, B. Zhou, Y. Lin et al., "Selective Interactions of porphyrins with semiconducting single-walled carbon nanotubes," *Journal of the American Chemical Society*, vol. 126, no. 4, pp. 1014–1015, 2004.
- [7] D. M. Guldi, H. Taieb, G. M. A. Rahman, N. Tagmatarchis, and M. Prato, "Novel photoactive single-walled carbon nanotube-porphyrin polymer wraps: efficient and long-lived intracomplex charge separation," *Advanced Materials*, vol. 17, no. 7, pp. 871–875, 2005.
- [8] J. Chen and C. P. Collier, "Noncovalent functionalization of single-walled carbon nanotubes with water-soluble porphyrins," *Journal of Physical Chemistry. B*, vol. 109, no. 16, pp. 7605–7609, 2005.
- [9] H. Li, R. B. Martin, B. A. Harruff, R. A. Carino, L. F. Allard, and Y. P. Sun, "Single-walled carbon nanotubes tethered with porphyrins: synthesis and photophysical properties," *Advanced Materials*, vol. 16, no. 11, pp. 896–900, 2004.
- [10] E. N. Mhuircheartaigh, S. Giordani, and W. J. Blau, "Linear and nonlinear optical characterization of a tetraphenylporphyrin—carbon nanotube composite system," *Journal of Physical Chemistry. B*, vol. 110, no. 46, pp. 23136–23141, 2006.
- [11] J. Wang and W. J. Blau, "Inorganic and hybrid nanostructures for optical limiting," *Journal of Optics. A*, vol. 11, no. 2, Article ID 024001, 2009.
- [12] G. X. Chen, M. H. Hong, L. S. Tan et al., "Optical limiting phenomena of carbon nanoparticles prepared by laser ablation in liquids," *Journal of Physics: Conference Series*, vol. 59, no. 1, pp. 289–292, 2007.
- [13] W. W. Kalisch and M. O. Senge, "Synthesis and structural characterization of nonplanar tetraphenylporphyrins with graded degree of β -ethyl substitution," *Tetrahedron Letters*, vol. 37, no. 8, pp. 1183–1186, 1996.
- [14] M. O. Senge and W. W. Kalisch, "Synthesis and structural characterization of nonplanar tetraphenylporphyrins and their metal complexes with graded degrees of β -ethyl substitution," *Inorganic Chemistry*, vol. 36, no. 26, pp. 6103–6116, 1997.
- [15] L. D. Sparks, C. J. Medforth, M. S. Park et al., "Metal dependence of the nonplanar distortion of octaalkyltetraphenylporphyrins," *Journal of the American Chemical Society*, vol. 115, no. 2, pp. 581–592, 1993.
- [16] J. E. Seto, S. I. Tamura, N. Asai, N. Kishii, Y. Kijima, and N. Matsuzawa, "Macrocyclic functional dyes: applications to optical disk media, photochemical hole burning and nonlinear

- optics," *Pure and Applied Chemistry*, vol. 68, no. 7, pp. 1429–1434, 1996.
- [17] M. Calvete, G. Y. Yang, and M. Hanack, "Porphyrins and phthalocyanines as materials for optical limiting," *Synthetic Metals*, vol. 141, no. 3, pp. 231–243, 2004.
- [18] L. Vivien, E. Anglaret, D. Riehl et al., "Optical limiting properties of singlewall carbon nanotubes," *Optics Communications*, vol. 174, no. 1–4, pp. 271–275, 2000.
- [19] S. R. Mishra, H. S. Rawat, S. C. Mehendale et al., "Optical limiting in single-walled carbon nanotube suspensions," *Chemical Physics Letters*, vol. 317, no. 3–5, pp. 510–514, 2000.
- [20] J. E. Riggs, D. B. Walker, D. L. Carroll, and Y. P. Sun, "Optical limiting properties of suspended and solubilized carbon nanotubes," *Journal of Physical Chemistry. B*, vol. 104, no. 30, pp. 7071–7076, 2000.
- [21] P. Nikolaev, M. J. Bronikowski, R. K. Bradley et al., "Gas-phase catalytic growth of single-walled carbon nanotubes from carbon monoxide," *Chemical Physics Letters*, vol. 313, no. 1–2, pp. 91–97, 1999.
- [22] M. Sheik-Bahae, A. A. Said, T. H. Wei, D. J. Hagan, and E. W. van Stryland, "Sensitive measurement of optical nonlinearities using a single beam," *IEEE Journal of Quantum Electronics*, vol. 26, no. 4, pp. 760–769, 1990.
- [23] S. M. O'Flaherty, S. V. Hold, M. J. Cook et al., "Molecular engineering of peripherally and axially modified phthalocyanines for optical limiting and nonlinear optics," *Advanced Materials*, vol. 15, no. 1, pp. 19–32, 2003.
- [24] H. Sun, "Compass: an ab initio force-field optimized for condensed-phase applications—overview with details on alkane and benzene compounds," *Journal of Physical Chemistry. B*, vol. 102, no. 38, pp. 7338–7364, 1998.
- [25] E. N. Mhuircheartaigh, W. J. Blau, M. Prato, and S. Giordani, "Sonication of porphyrin-nanotube composites: a cautionary tale," *Physica Status Solidi. B*, vol. 244, no. 11, pp. 4227–4230, 2007.
- [26] M. O. Senge, C. J. Medforth, L. D. Sparks, J. A. Shelnutt, and K. M. Smith, "A planar dodecasubstituted porphyrin," *Inorganic Chemistry*, vol. 32, no. 9, pp. 1716–1723, 1993.
- [27] M. O. Senge, M. W. Renner, W. W. Kalisch, and J. Fajer, "Molecular structure of (5,10,15,20-tetrabutyl-2,3,7,8,12,13,17,18-octaethylporphyrinato)nickel(II)- correlation of non-planarity with frontier orbital shifts," *Journal of the Chemical Society, Dalton Transactions*, no. 3, pp. 381–385, 2000.
- [28] N. C. Maiti and M. Ravikanth, "Effects of non-planarity and β -substitution on the singlet-excited-state properties of basket-handle porphyrins," *Journal of the Chemical Society, Faraday Transactions*, vol. 92, no. 7, pp. 1095–1100, 1996.
- [29] A. Rosa, G. Ricciardi, E. J. Baerends, A. Romeo, and L. M. Scolaro, "Effects of porphyrin core saddling, meso-phenyl twisting, and counterions on the optical properties of meso-tetraphenylporphyrin diacids: the $[H_4TPP](X)_2$ ($X = F, Cl, Br, I$) series as a case study," *Journal of Physical Chemistry. A*, vol. 107, no. 51, pp. 11468–11482, 2003.
- [30] D. Baskaran, J. W. Mays, X. P. Zhang, and M. S. Bratcher, "Carbon nanotubes with covalently linked porphyrin antennae: photoinduced electron transfer," *Journal of the American Chemical Society*, vol. 127, no. 19, pp. 6916–6917, 2005.
- [31] A. Satake, Y. Miyajima, and Y. Kobuke, "Porphyrin-carbon nanotube composites formed by noncovalent polymer wrapping," *Chemistry of Materials*, vol. 17, no. 4, pp. 716–724, 2005.
- [32] D. M. Guldi, H. Taieb, G. M. A. Rahman, N. Tagmatarchis, and M. Prato, "Novel photoactive single-walled carbon nanotube-porphyrin polymer wraps: efficient and long-lived intracomplex charge separation," *Advanced Materials*, vol. 17, no. 7, pp. 871–875, 2005.
- [33] G. M. A. Rahman, D. M. Guldi, S. Campidelli, and M. Prato, "Electronically interacting single wall carbon nanotube-porphyrin nano hybrids," *Journal of Materials Chemistry*, vol. 16, no. 1, pp. 62–65, 2006.
- [34] J. N. Miller, *Standards in Fluorescence Spectrometry*, Chapter 5, Chapman & Hall, New York, NY, USA, 1981.
- [35] C. A. Parker and W. T. Rees, "Fluorescence spectrometry. A review," *The Analyst*, vol. 87, no. 1031, pp. 83–111, 1962.
- [36] J. N. Coleman, A. Fleming, S. Maier et al., "Binding kinetics and SWNT bundle dissociation in low concentration polymer-nanotube dispersions," *Journal of Physical Chemistry. B*, vol. 108, no. 11, pp. 3446–3450, 2004.
- [37] M. Sheik-Bahae, A. A. Said, D. J. Hagan, M. J. Soileau, and E. W. van Stryland, "Nonlinear refraction and optical limiting in thick media," *Optical Engineering*, vol. 30, pp. 1228–1235, 1991.
- [38] E. Fazio, F. Neri, S. Patanè, L. D'Urso, and G. Compagnini, "Optical limiting effects in linear carbon chains," *Carbon*, vol. 49, no. 1, pp. 306–310, 2011.
- [39] J. W. Perry, K. Mansour, I. Y. S. Lee et al., "Organic optical limiter with a strong nonlinear absorptive response," *Science*, vol. 273, no. 5281, pp. 1533–1536, 1996.